DEM Generation and Ocean Tide Modeling Over Sulzberger Ice Shelf, West Antarctica, Using Synthetic Aperture Radar Interferometry

by

Sang-Ho Baek

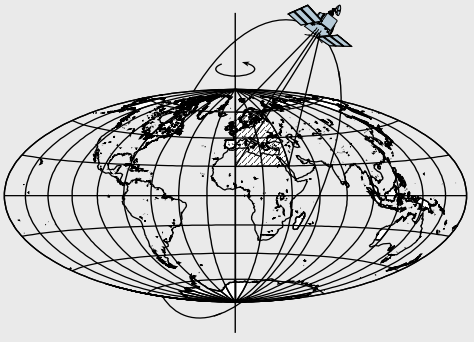

Report No. 480

Geodetic Science and Surveying
School of Earth Sciences
The Ohio State University
Columbus, Ohio 43210

August 2006

DEM GENERATION AND OCEAN TIDE MODELING OVER SULZBERGER ICE SHELF, WEST ANTARCTICA, USING SYNTHETIC APERTURE RADAR INTERFEROMETRY

by

Sang-Ho Baek

Geodetic Science and Surveying
School of Earth Sciences

The Ohio State University

August 2006

ABSTRACT

The use of Synthetic Aperture Radar Interferometry (InSAR) is an effective tool for studying the ice mass balance of polar regions and its contribution to global sea level change. An accurate, high-resolution digital elevation model (DEM) referenced within a well-defined terrestrial reference frame (TRF) is an inherent requirement to facilitate the use of InSAR to conduct these studies in remote polar regions where ground control points (GCPs) are unavailable. In this study, a digital elevation model by the Sulzberger Bay, West Antarctica is determined by using twelve European Remote Sensing (ERS) -1 and ERS-2 tandem satellite mission synthetic aperture radar scenes and nineteen Ice, Cloud, and land Elevation Satellite (ICESat) laser altimetry profiles. Differential interferograms from the ERS-1/ERS-2 tandem mission SAR scenes acquired in the austral fall of 1996 are used together with four selected ICESat laser altimetry profiles in the austral fall of 2004 which provides GCPs, resulting in an improved geocentric 60-m resolution DEM over the grounded ice region. The InSAR DEM is then extended to include two ice tongues using ICESat profiles via Kriging. Fourteen additional ICESat profiles acquired in 2003-2004 are used to assess the accuracy of the DEM. After accounting for radar penetration depth and predicted surface changes, including effects due to ice mass balance, solid Earth tides, and glacial isostatic adjustment, in part to account for the eight-year data acquisition discrepancy, the resulting difference between the DEM and ICESat profiles is -0.55 ± 5.46 m. After removing the discrepancy between the DEM and ICESat profiles for a final combined DEM using a bicubic spline, the overall difference is 0.05 ± 1.35 m indicating excellent consistency.

Accurate knowledge of the Antarctic ice sheet mass balance plays an important role on the global sea level change. Ocean tides (barotropic and baroclinic) and tidal currents cause basal melting and migration of grounding lines, which are all critical to the accurate determination of ice sheet or ice stream mass balance. Ocean tides in the Antarctic Ocean, especially underneath ice shelves or sea ice, are poorly known primarily due to lack of observations with adequate resolution and knowledge of the bathymetry and ice shelf bottom roughness. InSAR has been used to measure the ice sheet mass

balance, ice topography, ice stream velocity, and the location of the grounding lines. To properly use InSAR measurements for ice mass balance and because of their high spatial resolution (tens of meters), knowledge of ocean tides underneath the ice shelves needs to be accurately known and with commensurate resolution. Here two-pass differential InSAR (DInSAR) technique is applied for tidal signal modeling underneath the Sulzberger ice shelf, West Antarctica. The fine resolution (60-m) Digital Elevation Model (DEM) over grounded ice and ice shelf, obtained by combining ERS-1/2 tandem InSAR and ICESat laser altimetry, has been used to correct the topography phase from interferograms, resulting in a more accurate time series of vertical deformation measurements. In this study, it is demonstrated for the first time, that observable tidal constituents can be estimated underneath an ice shelf using an InSAR time series. In particular, it is shown that the time series of observed tidal differences from InSAR agrees well with a number of global/regional ocean tide models such as NAO.99b, TPXO.6.2, GOT00.2, CATS02.01, and FES2004, with the regional model, CATS02.01, having the best agreement. The technique developed here can be applied to other ice shelf regions where tide modeling is poor in accuracy and resolution.

ACKNOWLEDGMENTS

First of all, I want to express my deepest gratitude to Dr. C. K. Shum for his encouragement and support during my Ph. D. study. His broad knowledge and priceless direction for this study enabled me to reach the goal of the research work. He showed a good example of accepting people with open mind and his positive thinking made me to focus on my study. I would like to express my thanks to Dr. Burkhard Schaffrin for his careful review and advice for this dissertation. The same gratitude should go to Dr. Doug Alsdorf for his comments on my dissertation. His lectures helped me to understand and concrete my knowledge on InSAR principles, processing and applications. My sincere thanks also go to Dr. Zhong Lu for the fruitful discussions and practical help on InSAR processing. I appreciate the valuable discussions and help on basic InSAR processing from Oh-Ig Kwoun at EROS data center and Michael Baessler at TU Dresden, Germany. I thank my colleagues in Laboratory for Space Geodesy and Remote Sensing for their friendship and support during my study.

This research is supported by a grant from the National Science Foundation's Office of Polar Program (OPP-0088029).

TABLE OF CONTENTS

CHAPTER 1

INTRODUCTION

Synthetic Aperture Radar (SAR) is a microwave imaging system which is operational regardless of illumination and weather condition. It is especially advantageous in the polar regions because of their long period of darkness and unfavorable weather condition, which hinders the use of optical sensors. Synthetic Aperture Radar Interferometry (InSAR) and Differential InSAR (DInSAR), as advanced SAR techniques, have been demonstrated to be useful in detecting surface deformations of ice sheets and ice shelves over Antarctica for ice mass balance studies and their contribution to global sea level change [Rignot and Thomas, 2002; Thomas et al., 2004].

1.1 History of Radar Imaging and InSAR

Radar, an acronym for RAdio Detection And Ranging, transmits microwave signals towards an object and measures the strength and the time delay (distance) of the return signals. Radar provides its own energy source which allows independent operation without solar illumination. This type of system is referred to as an active remote sensing system distinguishing it from optical sensors depending on external radiation sources.

Usually a radar system uses wavelengths greater than 1 cm. As shown in Figure 1.1, those wavelengths can penetrate the atmosphere and operate in virtually all weather condition. Most of the development of radar had been for military purposes such as tracking and detecting, fire control, missile guidance, and reconnaissance [Ulaby et al., 1981]. The first operational usage of the imaging radar was built with mechanically-rotating antennas [Henderson and Lewis, 1998] and dates back to World War II, which produced an image in a rectangular format with distance in the across-track, perpendicular to the flight direction, and angle relative to the direction of aircraft orientation. It was prepared to help pilots and bombardiers understand the ground, but it had great distortions because of the nonlinear relations between distance and angle [Ulaby et al., 1981]. In the 1950s, the side-looking airborne radar (SLAR) was developed for military reconnaissance purposes, and finer resolution could be achieved using a relatively long antenna installed parallel to the aircraft body. The along-track resolution of SLAR was a function of the ratio of the wavelength to antenna size and was limited due to an antenna size practically attachable to the aircraft. In 1952, Carl Wiley developed a new radar called the “Doppler beam-sharpening” system and showed that a side-looking radar can improve the along-track resolution by utilizing the Doppler shift of the echoes [Curlander and McDonough, 1991]. Now this technique is referred to as the

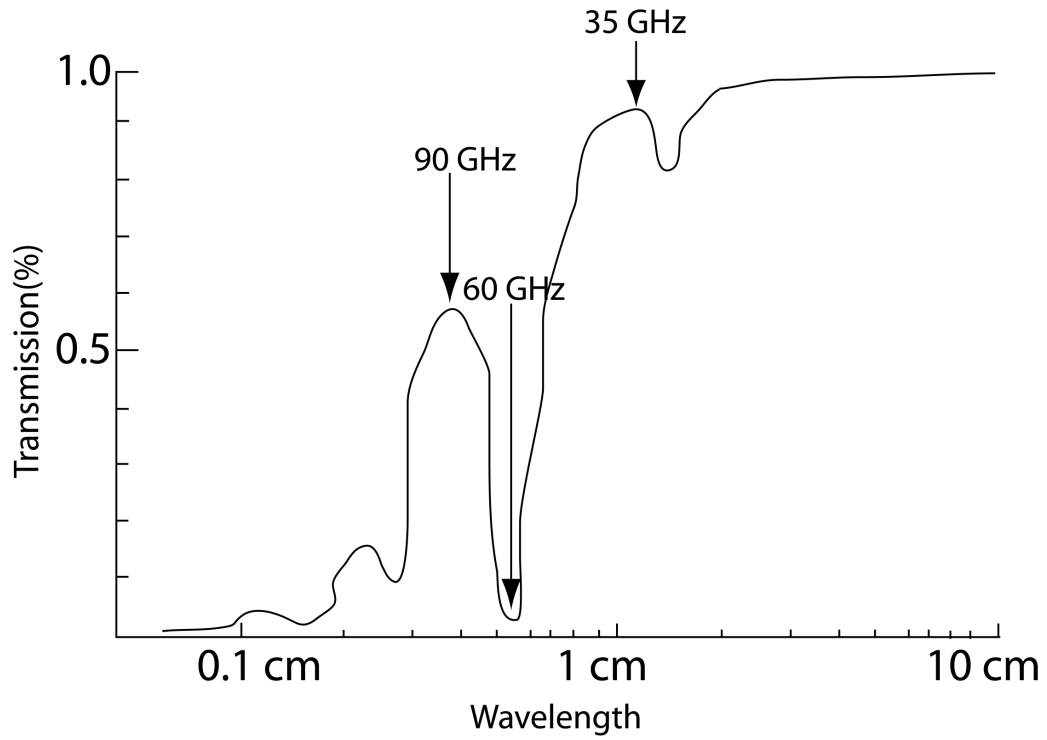

Figure 1.1. Microwave atmosphere transmission [Elachi, 1987].

synthetic aperture radar (SAR) distinguishing it from real aperture radar (RAR). The SAR system allowed finer along-track resolution than SLAR through synthetically created long antennas using a small moving antenna. In addition, its along-track resolution was independent of the distance between radar and an object on the earth surface which was a great advantage to spaceborne systems.

The first spaceborne earth observing radar was on Seasat, launched in June 1978 [Jordan, 1980]. Although it failed after only 105 days, the data were studied over ten years later and demonstrated a unique role of spaceborne microwave remote sensing systems in topography mapping [Goldstein et al., 1988; Li and Goldstein, 1990]. After the successful flight of Seasat, the U.S.A. (National Aeronautics and Space Administration, NASA), the European Union (European Space Agency, ESA), Canada (Canadian Space Agency, CSA), and Japan (Japan Aerospace Exploration Agency, JAXA) have launched spaceborne SAR systems during the last decade (see Table 1.1). ESA's ERS satellites have brought an enormous number of images to researchers in various areas and boosted the use of SAR images to compensate for the disadvantages of optic images [Bamler and Hartl, 1998]. NASA had continued its program of short-term SAR missions onboard the space shuttles such as SIR-A, -B, -C, and Shuttle Radar Topography Mission (SRTM) since the 1980s. The SRTM mission, operated for 11 days in a single-pass mode using two physically separated antennas, measured topography between 60° N and 56° S with improved accuracy over repeat-pass methods.

Now ERS-2 (EU), Radarsat (Canada), Envisat (EU), and ALOS (Japan) are operational, and Radarsat-2 (Canada), TerraSAR-X (Germany), and KOMSAT-5 (South Korea) will be launched shortly. A description of spaceborne SAR missions is given in Table 1.1.

Mission	Year	Nation	Repeat Period, days	Altitude, Km	Carrier frequency, GHz	Range Bandwidth, MHz	Incidence angle, deg	Swath, km
Seasat	1978	U.S.A	3	800	1.275	19.00	20-26	100
SIR-A	1981	U.S.A	-	235	1.278	19.00	50	50
SIR-B	1984	U.S.A	-	235	1.282	12.00	15-64	10-60
ERS-1	1991	EU	35	790	5.300	15.55	21-26	100
JERES-1	1992	Japan	44	568	1.275	15.00	26-41	85
SIR-C/ X-SAR	1994	U.S.A, Germany, Italy	1	225	1.240	20.00	15-55	85
ERS-2	1995	EU	35	790	5.300	15.55	21-26	100
Radarsat	1995	Canada	24	792	5.300	11-30	20-49	10-500
SRTM	2000	U.S.A	-	233	5.300 9.600	9.50	52	225 50
ENVISAT	2001	EU	35	800	5.331	14.00	20-50	100-500
ALOS	2006	Japan	45	700	1.270	28/14	8-60	40-350
Radarsat -2	(2006)	Canada	24	798	5.405	12-100	20-60	20-500
TerraSAR-X	(2006)	Germany	11	514	9.650	150	20-45	30
KOMSAT-5	(2009)	R.O.K						

Table 1.1. Spaceborne SAR systems.

The first non-military radar (RAR) mapping project was conducted over a secluded area covered by clouds and tropical forests in Panama, in 1967 [Viksne et al., 1969]. Conventional optical aerial photogrammetry was hindered over this area due to the persistent cloud-covering weather condition and logistical problems. After the success of this mapping project, Venezuela (1971) and Brazil (1971) applied radar mapping systems for border definitions, water and natural resources mapping, and geologic analysis [van Roessel and de Godoy, 1974]. The first experiment of airborne SAR interferometry for topography mapping was reported by Graham [1974]. He used two vertically deployed antennas to record the relative phase difference of the backscattered signals. Later his idea has been applied digitally by Zebker and Goldstein [1986]. They developed InSAR systems which can record the complex amplitude and phase information digitally for each antenna, and presented InSAR processing over the San Francisco area with the L-band NASA CV990 aircraft system, thereby generating a 11 km by 10 km topographic map. Goldstein et al. [1988] and Li and Goldstein [1990] reported the first topographic mapping results from an earth orbiting spaceborne radar system with Seasat. After launching the ERS-1 satellite, Zebker et al. [1994a] employed the ERS-1 radar system for topographic applications. They used 3-day repeat-pass ERS-1 data and presented topographic maps with rms errors of ±5 m. With the successful launching of the ERS-2 in 1995, Rufino et al. [1998] generated InSAR DEM over an area of 10 km by 10 km using the ERS-1/2 tandem mission. They demonstrated that over the test area (southern Italy) only the tandem pair is available to make an interferogram due to the short temporal baseline (1 day).

In the glaciological studies, densely sampled DEM is useful for studying ice sheet dynamics and their mass balance [Joughin, 1995]. After the successful launch of spaceborne radar altimetries, such as those on Seasat, Geosat, and ERS-1, absolute elevations had been measured [Zwally et al., 1983, 1987, 1989, 1997; Ridley et al., 1989; Bamber and Bindschadler, 1997]. However, topography from radar altimetry could not meet the resolution and accuracy requirements of ice mass balance studies [Rosen et al., 2000]. Joughin et al. [1996] and Kwok and Fahnestock [1996] presented on InSAR DEM from 3-day repeat ERS-1 data over Greenland. Eldhuset et al. [2003] presented the use of ERS-1/2 tandem mission data, for the first time, for glacier mapping applications. In spite of the use of various sensors for mapping over polar regions, the majority of the Greenland and Antarctic ice sheet topography is still poorly unknown [Rosen et al., 2000].

Smith [1991] used tiltmeters to detect tidal signals near the grounding zone of the Ronne Ice Shelf, Antarctica, and Vaughan [1994, 1995], Reeh et al. [2000], and King et al. [2000, 2005] detected tidal flexure using Global Positioning System (GPS) data over ice streams in Antarctica. Shepherd and Peacock [2003] suggested a solution of ice shelf surface tidal motion for major diurnal and semidiurnal constituents from ERS radar altimeter range measurements. Han et al. [2005] used spaceborne gravimeter measurements from GRACE to estimate two tidal constituents, M_2 and S_2, over the Filchner Ronne Ice Shelf and the Larsen Ice Shelf. The first attempt to detect a tidal signal using InSAR was reported by Goldstein et al. [1993] over the Rutford ice

stream, West Antarctica, and the tidal deformation from InSAR was compared to the standard bending-elastic-beam model of tidal flexure. Hartl et al. [1994] compared the tidal difference from differential interferometry between two ERS-1 3-day repeat orbit data (three-pass) with ocean tidal height predictions under the Ronne Ice Shelf, Antarctica. Rignot [1996] and Rignot and MacAyeal [1998] performed tidal signal detection by using four-pass interferometry under Antarctic ice shelves. Rignot et al. [2000] demonstrated that, theoretically, DInSAR measurement could be used to estimate tidal constituents under ice shelves directly. Schmeltz et al. [2002] used DInSAR measurement to validate tide models under floating ice shelves.

1.2 Background and Motivation

The predictability of ocean tides is significantly less accurate in the coastal regions, littoral and shallow seas, and oceans not covered by TOPEX/POSEIDON, than in the deep ocean and within ±66° latitude. Even with the availability of the most recent suite of global tide models, based primarily on TOPEX/POSEIDON data, extreme southern ocean tide models are limited both in accuracy and resolution, especially in seasonally or perpetually sea ice covered oceans near Antarctica.

In this dissertation, multiple repeat-pass InSAR data from the ESA's ERS-1 and ERS-2 satellites are used to detect ocean tidal deformation and to model it underneath the Sulzberger Ice Shelf in West Antarctica. For the purpose of topography correction for the InSAR deformation study, a high resolution and accurate Digital Elevation Model (DEM) over the study area is required. The most complete DEMs currently available in the study area include The Ohio State University Byrd Polar Research Center's (BPRC's) DEM, generated using ERS-1 ice mode radar altimetry and other data [Liu et al., 1999]. The 200-m resolution BPRC Radarsat Mapping Project (RAMP) DEM was generated using ERS-1 altimetry, airborne survey, and the Antarctic Digital Database (ADD) data [Liu et al., 2001]. An attempt to use the RAMP DEM to correct the topographic effect for repeat-pass InSAR studies of ice stream velocities, tidal dynamics, and grounding line migrations over the Sulzberger Ice Shelf region [Shum et al., 2002] was unsuccessful, due primarily to the coarse resolution and poor accuracy in the model, and provided motivation to create an improved DEM for this region. InSAR has proven to be an excellent tool to derive DEMs with high spatial resolution (~40–60 m) [Zebker and Goldstein, 1986, Goldstein et al., 1988; Li and Goldstein, 1990; Zebker et al., 1994a; Joughin et al., 1996; Kwok and Fahnestock, 1996; Rufino et al., 1998; Hensley et al., 2001; Eldhuset et al., 2003]. However, the estimation of ice topography using InSAR has always been a challenge because accurate ground control points (GCPs) with known latitude, longitude, and height to refine baseline estimation and to tie the DEM to the vertical datum are often unavailable. Extreme weather conditions and logistic difficulties in Antarctica are among the barriers to collecting necessary GCPs by ground survey for InSAR studies. Therefore, a multi-sensor approach was sought from previous studies (see [Zebker et al., 1994a, Joughin et al., 1996]), using radar altimetry data to account for missing GCPs. In this dissertation, geocentric ice height data from the Geoscience Laser Altimeter System (GLAS) instrument on NASA's Ice, Cloud, and Land Elevation Satellite (ICESat) [Schutz, 1998] are used to replace

GCPs in InSAR processing.

Floating ice shelves are affected by the ocean tides underbeath them [Holdsworth, 1969, 1977; Fricker, 2002]. As mentioned above, the vertical deformation of the ice shelf in Antarctica due to the ocean tide signal has been studied by tiltmeters [Smith, 1991], satellite altimetry [Shepherd and Peacock, 2003], Global Positioning System (GPS) [Vaughan, 1994, 1995; Reeh et al., 2000; King et al., 2000, 2005], satellite gravimeter [Han et al., 2005], and InSAR [Goldstein et al., 1993; Hartl et al., 1994; Rignot, 1996; Rignot et al., 1998, 2000; Schmeltz et al., 2002]. InSAR offers greater precision than other methods and is currently the only method that provides snapshots of the differential tidal displacement of an ice shelf, simultaneously, at a high spatial resolution such as 20 m to 60 m over extensive areas (~100km). However, several previous studies for ocean tide detection using InSAR were not successful in generating a tide model, but instead demonstrated that InSAR data are sensitive to tidal deformation and thus could validate tide models defined over Antarctica [MacAyeal et al., 1998; Rignot and MacAyeal, 1998; Padman et al., 2003b]. In this dissertation, to overcome the limitation of applying the four-pass method addressed by Rignot et al. [2000] and Padman et al. [2003b], the two-pass InSAR methodology, which is based on the combination of datasets between interferogram and DEM, is applied to first demonstrate the detection of ocean tidal signals under the ice shelf, and then to determine selected tidal constituents towards the determination of a high-resolution ocean tide model from InSAR.

1.3 Summary of Chapters

Chapter 2 reviews the basis of SAR and InSAR theory. The InSAR processing issues and DInSAR methods are discussed along with the limitation of InSAR as a geodetic tool.

Chapter 3 deals with ERS-1/2 InSAR DEM generation procedure using ICESat altimetry profiles to replace GCPs. To aid the understanding for datasets used in this dissertation, introductions to the ERS and ICESat systems are given as well. After accounting for radar penetration depth and predicted surface changes, including effects due to ice mass balance, solid earth tides, and glacial isostatic adjustment, the InSAR DEM accuracy was validated using additional ICESat profiles. Extension of the InSAR DEM over two ice tongues are conducted using ICESat profiles via Kriging.

Chapter 4 is devoted to tidal signal restoration using InSAR. Basic theory for ocean tide and tide models are given along with the InSAR tide signal measurements and estimated tidal constituents. The tidal constituent estimates are compared with several other tide models.

Chapter 5 summarizes the use of InSAR in ice mass balance studies and the conclusions with on outlook on future studies are given in Chapter 6.

CHAPTER 2

OVERVIEW OF SAR AND SAR INTERFEROMETRY THEORY

2.1 Introduction

SAR is an active sensor that illuminates the surface with microwaves and captures the backscattered signal. Because of this characteristic, unlike optical sensors, which are called passive sensors for their dependency on sunlight for data acquisition, SAR can acquire images over night and always unfavorable weather conditions. However, because of the active sensor characteristic, it needs power to generate microwaves, and its life span could be relatively short compared with optical sensors. In this chapter, SAR and InSAR procedures are concisely reviewed to describe the digital elevation model generation and the tidal signal reconstruction, in particular using InSAR, as are discussed in Chapters 3 and 4, respectively. In addition, the ERS satellites and the ICESat sensor characteristics are introduced at the end of this chapter.

2.2 SAR Signal Processing

If the radar is turned on for a very short time, and then off again, a brief burst of radio energy is emitted. As two targets *a* and *b* on the ground (Figure 2.1) return echoes back to the radar receiving unit (or antenna) onboard of the spacecraft or aircraft, two echoes will arrive at different times because of their different distances in the slant range directions. Those echoes arrive at different times as radar signals are recorded as a function of travel time and intensity as a single line in Figure 2.2. The shorter pulse has the better range resolution (it will be explained in the next section). By forming other strip lines, produced in the same manner as the first strip line at subsequent times, two-dimensional images can be formed as can be seen in Figure 2.2. To generate radar images in this way, two problems should be considered and overcome [Cenzo, 1981]. First, to maintain the pulse in range to be short for the better resolution, the transmitted energy of the pulse should be very weak which causes difficulties in detecting the back-scattered echo. Second, two targets within the same radar beam in the along-track direction, e.g., *c* and *d* in Figure 2.3, are not distinguishable. To separate them it is required to design a very narrow along-track beamwidth for the receiving antenna, β_a. However, only extremely large antennas, with a length of several km, could meet this condition. To overcome the first and second limitations, chirp signal and synthetic aperture techniques are introduced, respectively.

2.2.1 Range Resolution

The first problem is solved by simply transmitting a longer pulse but with linear frequency modulated (FM) chirp. As the received chirp signal is compressed to a shorter pulse by cross-correlation, we can obtain required range resolutions of several meters. If

the time extension of the radar pulse is τ (Figure 2.1), the minimum separation of two resolvable points a and b is then [Curlander and McDonough, 1991]

$$R_r = \frac{c\tau}{2} \tag{2.1}$$

where c is the speed of light ($\approx 3\times10^5$ km/s) and the factor of 2 in the denominator accounts for the round trip of the pulse. According to this equation, a better resolution is acquired from a shorter pulse duration time τ. However, as mentioned before, the signal-to-noise ratio (SNR) restricts the use of too short pulse duration, i.e., as we use too short of a pulse duration, its energy is not enough to have a sufficient echo signal. This is a contradiction between a sufficient SNR and high resolution. It will be an ideal situation if we can acquire reasonable resolution using a longer pulse with large enough SNR. A pulse compression or matched filter technique [Cenzo, 1981] over a chirp signal is employed to meet this goal. Through the matched filter technique over a chirp signal, the range resolution is improved as [Curlander and McDonough, 1991]

$$R_r = \frac{c}{2B_W} \tag{2.2}$$

where B_W is the frequency bandwidth of the transmitted pulse. According to the inverse proportional relationship between the range resolution R_r and bandwidth B_W, fine resolution can be acquired by increasing the pulse bandwidth. For the ERS systems, the nominal pulse length is 37.1 μsec and the nominal range bandwidth is 15.55 MHz. With this system configuration the slant resolution without matched filter techniques is about 5.6 km in length (according to equation (2.1)). Through a matched filter, its resolution can be improved to about 10 m and 25 m in the slant range and ground range, respectively. Not only SAR, but also the conventional SLAR uses the same method in acquiring range resolution. It is the way of acquiring along-track resolution that distinguishes SAR from other radar imaging systems.

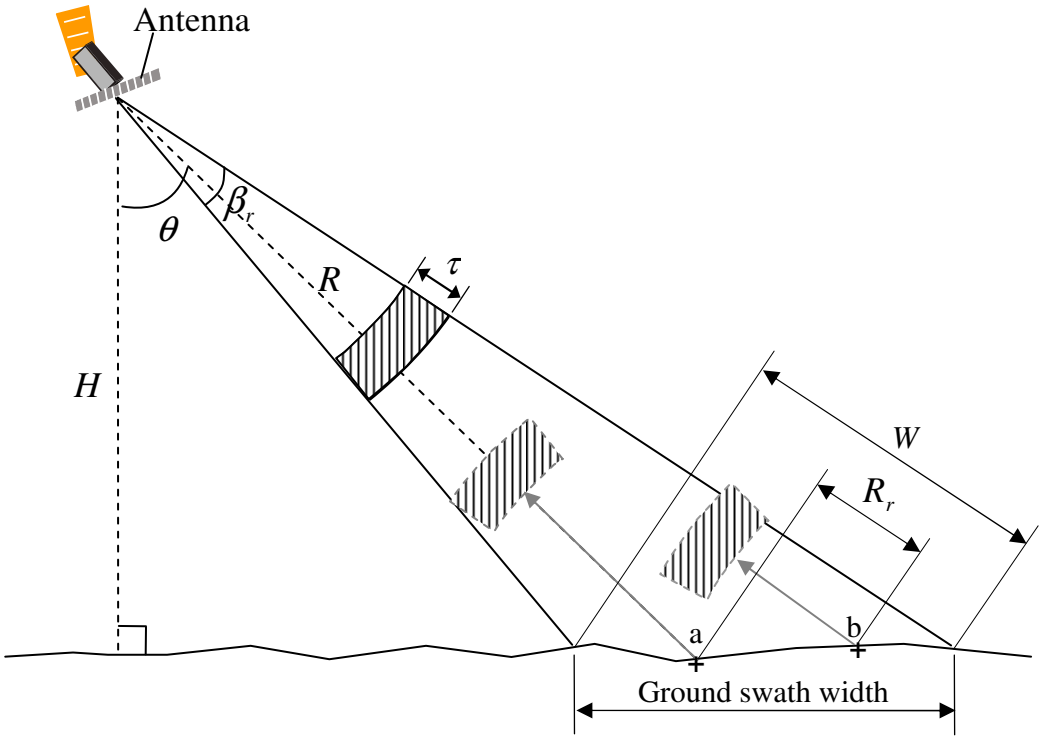

Figure 2.1. Geometric principle of SAR: A view in the flight direction of the satellite illustrating the slant range swath, W, range resolution, R_r, range direction beamwidth, β_r, and pulse duration, τ, and slant range distance R, and look angle θ.

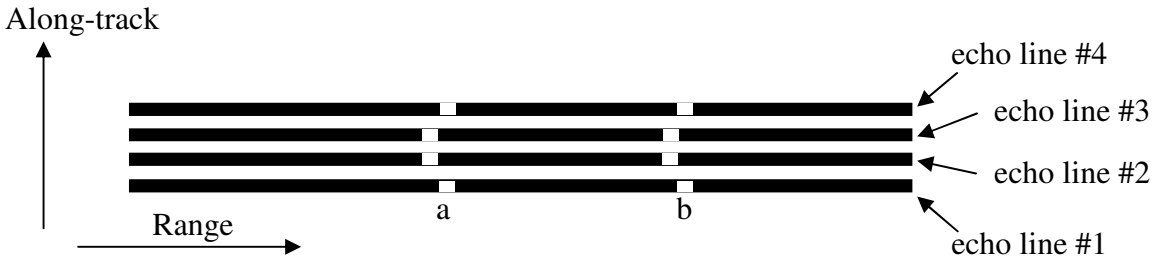

Figure 2.2. Echo display in two dimensions.

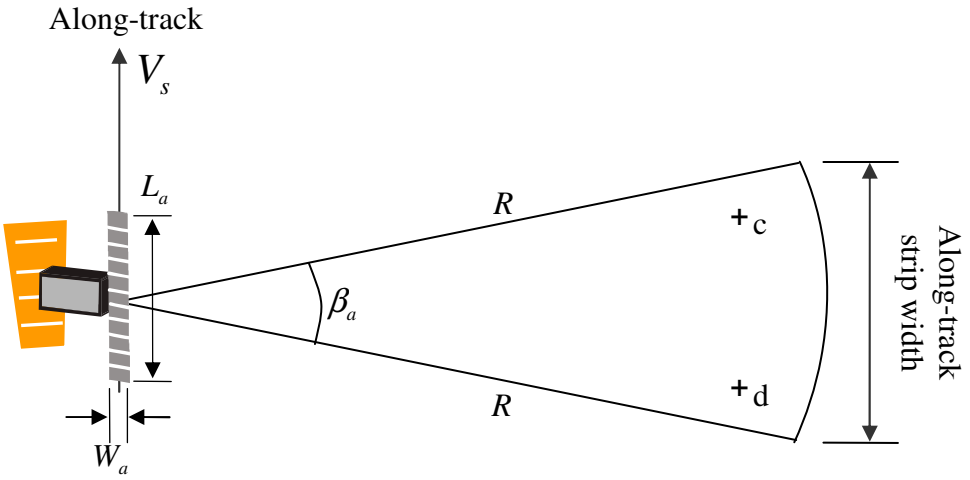

Figure 2.3. SAR geometry viewed from a direction orthogonal to the slant range and along the track-axis with an antenna size of $L_a \times W_a$ (length×width)

2.2.2 Along-track Resolution

In the along-track direction, any conventional SLAR has the resolution of [Curlander and McDonough, 1991]

$$R_a = R\beta_a = \frac{R\lambda}{L_a} \tag{2.3}$$

where β_a is the radar beamwidth in the along-track direction which is the ratio of the wavelength λ to the SAR antenna length along-track L_a (Figure 2.3). Nominal values for the ERS wavelength and antenna length are 5.6 cm and 10 m, respectively. Through equation (2.3), we can find that the ERS satellites with the slant range of $R = 800$ km can have an along-track resolution of 4.5 km in length. It means that objects in the 4.5 km range are expressed as one pixel in the image, which is unacceptable for most scientific purposes. Better resolution is achievable through a larger antenna, but often it is impractical to carry an extremely long antenna such as 500 m or even a couple of kilometers. To overcome this problem, similar processing technique as applied to the range direction over the chirp signal is introduced to the Doppler shift frequency in the along-track direction. This is another type of frequency-modulated chirp signal, induced by the relative velocity of the satellite to ground targets. For a point target P at slant range R and along-track coordinate x relative to the radar, the Doppler shift relative to the transmitted frequency is (Figure 2.4) [Curlander and McDonough, 1991; Hanssen, 2001]

$$f_D = \frac{2V_s \sin(\beta_a / 2)}{\lambda} \approx \frac{2V_s x}{\lambda R} \tag{2.4}$$

where V_s is the relative velocity, and $\beta_a / 2$ is the off angle from broadside shown in Figure 2.4. Given the Doppler frequency, the along-track position, x, is computed and a position can be located on the range-Doppler coordinate of (R, x). With the use of Doppler analysis of the radar returns, the along-track resolution δx is related to the resolution δf_D of the measured Doppler frequency. From the formula (2.4), the azimuth resolution, R_a, is

$$R_a = \delta x = \left(\frac{\lambda R}{2V_s} \right) \delta f_D \tag{2.5}$$

Furthermore, the measurement resolution in the frequency domain is nominally the inverse of the time span S of the waveform being analyzed [Curlander and McDonough, 1991]. Since this time is potentially the time during which a target remains in the beam, we have from Figure 2.3 and $\beta_a = \lambda / L_a$ that

$$(\delta f_D)^{-1} = S = \frac{R\beta_a}{V_s} = \frac{R\lambda}{L_a V_s} \tag{2.6}$$

Putting equation (2.6) into equation (2.5), we have the along-track resolution of [Curlander and McDonough, 1991]

$$R_a = \left(\frac{\lambda R}{2V_s}\right)\left(\frac{L_a V_s}{R\lambda}\right) = \frac{L_a}{2} \tag{2.7}$$

According to this equation the shorter antenna gets the better resolution in the along-track direction which is in contrast to the result from the conventional resolution in SLAR. Also unlike the along-track resolution of SLAR (equation (2.3)), the SAR along-track resolution is independent of the slant range R. It is a great advantage especially to satellite SAR systems, which usually operate at an altitude of several hundred kilometers.

By defining the Doppler bandwidth

$$B_D = \frac{\beta_a V_s}{\lambda} \tag{2.8}$$

equation (2.7) is rewritten as

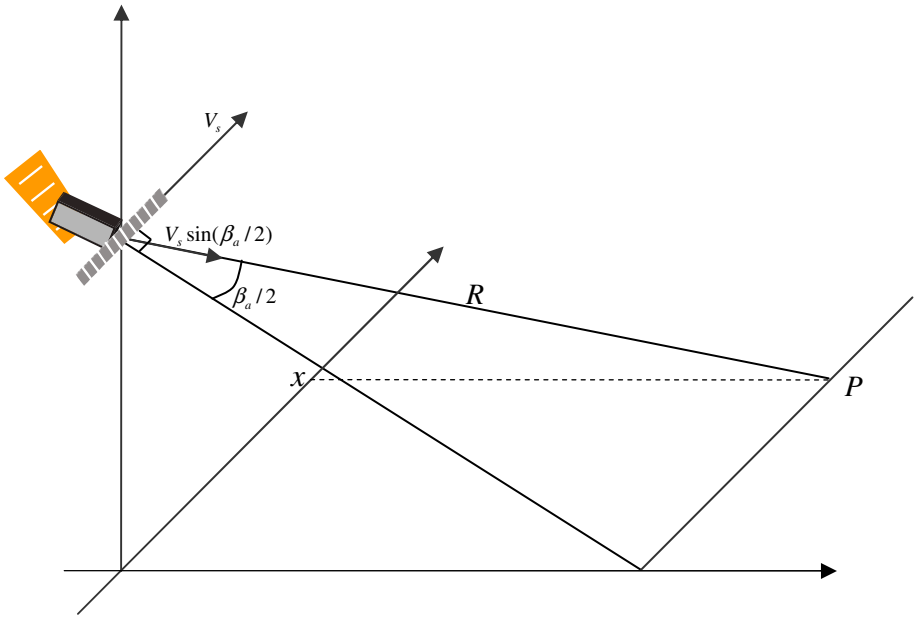

Figure 2.4. Three-dimensional view of SAR geometry.

$$R_a = \frac{V_s}{2B_D} \tag{2.9}$$

This is in analogy of the range resolution expressed by equation (2.2). While the resolution is proportional to the speed of light in the range, or the velocity of the satellite in the along-track direction, respectively, each resolution is inversely proportional to the bandwidth.

2.3 Geometric Distortion in SAR

In two-dimensional images, the side-looking geometry of SAR causes distortions such as layover, foreshortening, and shadow: 1) when the terrain slope exceeds the incidence angle of the SAR, the mapping from ground range to slant range gets inverted (layover) 2) when the terrain tilted towards the sensor appears squeezed in the SAR image (foreshortening), and 3) the terrain behind steep mountains at shallow incidence angle is shadowed and appear as black in the image (shadow). As can be shown over A-B in Figure 2.5, the top of the object, i.e., B in this case, is laid over relative to its base, i.e., A, on SAR image. The ground distance C-D is represented on radar images as shortened (compressed) distance C'-D'. Ground surface D-E is not illuminated by the radar. Since no radar signal is received, radar shadow appears very dark on the SAR image. Due to the increase of incidence angle at the far side, shadow occurs more frequently at the far side than at the near side.

2.4 InSAR Geometry and Equation

The InSAR acquisition geometry is shown in Figure 2.6 and from this the physical and the geometrical relationship between the two phase observations to obtain topographic height and surface deformation estimates can be derived. Both ERS-1 and

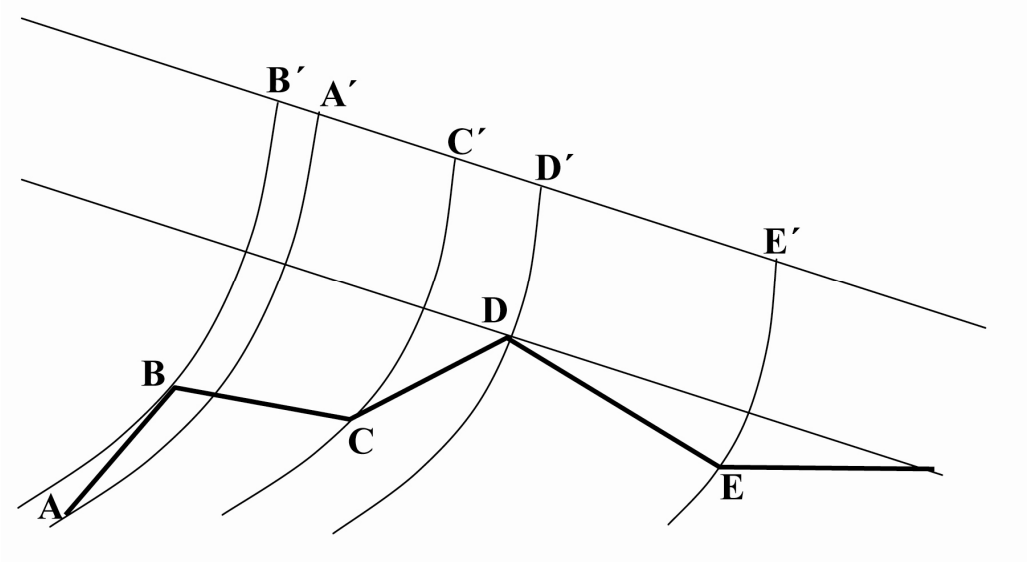

Figure 2.5. Geometric distortions in SAR.

-2 SAR images are acquired at the positions of S_1 and S_2 in the figure at different epochs. The distance between the two positions is referred to as an interferometric baseline which consists of perpendicular baseline $B_\perp$ and parallel baseline $B_\parallel$ to the reference look direction $\overline{S_1C}$ where C is a center point of image on the reference surface. In case of a single-pass interferometric system such as SRTM, two images are taken at the same epoch. The first satellite is at altitude H and the slant distance between S_1 and point P on the surface is R_1.

Observed points in two images with regular grids are expressed as [Hanssen, 2001]:

$$y_1 = |y_1| \exp(j\psi_1) \tag{2.10a}$$

$$y_2 = |y_2| \exp(j\psi_2) \tag{2.10b}$$

where $j = \sqrt{-1}$, 'exp' denotes the exponential function, and $|y_i|$, ψ_i are amplitude and phase for the respective point in image i, respectively. In these equations, phase in the exponential is defined as modulo 2π. After re-sampling the second image y_2 to corresponding locations in the first image y_1, complex multiplication yields the complex interferogram:

$$U = y_1 y_2^* = |y_1||y_2| \exp(j(\psi_1 - \psi_2)) \tag{2.11}$$

where the superscript, *, indicates the conjugate of a complex variable.

The observed phase values ψ_1 and ψ_2 in the two images for a certain resolution cell are

$$\psi_1 = -\frac{4\pi R_1}{\lambda} + \psi_{scat,1} \tag{2.12a}$$

$$\psi_2 = -\frac{4\pi R_2}{\lambda} + \psi_{scat,2} \tag{2.12b}$$

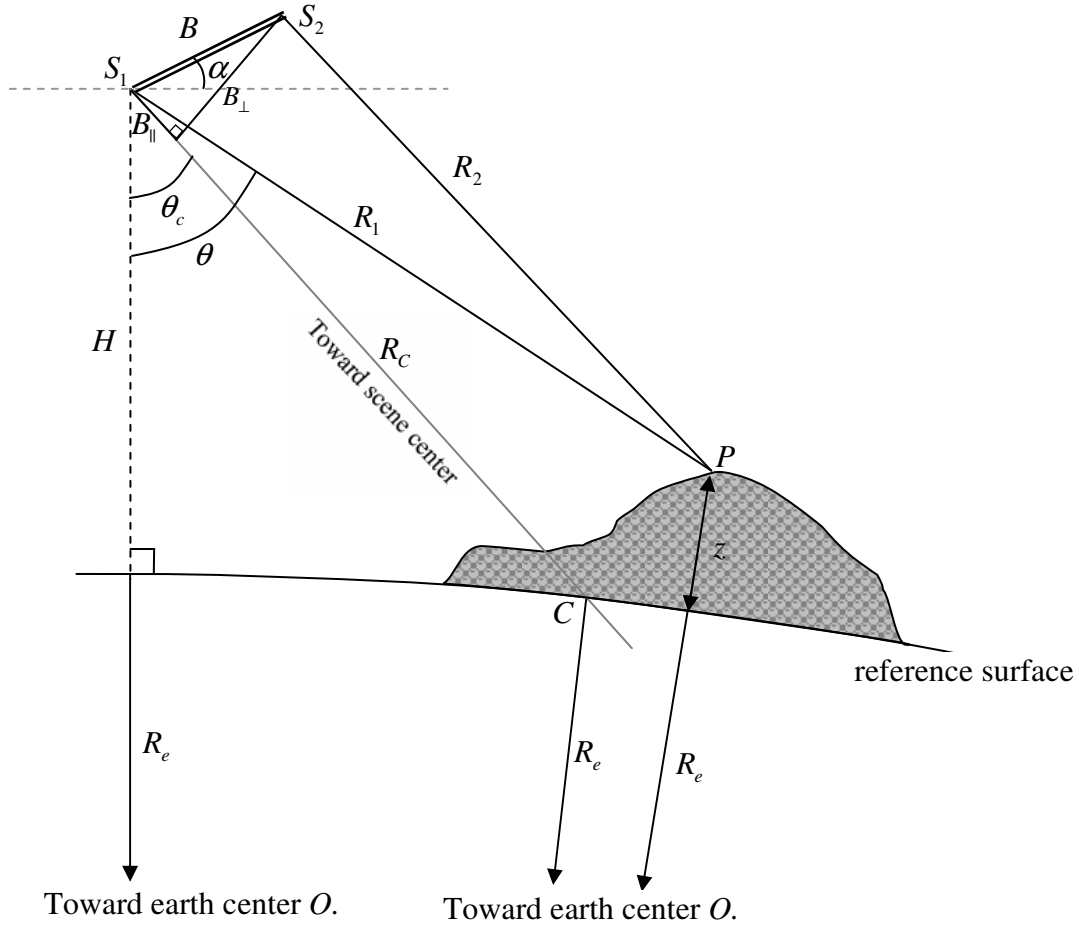

Figure 2.6. Geometry of the interferometric SAR system. Satellite flight paths are perpendicular to the plane and R_e is a radius for a reference earth surface.

where R_1 and R_2 are the slant range between the satellite and a position on the ground, λ denotes the wavelength (e.g. 5.6 cm for ERS), and $\psi_{scat,1}$ and $\psi_{scat,2}$ are the scattering phases within a resolution cell in the two images, respectively. The minus sign is induced from the Doppler frequency in equation (2.4) which can be rewritten as:

$$f_D = \frac{2V}{\lambda} = -\frac{2}{\lambda}\frac{\partial R}{\partial t} \tag{2.13}$$

where $V = V_s \sin(\beta_a / 2)$. It means that as range decreases, the Doppler frequency is positive and makes the wavelength shorten. Since the frequency is obtained by differentiating the phase, $\partial\psi / \partial t = 2\pi f(t)$, we have

$$\psi(t) = -\frac{4\pi R(t)}{\lambda} \text{ (modulo } 2\pi \text{)} \tag{2.14}$$

For the simplicity of the notation, range and phase as functions of time t are expressed simply as R and ψ in the rest of this dissertation.

If the scattering characteristics are equal, which means there are no changes in its backscattering characteristics on the surface over both acquisitions, the interferometric phase ϕ can be written as:

$$\phi = \psi_1 - \psi_2 = -\frac{4\pi(R_1 - R_2)}{\lambda} = \frac{4\pi\Delta R}{\lambda} \tag{2.15}$$

To demonstrate the superiority of using InSAR in determination of range difference to the conventional methods, first the stereometry method [Franceschetti and Lanari, 1999] is introduced. From the two-pass InSAR geometry in Figure 2.6, the angle of elevation θ can be determined by the law of cosines:

$$\sin(\theta - \alpha) = \frac{R_1^{\,2} + B^2 - R_2^{\,2}}{2R_1 B} \tag{2.16}$$

and from the knowledge of θ, the object's elevation z can be determined from

$$z = H - R_1 \cos\theta \tag{2.17}$$

This process is very sensitive to errors in the determination of the range difference $\Delta R = R_2 - R_1$ [Cheney, 2001]. By applying the chain rule, we get

$$\frac{dz}{d(\Delta R)} = \frac{dz}{d\theta}\frac{d\theta}{d(\Delta R)} = R_1 \sin\theta \frac{d\theta}{d(\Delta R)} \tag{2.18}$$

and calculate the derivative $d\theta / d(\Delta R)$ implicitly from (2.16) with $R_2 = R_1 + \Delta R$

$$\frac{d\theta}{d(\Delta R)} = \frac{-(R_1 + \Delta R)}{BR_1 \cos(\theta - \alpha)} \tag{2.19}$$

Using this in (2.18) gives

$$\frac{dz}{d(\Delta R)} = -\frac{(R_1 + \Delta R)\sin\theta}{B\cos(\theta - \alpha)} = -\frac{R_2 \sin\theta}{B\cos(\theta - \alpha)} \tag{2.20}$$

For spaceborne SAR systems, the ratio of R_2 to B is very large, i.e., $R_2 >> B$. As error in ΔR is determined in m-level, the height error will reach up to several hundred meter or even a couple of km. For example, in the ERS system the range resolution is about 10 m and an obtainable accuracy in range difference by image registration techniques is at most 1/20th of the pixel [Franceschetti, G. and R. Lanari, 1999] which yields the height accuracy of 1.5 km using nominal ERS parameter values in (2.20) such as R_2=800 km, θ=23°, and B=100 m. It is for this reason that many SAR systems use instead an interferometric method to estimate ΔR and thus find the ground topography. As can be shown in (2.15), InSAR determines the range difference ΔR from phases from two SAR images. In ERS systems, with an assumption of a phase standard deviation of 30° [Franceschetti, G. and R. Lanari, 1999], the range error is computed to be 0.2 cm by equation (2.15). Plugging this value in equation (2.20), we get a height accuracy of about 7 m.

Now, to demonstrate the factors influencing the interferometric phase, several approximations are introduced in the following paragraphs. Using the approximation $(R_1 + \Delta R)^2 \approx R_1^{\,2} + 2R_1\Delta R$ and $R_1 >> B$, the interferometric phase, ϕ, can be expressed, using (2.15) and (2.16), as:

$$\phi \approx -\frac{4\pi B \sin(\theta - \alpha)}{\lambda} \tag{2.21}$$

By applying the Taylor expansion of ϕ around θ_c shown in Figure 2.6, we finally get [Zebker et al., 1994b; Sansosti et al., 1999] from (2.18)

$$\phi \approx -\frac{4\pi}{\lambda}\left(B\sin(\theta_c - \alpha) + B\cos(\theta_c - \alpha)\frac{z}{R_1 \sin\theta}\right) = -\frac{4\pi}{\lambda}\left(B_{\parallel} + B_{\perp}\frac{z}{R_1 \sin\theta}\right) \tag{2.22}$$

where $B_{\parallel}$ and $B_{\perp}$ are baseline components parallel to and perpendicular to the line of sight from S_1 to the point on the reference surface center in Figure 2.6. Slant range to the center look angle to the reference surface, R_c, can be computed from three information- the slant range to the first pixel, R_0, a range pixel size, and number of pixel of an image to have $R_c = R_0 + (\text{pixel size}) \times (\text{number of pixel to image center})$. Look angle to the image center of the reference surface, θ_c, is computed from the trigonometry of $\Delta S_1 CO$ where O is the center of earth.

Equation (2.22) is for the case of no deformation on the surface over the data acquisition times. As we consider both the influence of topography, z, and surface

deformation along the line of sight, D, in the interferometric phase differences, relative to the reference body, the above equation yields:

$$\phi \approx \phi_{topo} + \phi_{def} = -\frac{4\pi}{\lambda}\left(B_{\parallel} + B_{\perp}\frac{z}{R\sin\theta}\right) + \frac{4\pi}{\lambda}D \tag{2.23}$$

where R is substituted for R_1 for simplicity. It shows the proportional relationship between observed phase ϕ and height z above the reference body. By differentiating equation (2.23) with respect to height, we get

$$\frac{d\phi}{dz} = -\frac{4\pi}{\lambda}\frac{B_{\perp}}{R\sin\theta} \tag{2.24}$$

By differentiating equation (2.23) again with respect to surface deformation along the line of sight D, we find

$$\frac{d\phi}{dD} = \frac{4\pi}{\lambda} \tag{2.25}$$

Since $R >> B_{\perp}$, the phase change caused by height in equation (2.24) is less sensitive than the phase sensitivity to the deformation in equation (2.25) which is an advantage when using InSAR for deformation studies. It is also noted that while the topography is sensitive to the baseline, the deformation is independent of the baseline (as long as $R_1 \approx R_2$).

To separate a constant and linear deformation signal from equation (2.23), the differential interferometric method [Kwok and Fahnestock, 1996] between two interferograms I and II is introduced.

$$\Phi = \phi_I - \phi_{II} \approx -\frac{4\pi}{\lambda}\left(\frac{B_{\perp,I} - B_{\perp,II}}{R\sin\theta}\right)z \tag{2.26}$$

2.5 Differential Interferometry

Once given the deformation-free interferogram, deformation signals can be computed by differentiating between deformation-free and deformation/topography-induced interferograms. Deformation-free interferograms could be obtained either from an external DEM [Massonnet et al., 1993, 1994, 1995a, 1995b, 1998] or from another InSAR image. Depending on the way of generating deformation-free interferograms, there are three kinds of methods in differential interferometry: two-pass, three-pass, and four-pass interferometry.

The two-pass method is a combination between an interferogram from a pair of SAR scenes and another interferogram from an external digital elevation model (DEM).

An interferogram from SAR images has both a topographic phase and deformation phase. The idea of a two-pass interferogram is to separate the deformation phase by subtracting the topography related phase simulated from the DEM. Based on the SAR geometry, the interferometric baseline model, and the transformed height map from DEM into SAR coordinates, the unwrapped interferogram corresponding to topography is calculated. If there is an accurate DEM, it would be used for land deformation studies. However, often for remote places, (e.g., Antarctica), using the two-pass interferometric method has great limitations due to the lack of an accurate DEM.

Three-pass differential interferometry is a combination between three SAR images according to Zebker et al.[1994b]. One of them is used as a common image in the forming of two interferograms out of three SAR images. For example, in the time span of one three-day repeat orbit, the satellite passes over the same area three days apart continually. Once we have an image at epoch A before a certain surface deformation and an earthquake has occurred between epoches B and C, any deformation due to the earthquake is possible to be extracted by subtracting the two interferograms from A-B and B-C. We assume that the interferogram from A-B has only a topographic phase, whereas interferogram from B-C has both topographic and deformation phases [Gabriel et al., 1989; Zebker et al., 1994b; Peltzer and Rosen, 1995]. One of the advantages of the three-pass differential interferometric method is no need of any DEM over the study area. However, acquiring the timely data covering the study area is a challenging matter. Also due to the subtraction between two interferograms from different baselines, two individual interferograms should be unwrapped before the subtraction. It could cause a problem of depending on the baseline and slope of a study area: For the same area, an unwrapping procedure could be more difficult over an image from a longer baseline than an image from a smaller baseline, and a stiff area resulting in more interferometric fringes is more difficult than gentle sloping areas.

Four-pass differential interferometry needs two interferograms independent of each other. Similar to the three-pass interferometry, between two independent interferograms, one interferogram is assumed to have a deformation phase along with a topographic phase, while the other interferogram is free from the deformation. Like the three-pass interferometry, it is not necessary to have a DEM for the study area. One may select between three- and four-pass methods according to the data availability over the study area.

2.6 Speckle

A pixel value in a SAR image is not one of the several echoes from the image resolution cell but the sum of the backscattering of various kinds of objects in the resolution cell and hence there could be big differences even between neighboring pixels, which yields an image of 'salt and pepper.' A common approach for reducing this sort of speckle is to average independent estimates of images [Fitch, 1988]. Multilooking reduces the phase noise by approximately $\sqrt{L}$ [Madsen and Zebker, 1999] where L is the number of looks defined in equation (2.27). In this way, we obtain a noise-reduced and squared image with the same pixel size both in range and along-track directions at some

loss of resolution in the image. The number of looks is computed based on azimuth and range resolution, pixel size, and averaging pixel sizes such that [Zebker et al., 1994a]:

$$L = \frac{A_p}{R_a R_r} \tag{2.27}$$

where A_p is the ground area of the multilook pixel, and R_a and R_r are the ground resolutions in along-track direction and range, respectively.

2.7 Errors in Topographic Estimation and Deformation

The consistency of the interferogram can be checked using a correlation coefficient. It is a measure of the correspondence of both SAR images and is estimated by window-based computation of the magnitude of the complex cross-correlation coefficient $|\rho|$ of the SAR images over an estimation window of N pixels [Seymour and Cumming, 1994; Hanssen, 2001], namely:

$$|\hat{\rho}| = \frac{\left|\sum_{n=1}^{N} y_1^{(n)} y_2^{*(n)}\right|}{\sqrt{\sum_{n=1}^{N} \left|y_1^{(n)}\right|^2 \sum_{n=1}^{N} \left|y_2^{(n)}\right|^2}} \tag{2.28}$$

For completely coherent scatterers, $|\rho| = 1$ holds, whereas $|\rho| = 0$ when the scattered fields are independent of each other. The magnitude $|\rho|$ is relative to a measure of the phase noise, and it can also be used as a tool for image classification insofar as the different levels of coherence correspond to different ways of surface backscattering. It has been shown that the resulting standard deviation of the phase noise, σ_ϕ, at a given degree of coherence, $|\rho|$, can be approximately written as [Rodriguez and Martin, 1992; Hagberg et al., 1995]:

$$\sigma_\phi = \frac{1}{\sqrt{2L}} \frac{\sqrt{1-|\rho|^2}}{|\rho|} \tag{2.29}$$

The complex coherences can either be estimated from the interferometric data or derived theoretically, based on the known sensor characteristics, acquisition circumstances, and signal processing algorithms [Zebker and Villasenor, 1992; Joughin, 1995; Hanssen, 2001]. Total correlation (or coherence) may be introduced by the multiplication of individual correlation coefficients [Zebker and Villasenor, 1992]:

$$\rho = \rho_{thermal} \rho_{base} \rho_{temporal} \tag{2.30}$$

where $\rho_{thermal}$ is related to the noise caused by the characteristics of the system as well as

the antenna characteristics, ρ_{base} to noise of the image acquisition geometry or baseline, and $\rho_{temporal}$ to the noise of temporal terrain change in repeat-pass InSAR. The absolute value of the system coherence $\rho_{thermal}$ is sometimes described as a function of the signal-to-noise ratio (SNR) [Zebker and Villasenor, 1992; Bamler and Just, 1993; Hanssen, 2001]

$$\left|\rho_{thermal}\right| = \frac{1}{1 + SNR^{-1}} \tag{2.31}$$

The baseline correlation term is introduced as:

$$\left|\rho_{base}\right| = \frac{B_c - B_\perp}{B_c} \tag{2.32}$$

where B_c is the critical baseline. The critical baseline is the maximum horizontal separation of the two satellites allowing interferogram generation. It is the baseline that causes a spectral shift equal to the bandwidth B_W [Zebker et al., 1992; Hoen and Zebker, 2000; Hanssen, 2001] and is defined as

$$B_c = \frac{\lambda B_W}{c} R \tan(\theta - \alpha) = \frac{\lambda}{R_r} R \tan(\theta - \alpha) \tag{2.33}$$

From the C-band ($\lambda = 5.6\,\text{cm}$) ERS parameters, the critical baseline B_c is about 1 km while JERS-1 using the L-band ($\lambda = 23.5\,\text{cm}$) has a critical baseline of about 7 km. By determining $\left|\rho\right|$, it is possible to obtain the standard deviation of the local height, σ_z, of a DEM generated from a SAR repeat-pass interferogram [Li and Goldstein, 1990; Rodriguez and Martin, 1992; Hagberg et al., 1995]

$$\sigma_z = \frac{\lambda}{4\pi} \frac{R \sin\theta}{B_\perp} \sigma_\phi \tag{2.34}$$

following (2.24).

As can be shown through the relationship between phase error and coherence in equation (2.29), the phase error could be explained by thermal noise in the SAR system as well as by environmental changes of the surface target. The elevation error caused by phase error is inversely proportional to the baseline length so that long baselines are important for the reduction of elevation error. But long baselines cause more decorrelation, which increases the phase error and, thus, the elevation error. This requires that these opposing influences of baseline length on the elevation error be balanced in order to minimize it [Rodriguez and Martin, 1992].

2.8 Limitation of InSAR as a Geodetic Tool

Interferograms are made only if the coherency condition is met between two image acquisitions. This condition limits the upper boundary of the interferometric measurement slope to about 10^{-3} which translates into 3mm/m [Massonet and Feigl, 1998]. Rapid changes on the surface such as an earthquake and a volcanic eruption can easily exceed this limit. The lower limit of the interferometric phase slope, given by 10^{-7} in Figure 2.7, is determined by the ratio between range change and the measurement uncertainty [Massonet and Feigl, 1998]. The lower limit is mainly due to orbit inaccuracies and long wavelength atmospheric gradients [Hanssen 2001]. The side-looking antenna has a pointing of probably no better than ±0.07 degree which corresponds to ±1 km error on the ground. This is would be the minimum error one gets on the ground – not to mention orbit errors. Signals from solid earth tides and even more so for postglacial rebound are hard to detect since they have broad or long spatial wavelengths with respect to the imaging system. In other words, the magnitude of the deformation signal is too weak to be detected in imaging swath, and the phase slope is smaller than the lower boundary value of 10^{-7}. The horizontal axis of Figure 2.7 shows the characteristic spatial width of the imaging system and several geophysical phenomena. While the left end of the horizontal axis is a limit caused by the pixel size, the right side is a limitation due to the swath width of the system.

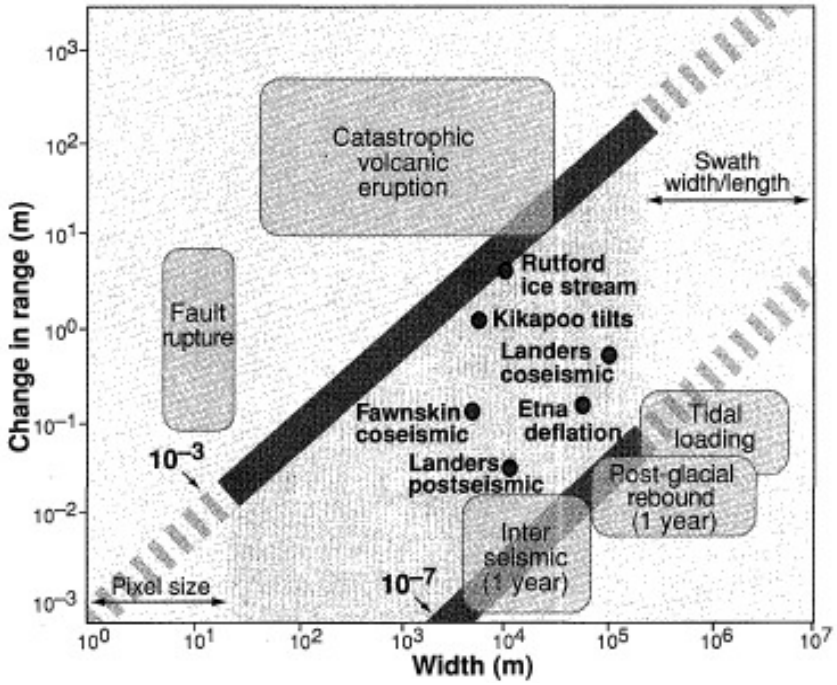

Figure 2.7. Scope of InSAR applications in deformation studies. [Meade and Sandwell, 1996]

2.9 Advanced InSAR Missions and Techniques

To have better resolution and accuracy in InSAR products, the use of shorter wavelengths in the X-band has been introduced, and to meet this end, a new German SAR mission TerraSAR-X will be launched in December 2006. Its Spotlight, StripMap, and ScanSAR modes acquire images with up to 1, 3, and 16 m resolution respectively. Later the TanDEM-X mission, proposed for launch in 2008 as a TerraSAR-X add-on mission, is expected to provide a global DEM with unprecedented accuracy of a couple of meters vertically. It will acquire SAR images using a tandem formation of two satellites, TerraSAR-X and TanDEM-X. On the other hand, by using the longer wavelengths of the L-band, the ALOS of the JAXA will be useful over vegetated or other rapidly-changing surfaces and will be used as a complement to existing satellites. The Radarsat-2, C-band Canadian SAR satellite, scheduled to be launched in October 2006, has an ultra-fine beam mode to achieve 3 m resolution, and its product can be useful in detecting objects even for military purposes.

Envisat ASAR and ALOS have a wide swath mode which can acquire images over 300 ~ 450 km at the cost of resolution. They are beneficial in studying phenomena over wide areas, for which the previous satellites have too narrow coverage, i.e., about 70~100 km. Radarsat-2 can increase the revisit frequency using right and left looking modes, and it allows frequent observation for areas of interest, hence having coherence between visits. When the radar wave interacts with a surface, the polarization is modified based on the properties of the surface. Polarization refers to the orientation of the radar beam relative to the earth's surface. Radar systems can be configured to transmit and receive either horizontally or vertically polarized electromagnetic radiation. Depending on the type of the polarization, backscattering characteristics are different and the polarization response can be used for surface information. In general it was known that the use over bare ground of co-polarization (or like-polarization where, HH or VV for energy is transmitted and received horizontally or vertically, respectively,) shows greater response than cross-polarization, i.e., HV or VH. By applying different types of polarization over the same area, we can have more information over it. New SAR missions are able to use single or dual polarization in HH, VV, HV, and VH combinations to increase our understanding of the study area. The advent of the aforementioned several SAR missions will provide data integration from various sources, a more complete coverage, and increased accuracy due to shorter revisiting times and higher resolutions.

Due to the temporal and geometrical decorrelation, InSAR application is limited to be used in specific areas of study and also in some locations on the earth surface. The Permanent Scatterer (PS) InSAR technique provides time series for selected points on the image even over several years [Ferretti et al., 2001]. Through this technique, the decorrelation problem in InSAR applications such as subsidence studies could be overcome. For example, in tectonic research the phase change as a function of time corresponding to each PS can be related to the scatterer motion even if all the surrounding pixels are totally incoherent [Rocca et al., 2000].

CHAPTER 3

INSAR DEM GENERATION

3.1 Introduction

The use of InSAR is very effective for studying the ice mass balance of polar regions and its contribution to global sea level change [Rignot and Thomas, 2002]. An accurate, high-resolution DEM referenced within a well-defined terrestrial reference frame (TRF) is an inherent requirement to facilitate the use of InSAR to conduct these studies in remote polar regions. Conventional optical stereographic mapping uses the parallax, which is directly related to angle-measurements. Besides the need of illumination, it requires identical features, so-called 'conjugate points,' in both images, which poses problems in snow/ice covered areas in polar regions. In Figure 3.1, an image from Advanced Spaceborne Thermal Emission and Reflection (ASTER) on Earth Observation Satellite over our study area is given along with the DEM. As can be seen from Figure 3.1(a), its surface is covered with ice and snow and hence very smooth which makes it difficult to find a distinct feature. Consequently, no common features could be found which yields many "holes" in the stereographic DEM seen in Figure 3.1(b).

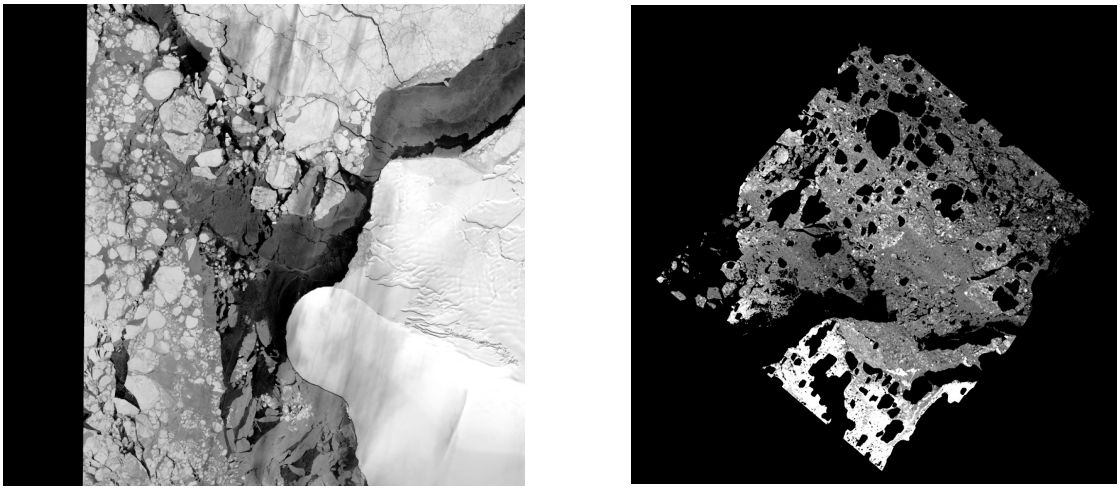

(a) (b)

Figure 3.1. (a) Optic image (ASTER) over the study area (image center coordinates around 158.72°W, 76.45°S), and (b) stereographic DEM from ASTER images.

An InSAR DEM over polar regions has advantages over the conventional optical stereographic DEM because of its active sensor characteristic and since there is no need for conjugate points in the images. Still it needs GCPs to refine the baseline. However, ERS orbits are not known well enough to estimate the baseline with the level of accuracy needed to generate DEMs and estimate deformation [Zebker et al., 1994a]. As a result, the baseline must be determined using tie points [Joughin et al., 1996; Zebker et al., 1994a]. In this dissertation, the baseline is modeled as a linear function of the along-track coordinate [Joughin et al., 1996] and the DEM is defined as geocentrically referenced to a terrestrial reference frame (TRF). The International TRFs (ITRFs) to which the ERS and the ICESat precise orbits are referenced, namely ITRF95 and ITRF2000, are used, respectively. In the context of the DEM study, both ITRF systems have practically the same accuracy for the InSAR and ICESat altimetry analyses. The generation of an accurate (meters) and high-resolution (60-m) DEM over grounded ice and floating ice shelves is demonstrated, using laser altimetry profiles acquired by the ICESat, thereby eliminating the need for in-situ GCPs. The study area Sulzberger Bay is located at 76.5 °S to 77.5 °S and 153 °W to 159 °W by the Ross Sea, West Antarctica, and is one of the major drainage outlets of the West Antarctic Ice Sheet.

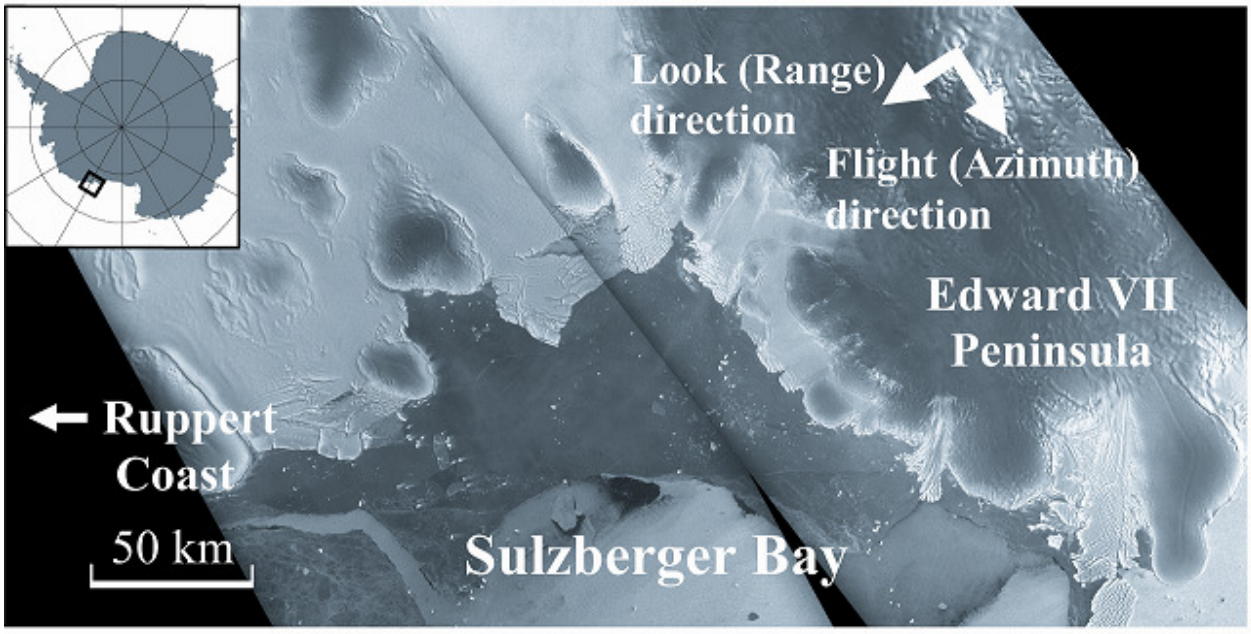

Figure 3.2. Sulzberger Bay, West Antarctica.

3.2 Methodology

Figure 3.3 shows the diagram for the DEM generation scheme by the four-pass differential interferometric method in this research. Six interferograms are generated and each interferogram contains topographic, horizontal, and vertical deformation phases. The topographic phase is proportional to the perpendicular base line, $B_{\perp}$, and horizontal deformation is assumed to be constant and linear. By subtracting two interferograms, one may have another interferogram with horizontal deformation-free and topographic phase corresponding to a differenced baseline, $B_{\perp}^{1} - B_{\perp}^{2}$. A DEM by Sulzberger Bay, West Antarctica, is presented which was developed using 12 ERS SAR scenes and 19 ICESat laser altimetry profiles. Differential interferograms from the ERS tandem mission SAR scenes, acquired in the austral fall of 1996, have been employed as well as four selected ICESat laser altimetry profiles, acquired in the austral fall of 2004, in lieu of GCPs to construct an improved geocentric 60-m resolution DEM over the grounded ice region. The DEM is then extended to include two ice shelves by using ICESat profiles via Kriging. Fifteen additional ICESat profiles acquired in 2003-2004 are used to assess the accuracy of the DEM. After accounting for radar penetration depth and predicted surface

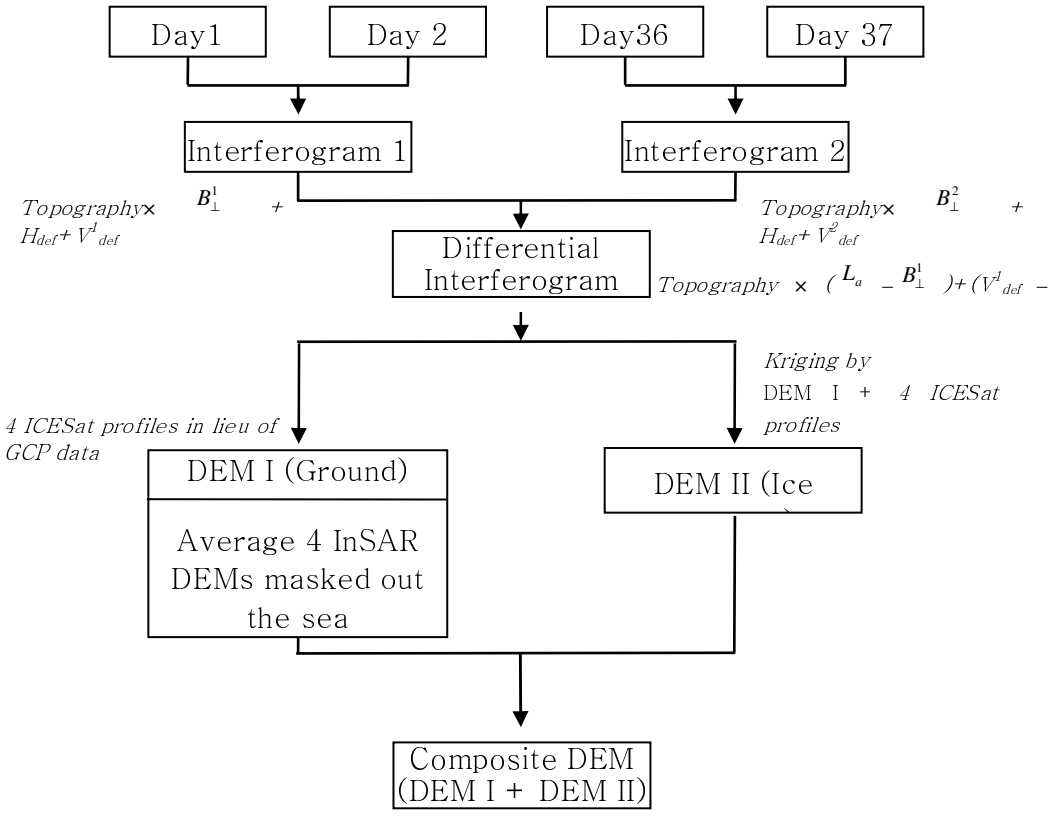

Figure 3.3. Diagram for DEM generation.

changes, including effects due to ice mass balance, solid Earth tides, and glacial isostatic adjustment, in part to account for the eight-year data acquisition discrepancy, the resulting difference between the DEM and ICESat profiles is 0.57 ± 5.88 m. After removing the discrepancy between the DEM and ICESat profiles for a final combined DEM using a bicubic spline, the overall difference is 0.05 ± 1.35 m.

3.3 Datasets

3.3.1 SAR Data

SAR data used in this dissertation are all from ERS-1 and ERS-2 tandem missions in 1996. The European Space Agency launched ERS-1, its first SAR satellite, in July 1991. It was designed primarily to monitor polar oceans and ice with the look angle of 23°. With this small look angle, vertical deformation is more sensitive than the horizontal deformation. For the system verification, data validation, and InSAR experiments, it was operated in a three-day repeat orbit. Later, to meet various scientific purposes, its repeat pattern was changed to 3, 35, and 168 days. ERS-1 is operated in a sun-synchronous near-polar orbit (inclination of 98.5°) with an altitude of about 780 km. The ERS system transmits microwaves in the vertical direction and receives in the vertical direction, which is called VV polarization. In the single-look complex (SLC) image the pixel size corresponds to 4 m in the along-track direction and to 20 m in the range direction. As

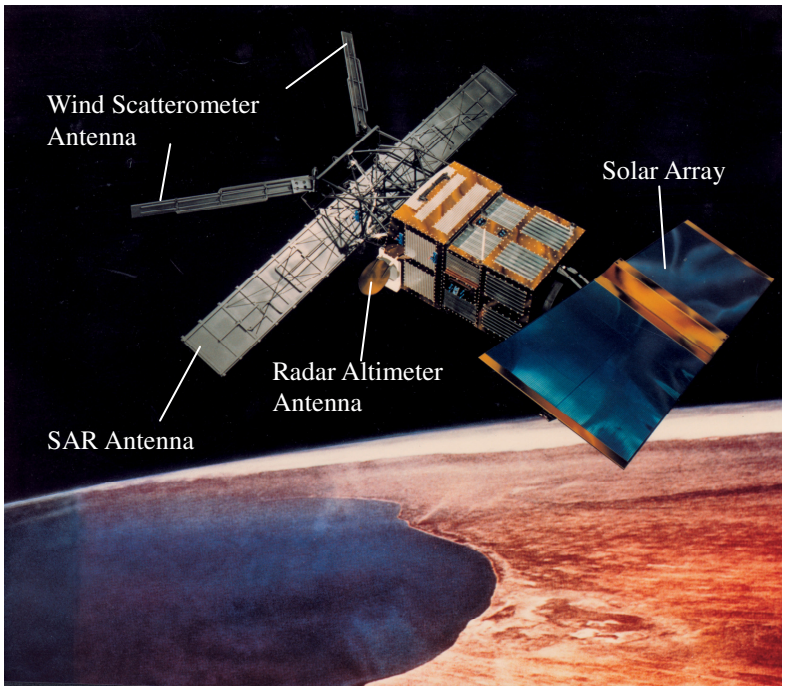

Figure 3.4. ERS Satellite image © European Aeronautic Defence and Space Company (EADS) Astrium.

explained before, by taking looks with the ratio of 5 to 1 in along-track and range direction, respectively, a squared image is acquired at the cost of resolution. ERS-2, the twin satellite of ERS-1, was launched in April 1995. It was operated in tandem with ERS-1 for 9 months between October 1995 and June 1996 to provide image pairs with 24-hour revisit times which is advantageous in forming SAR interferometry. Table 3.1 shows the important parameters for the ERS satellites, and Table 3.2 is for different repeat orbit phases of ERS-1.

Parameters	Value
Wavelength, cm	5.6(C band)
Frequency, GHz	5.30
Antenna Size (Length by width)	10 m by 1m
Polarization	VV
Incidence angle, deg	23
Altitude, km	790
Pulse repetition rate, Hz	1679
Sampling rate, MHz	18.96
Pulse length, μsec	37.1
Range bandwidth, MHz	15.55
Slant range resolution, m	10.2
Ground range resolution, m	25
Along-track resolution, m	6
Single-look range pixel size, m	20
Single-look along-track pixel size, m	4
Swath width, km	100
Inclination, deg	98.5
Repeat cycles*, days	3, 35, 168

Table 3.1. ERS parameters (* more information on repeat cycles for ERS-1 is listed in Table 3.2.).

Phase	Date	Repeat days
Phase A	31 Jul 1991	Commissioning (3-days)
Phase B	28 Dec 1991	Ice (3-days)
Phase C	2 Apr 1992	Multi-Disciplinary (35-days)
Phase D	23 Dec 1993	Ice (3-days)
Phase E	10 Apr 1994	Geodetic (168 days)
Phase F	28 Sep 1994	Geodetic (168 days) 8 km shifted orbit
Phase G	20 Mar 1995	Multi-Disciplinary (35-days)

Table 3.2. ERS-1 Orbital Phases

In this study, six ERS-1/2 SAR tandem mission data pairs acquired in 1996 are used (Table 3.3). The three-day, repeat-pass ERS-1 SAR data are unavailable for the study region. Several 35-day, repeat-pass data are available; however, the temporal decorrelation was too significant to use these data for repeat-pass interferometry. For the six tandem interferograms of this study, the perpendicular baseline at the scene center $B_{\perp}$ varies from about 6 to 195 m. The coherence is estimated within a 5×5 moving window in a 3×15 multilooked interferogram, and the mean coherence value for each interferogram ranges from 0.40 to 0.66 (Table 3.3). Figure 3.5 shows six coherence images for interferogram pairs listed in Table 3.3. The highest coherence is found with the shortest baseline in the image pair of 24918 of ERS-1 and 5245 of ERS-2. The longer

Track	Orbits (ERS-1/-2)	Acquisition Dates	$B_{\perp}$, m	Mean Coherence
381	23916/4243	10/11 Feb 1996	-152.1	0.41
	24417/4744	16/17 Mar 1996	-147.4	0.40
	24918/5245	20/21 Apr 1996	-5.8	0.66
424	23959/4286	13/14 Feb 1996	-120.8	0.50
	24460/4787	19/20 Mar 1996	-194.9	0.40
	24961/5288	23/24 Apr 1996	-22.9	0.62

Table 3.3. ERS-1/2 tandem mission data used in this study.

the baseline is, the worse the coherence is found. This is so because the change of the look angle may cause different backscattering characteristics over the snow/ice cover area. In a coherence image the top of a peninsula at the lower left corner of the image shows low coherence relative to the surrounding area. It is presumably due to the accumulation or elimination of snow on the surface by wind blowing.

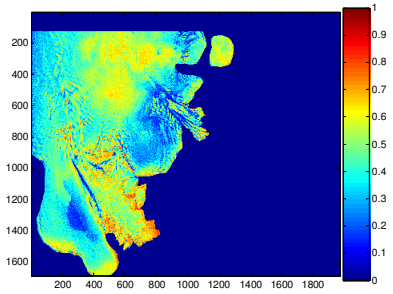

(a) 23916/4243

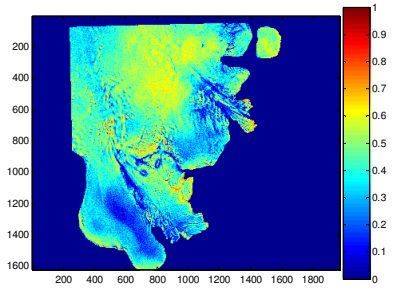

(b) 24417/4744

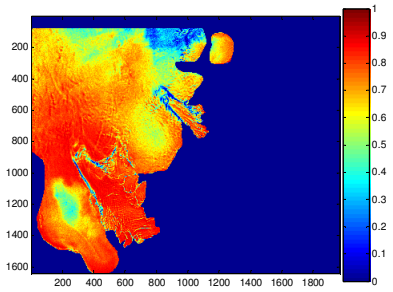

(c) 24918/5245

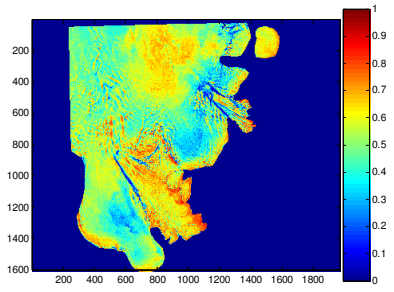

(d) 23959/4286

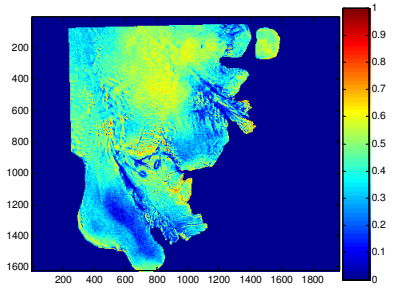

(e) 24460/4787

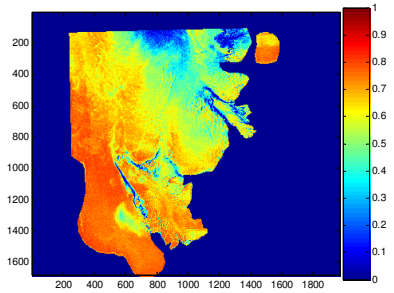

(f) 24961/5288

Figure 3.5. Coherence images corresponding to image pairs in Table 3.3 from top to bottom.

3.3.2 ICESat Data

On January 12, 2003, NASA launched the first Earth observing satellite laser altimetry mission, ICESat. ICESat is the first polar orbiting satellite mission to carry a laser altimeter, and it continues to provide surface elevation of the earth surfaces with unprecedented accuracy and resolution [Schutz et al., 2005]. ICESat's laser footprint is about 70 m in diameter. Its along-track spacing of 172 m (see Table 3.4) provides much denser and more accurate elevation data than traditional radar altimetry, and ICESat works well over all surface types with moderate slopes. The vertical accuracy of ICESat laser altimetry over the ice sheet is projected to be approximately ±5 cm rms, and the horizontal footprint accuracy is within ± 10 m [Zwally and Shuman, 2002]. Initial studies have shown that ICESat elevation data are accurate within ± 10 cm [Braun et al., 2004; Magruder et al., 2003]. It aims to determine the annual and long-term changes in ice-sheet volume (and inferred mass change) in Antarctica and Greenland to a sufficient level of accuracy to assess their impact on global sea level change [Zwally et al., 2002]. The position of the footprint of the laser on the earth's surface is determined by the sum of two vectors, laser position and range. The position is expressed as geodetic latitude, longitude, and height with respect to a reference ellipsoid. GLAS, GPS, and a star tracking camera are the key instruments to put this measurement concept into practice: GLAS measures the distance between the laser instrument and the earth's surface, GPS the satellite position in space, and the star tracking camera and several gyros provide the satellite orientation as well as the pointing angle of the laser to the ground. GLAS has three laser phases (namely Laser 1, 2, and 3), but operates one laser at a time (see Table 3.5). Using the GLAS measurement over East Antarctica, the root mean square error was

Parameters	Value
Altitude, km	600
Inclination, deg	94
Repeat cycle, days	91
Coverage	86°N to 86°S
Wavelength, nm	1064
Laser pulse rate, Hz	40
Laser pulse pointing accuracy, arcsec (±)	~2
Foot print diameter, m	70
Along-track resolution, m	172
Cross-track resolution, km	15 (Equator) 2.5 (80° Lat)

Table 3.4. GLAS/ICESat parameters.

Laser operating Phase	Date	Orbit period, days
1	20 Feb, 2003 – 29 Mar, 2003	8
2a	25 Sep, 2003 – 18 Nov, 2003	91
2b	19 Feb, 2004 – 21 Mar, 2004	91
2c	18 May, 2004 – 21 Jul, 2004	91
3a	3 Oct, 2004 – 8 Nov, 2004	91
3b	17 Feb, 2005 – 24 Mar, 2005	91
3c	20 May, 2005 – 23 Jul, 2005	91
3d	21 Oct, 2005 – 24 Nov, 2005	91

Table 3.5. GLAS laser operation phase.

Name	Description
GLA01	GLAS/ICESat L1A Global Altimetry Data
GLA02	GLAS/ICESat L1A Global Atmosphere Data
GLA03	GLAS/ICESat L1A Global Engineering Data
GLA04	GLAS/ICESat L1A Global Laser Pointing Data
GLA05	GLAS/ICESat L1B Global Waveform-based Range Corrections Data
GLA06	GLAS/ICESat L1B Global Elevation Data
GLA07	GLAS/ICESat L1B Global Backscatter Data
GLA08	GLAS/ICESat L2 Global Planetary Boundary Layer and Elevated Aerosol Layer Heights
GLA09	GLAS/ICESat L2 Global Cloud Heights for Multi-layer Clouds
GLA10	GLAS/ICESat L2 Global Aerosol Vertical Structure Data
GLA11	GLAS/ICESat L2 Global Thin Cloud/Aerosol Optical Depths Data
GLA12	GLAS/ICESat L2 Antarctic and Greenland Ice Sheet Altimetry Data
GLA13	GLAS/ICESat L2 Sea Ice Altimetry Data
GLA14	GLAS/ICESat L2 Global Land Surface Altimetry Data
GLA15	GLAS/ICESat L2 Ocean Altimetry Data

Table 3.6. List of GLAS data products.

reported to be less than ±3 cm [Abshire et al., 2005]. Fifteen ICESat data products, identified as GLA01 to GLA15 in Table 3.6, are generated by the ICESat-Science Investigator-led Processing System (I-SIPS).

In this study, GLA06 (global elevations) and GLA12 (ice sheet elevations), available through the National Snow and Ice Data Center [Zwally et al., 2003] are used. These data products include a total of 19 profiles from the ICESat laser phases 2a, 2b, and 2c.

Laser phase	date	No. of points
2a	Oct 7, 2003	254
	Oct 8, 2003	245
	Oct 15, 2003	76
	Oct 16, 2003	101
	Oct 17, 2003	178
	Oct 23, 2003	108
	Oct 24, 2003	215
	Nov 1, 2003	124
	Nov 2, 2003	200
2b	Feb17, 2004	359
	Feb 18, 2004	161
	Feb 24, 2004	31
	Feb 26, 2004	57
	Mar-12, 2004	248
	Mar-13, 2004	300
2c	May 17, 2004	264
	May 26, 2004	96
	Jun 11, 2004	271
	Jun 19, 2004	89

Table 3.7. GLAS/ ICESat profiles used for this study.

3.4 DEM Generation

The four-pass differential InSAR technique developed in [Joughin et al., 1996], [Kwok and Fahnestock, 1996], and [Fatland and Lingle, 1998] has been adopted in this study. Data processing includes the following steps: image coregistration, differential interferogram generation and phase noise filtering, phase unwrapping, baseline refinement, and phase-to-height transformation. The DEM generation using the differential interferogram has been presented by [Kwok and Fahnestock, 1996]. A brief scheme for the method as applied here follows:

Image ID	Master pair (ERS-1/-2)	Slave pair (ERS-1/-2)	$B_{\perp}^{1} - B_{\perp}^{2}$, m	Phase Error, deg	Height Error, m
1	23916/4243	24918/5245	-146.2	20.67	3.83
2	24417/4744	24918/5245	-141.6	21.16	4.05
3	23959/4286	24961/5288	-143.8	17.74	3.34
4	24460/4787	24961/5288	-217.8	21.65	2.69

Table 3.8. Differential interferogram pairs

3.4.1 Image Coregistration

The InSAR DEM generation is based on the processing of at least two complex SAR images covering the same area and acquired from slightly different points of view. Two SLC images are acquired by the two spatially separated antennas for repeat-pass satellite data. Because an interferogram represents the phase difference between two SLC images at the same location, in repeat-pass InSAR processing, a pair of SLC images not covering exactly the same area is needed to be registered. Registration offsets are modeled as bilinear functions in range and azimuth. The cross-correlation coregistration method [Zebker et al., 1994a] is applied between two real-valued intensity images. Co-registration offsets are estimated by locating the peak of the cross-correlation between small subsets of image pairs. This procedure is repeated throughout the image to determine the offsets as functions of azimuth and range coordinates. One image is then resampled to be co-registered with respect to the other image, based on the offset functions. Two four-parameter polynomials are used to model the range, and azimuth offsets and the transformation is described as:

$$\begin{aligned} x' &= a_0 + a_1 x + a_2 y + a_3 xy \\ y' &= b_0 + b_1 x + b_2 y + b_3 xy \end{aligned} \tag{3.1}$$

where (x, y) and (x', y') are the first and second image position, respectively.

3.4.2 Interferogram Generation

The interferometric phase values are calculated by subtracting the phase of one image from the other. This is done by multiplying one SLC with the complex conjugate of the other. The interferometric phase at this stage is composed of phase contributions from surface topography, surface deformation, distance between satellites, atmospheric delay, and noise. In addition, the phase computed from the interferogram is only modulo 2π.

3.4.3 Removal of Phase Ramps and Noise

Phase ramps are computed from range differences between satellites and the reference surface such as the earth ellipsoid model defined by WGS84. The phase ramp is subtracted from the original interferometric phase which yields the so-called 'flattened' interferogram which makes phase unwrapping easier by reducing the number of fringes. To reduce the phase noise in the interferogram, multilooking in 3 by 15 (3 in range direction and 15 in azimuth direction) and phase noise filtering are performed. Figure 3.6

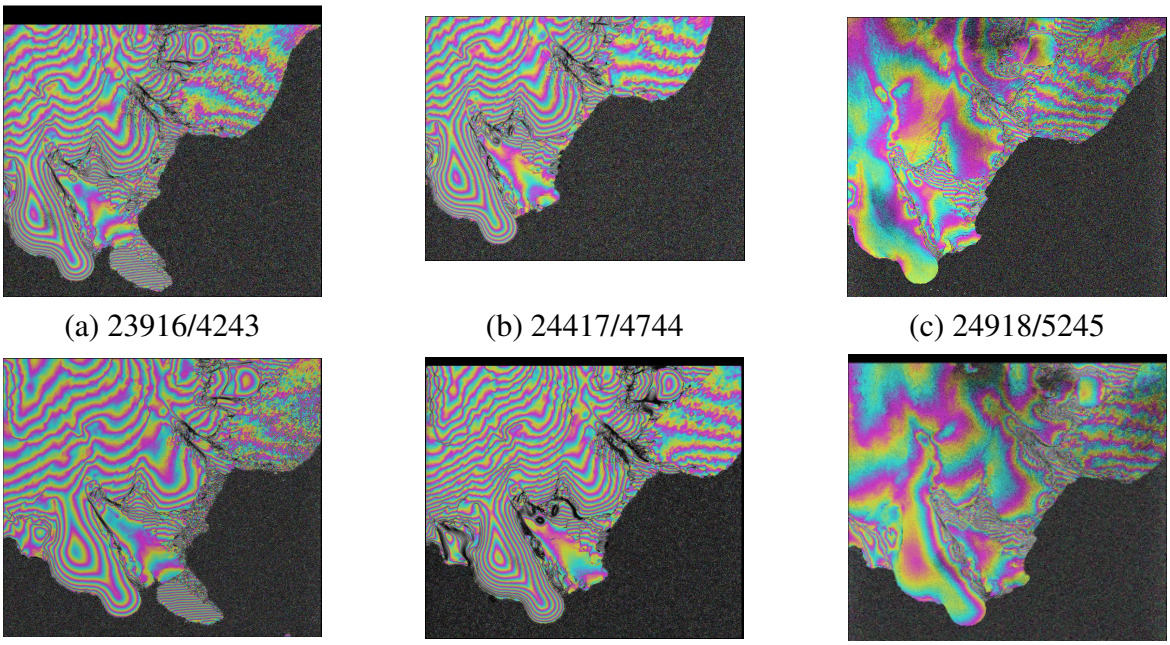

(a) 23916/4243 (b) 24417/4744 (c) 24918/5245

(d) 23959/4286 (e) 24460/4787 (f)24961/5288

Figure 3.6. Flattened and noise-filtered interferograms used for DEM generation.

shows flattened and noise-filtered interferograms for six image pairs for InSAR DEM generation. In this figure, the color represents the interferometric phase, with one cycle of color equal to a phase change of 2π radians in the line of sight in a round trip, i.e., 1 color cycle equals 2.8 cm for ERS. Over the grounded ice, the number of fringes is different from each other according to the perpendicular baseline length (see equation (2.22)). For example, Figure 3.6(c) and (f) show a lower number of fringes than others, due to their short baseline.

3.4.4 Phase-unwrapping

To estimate surface elevation from the interferometric phase, the modulo 2π ambiguity of the phase needs to be resolved by unwrapping the phase. For this step the branch-cut method [Goldstein et al., 1988] is applied in this dissertation. The principle of the branch-cut algorithm is to restrict the integration through the image to paths with local phase differences in the interval $(-\pi, \pi]$. Summing the finite phase differences about the short circular paths permits localization of discontinuities in the filing of the wrapped phase. If the sum is non-zero, a so-called 'residue' lies in the region. The residue value or 'charge' can be positive or negative depending on the sign of the sum. Line segments so-called 'branches', are drawn between positive and negative residues in a systematic way to function as barriers during the path integration that cannot be crossed. This discharge of residues results in a consistent, path-independent solution.

3.4.5 Baseline estimation

Ephemeris baseline data provided by ESA are not accurate enough for DEM generation, and GCPs are required to refine the baseline [Zebker et al., 1994a]. Baseline length and orientation vary along the flight line, or along-track, due to the convergence of ERS orbits. Over the length of an ERS-1 or -2 frame, the baseline is modeled as a linear function of the along-track coordinate, x. The normal component of the baseline can then be represented as

$$B_{\perp}(x) = B_{\perp}^{c} + \delta B_{\perp}\left(\frac{x - x_c}{L_x}\right) \tag{3.2}$$

where $B_{\perp}^{c}$ is the normal component of the baseline at the frame center, x_c, and $\delta B_{\perp}$ is the convergence rate explained as the change in $B_{\perp}$ over the length of the frame, L_x. Similarly the parallel component of the baseline can be modeled as

$$B_{\parallel}(x) = B_{\parallel}^{c} + \delta B_{\parallel}\left(\frac{x - x_c}{L_x}\right) \tag{3.3}$$

The baseline estimation equation suggested by Joughin [1995] was used and solved for the five unknown parameters $B_{\perp}^{c}, B_{\parallel}^{c}, \delta B_{\perp}, \phi_c$, and G_x by least-squares solution:

$$\phi_{unwrap} - \frac{kB^2}{R} + \frac{k\Delta R^2}{R} = -2k\left(\left(B_{\perp}^{c} + \delta B_{\perp}\left(\frac{x - x_c}{L_x}\right)\right)\sin\theta_d + B_{\parallel}^{c}\cos\theta_d\right) - G_x(x - x_c)\cos\theta_d - \phi_c \tag{3.4}$$

where B, ΔR are given values by reference orbit information, e.g., the Delft precise orbit for ERS-1/2 in this dissertation, corresponding to baseline length and the range difference, respectively. ϕ_c is the unknown constant after phase unwrapping, k is the wave number ($=2\pi/\lambda$), θ_d is the look angle difference between the GCPs and the center of the frame. G_x is the azimuth phase ramp, interpreted as a slope from the parallel component of the baseline at two different points along-track and defined by [Joughin, 1995]:

$$G_x = \frac{4\pi}{\lambda}\left(\frac{B_{\parallel}(x_2) - B_{\parallel}(x_1)}{x_2 - x_1}\right) \tag{3.5}$$

For the InSAR DEM generation, a reference DEM or ground surveying data are needed to extract GCP information. However, like many areas in Antarctica, the study area does not have a DEM accurate enough or with adequate resolution to provide GCP or ground surveying data comparable to those from a leveling or GPS campaign. To overcome the lack of GCP data, the GLAS/ICESat laser altimetry is adopted. The accuracy of the ICESat map is more than 10 times better than the accuracy from previous satellite surveys, due to the very narrow footprint of the laser altimeter instrument compared to the much broader footprint (several kms) of radar instruments flown before. The improved mapping of the height of the ice sheet is rather advantageous in studies that use InSAR over remote places like Antarctica. ICESat's along-track spacing of 172 m provides much denser and more accurate elevation data than traditional radar altimetry, and ICESat works well over all surface types with moderate slopes [Schutz et al., 2005].

Assuming that the surface deformation and atmospheric artifacts are negligible, the range and the look angle for each pixel in the interferogram are calculated by using the unwrapped phase and refined baseline [Rufino et al., 1998]. The range difference with respect to the refined baseline allows determination of the height difference between arbitrary target points. The DEM derived from the SAR inteferometry technique is geocoded into a map coordinate. Four differential interferograms are obtained by double differencing of the tandem interferograms (Figure 3.7). Next, the floating ice shelves and the ocean area including the grounding zone from the combined interferogram are masked out to first generate a land-only DEM. For the phase unwrapping, the branch-cut algorithm of [Goldstein et al., 1988] is built into the GAMMA InSAR software of [Werner et al., 2000] which is used here as such. The baseline is modeled as varying linearly along-track using only orbital vectors described in equations (3.2) and (3.3). Next, to refine the baseline, GCPs with known elevations in the image are used to solve equation (3.4) [Zebker et al., 1994a]. In this

study, four ICESat profiles obtained during the same season (February–March 2004) as the SAR data acquisition time are selected to replace the GCPs and are listed in Table 3.11. The baseline components, azimuth convergence rate, and constant phase are estimated using a least-squares adjustment. Cross-track azimuth convergence rates in the four differential interferogram pairs corresponding to the image pairs 1–4 in Table 3.8 are 0.11, 0.08, 0.04, and 0.12 m/s, respectively. The corresponding baseline length changes in the cross-track before and after the baseline refinements are 1.02, 0.21, 0.22, and 0.19 m. Table 3.8 also shows the perpendicular baseline and estimated phase and height errors for the four generated differential interferograms. Based on the refined baselines, a DEM for each differential interferogram pair is generated. For the four differential interferograms, the averaged phase error from the Cramer–Rao bound defined in equation (2.29) ranges from 17.74 to 21.65 with the independent number of looks of 24 [Zebker et al., 1994a]. The independent number of looks is computed based on ERS azimuth and range resolution, pixel size, and averaging pixel sizes. The ERS azimuth resolution is 6 meters and the ground range resolution is 25 meters whereas the pixel sizes are 4 meters and 20 meters, respectively [Zebker et al., 1994a]. Therefore an image that was averaged 3 by 15 will have (see Table 3.1 and equation (2.27))

$$L = \frac{(4\times 15)\times(20\times 3)}{(6\times 25)} = 24 \tag{3.6}$$

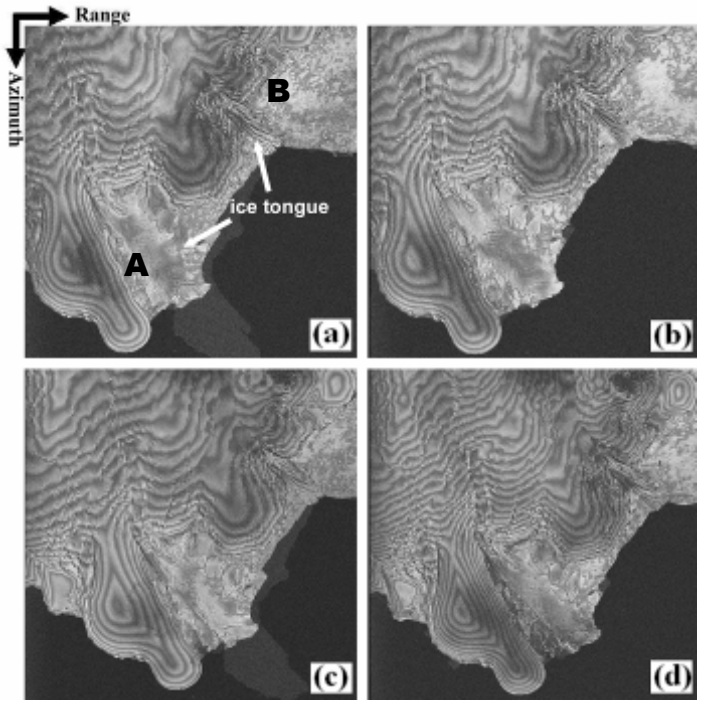

Figure 3.7. (a)–(d) Differential interferograms from image ID 1–4 of Table 3.8.

The resulting averaged height error [Li and Goldstein, 1990] falls between 2.69 and 4.05 m. It should be noted that these values indicate the lower bound of the phase and height errors.

Four InSAR DEMs are generated out of six tandem pairs [Figure 3.7(a)–(d) and Table 3.8] and are averaged considering correlation between DEMs by taking coherence value of each interferogram as weighting factor to first generate a land-only DEM. To generate the DEM over the floating ice shelf, the land-only DEM is combined with the four ICESat profiles passing over the two major ice tongues (approximately 32 km×32 km and 20 km×20 km) using Kriging.

To estimate the ice surface topography from ICESat profiles, one needs to apply an interpolation or extrapolation method. Kriging is one of the possible geostatistical methods. The advantages of using Kriging include that it provides interpolation together with a prediction error. Figure 3.8 shows a block diagram for the procedure of Kriging.

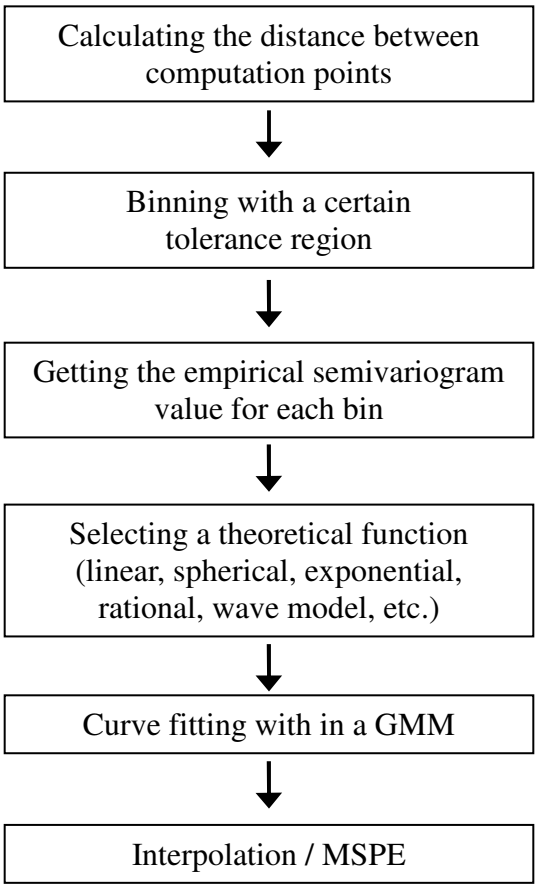

Figure 3.8. Block diagram for Kriging

Computing the empirical semivariogram is the first step for this method. The semivariogram, $\hat{\gamma}(h_k)$, is defined as half of the normalized sum of squared height differences, for all possible pairwise lags between points plotted as a function of their distance h_k:

$$\hat{\gamma}(h_k) = \frac{1}{2 \mid N(h_k) \mid} \sum_{N(h_k)} (z(s_p) - z(s_q))^2 \tag{3.7}$$

where h_k is defined as

$$h_k = \| s_p - s_q \| = \sqrt{(x_p - x_q)^2 + (y_p - y_q)^2} \tag{3.8}$$

$N(h_k)$ is the set of pairs of data at points s_p and s_q, and $|N(h_k)|$ is the number of pairs at the distance h_k. After estimating the empirical semivariogram values, the next step is to fit a theoretical model to them such as a spherical, exponential, or wave model. Figure 3.9 shows several types of theoretical semivariogram models.

A Gauss Markov Model (GMM) is used to fit the chosen theoretical model with the appropriate empirical values using observation. Once the semivariogram is selected, then the interpolator $\tilde{\tilde{x}}(s)$ and its mean square prediction error (MSPE) are obtained according to the primal system for Ordinary Kriging, for instance:

$$\Gamma = \begin{bmatrix} \gamma_x(0) & \gamma_x(s_2 - s_1) & \cdots & \gamma_x(s_n - s_1) \\ \gamma_x(s_2 - s_1) & & & \gamma_x(s_n - s_2) \\ \vdots & & & \vdots \\ \gamma_x(s_n - s_1) & \cdots & \cdots & \gamma_x(0) \end{bmatrix} - \sigma_e^2 I_n \tag{3.9}$$

$$\begin{bmatrix} \Gamma & \tau \\ \tau^T & 0 \end{bmatrix} \begin{bmatrix} \bar{\bar{\chi}}(s) \\ \bar{\bar{\nu}}(s) \end{bmatrix} = \begin{bmatrix} \gamma(s) \\ 1 \end{bmatrix} \tag{3.10}$$

$$\tilde{\tilde{x}}(s) = \bar{\bar{\chi}}(s)^T y \tag{3.11}$$

$$MSPE\{\tilde{\tilde{x}}(s)\} = \bar{\bar{\chi}}(s)^T \gamma(s) + \bar{\bar{\nu}}(s) \tag{3.12}$$

To find the best fitting theoretical semivariogram, two theoretical functions are introduced; the linear and power models for ice tongue A, and the power and exponential models for ice tongue B, respectively. Equations for the models together with the empirical semivariograms are shown in Figures 3.10 and 3.11 for the ice tongues A and B, respectively.

For the linear model with the initial values of (0, 0.0057) for (c_0 , b_l) and a GMM estimate of (6.2906, 0.0058), the height and its mean squared prediction error are obtained by equations (3.11) and (3.12). The mean values of predicted height and the MSPE are -18.6m and 26.2m, respectively, for ice tongue A. For the power model with the initial values of (0, 0.0003, 1.3000) for (c_0, b_p, α) and the GMM estimate of (12.1641, 0.0003, 1.3000), similar values are obtained (see Table 3.9). Between these two models, the power model is selected to predict the heights over ice tongue A, due to its smaller MSPE compared with the linear model.

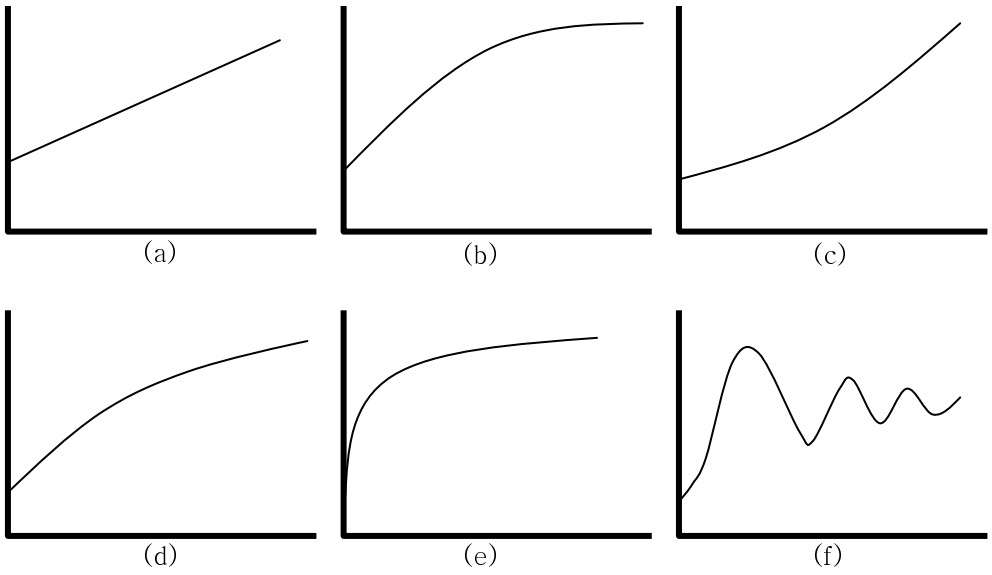

Figure 3.9. Theoretical semivariogram functions [Cressie, 1993]: (a) Linear (b) Spherical (c) Power (d) Exponential (e) Rational quadratic (f) Wave model

	Mean estimate, m	Minimum estimate, m	Maximum estimate, m	Mean MSPE, m
Linear Model	-18.6	-36.1	-0.1	26.2
Power Model	-18.5	-32.1	-1.3	21.7

Table 3.9. Statistics for ice tongue A with a linear and power model estimate.

	Mean estimate, m	Minimum estimate, m	Maximum estimate, m	Mean MSPE, m
Power Model	-14.4	-29.3	-3.3	106.3
Exponential Model	-16.5	-30.6	-1.9	114.9

Table 3.10. Statistics for ice tongue B with a power and exponential model estimate.

For ice tongue B, the power and exponential models are used to fit the empirical values; the statistics are given in Table 3.10. The MSPE is big because only one ICESat profile with a small number of points (105 points) is available over this ice tongue which makes the prediction system unstable. The initial and GMM estimate values for the exponential model are (0, 150, 3000) and (0, 152.5476, 3170.4086), respectively. The power model is selected to get height interpolation over the ice tongue B as well.

(a) Linear Model	(b) Power Model
$\gamma = \begin{cases} 0 & (h=0) \\ c_0 + b_l h & (h \neq 0) \end{cases}$	$\gamma = \begin{cases} 0 & (h=0) \\ c_0 + b_p h^{\alpha} & (h \neq 0) \end{cases}$
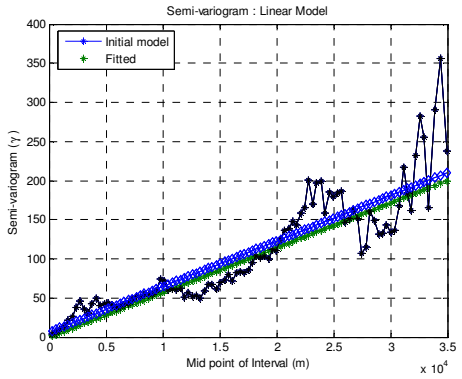	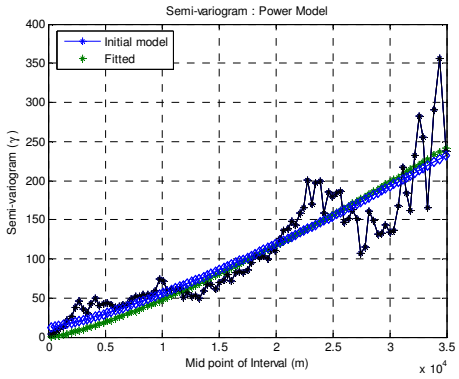

Figure 3.10. Theoretical and fitted models for ice tongue A

The generation of such a DEM bordering the grounding zone is critical in the study of grounding line migration, tidal dynamics, and ice stream velocities. Despite the rapidly changing atmosphere conditions of Antarctica, due to the lack of meteorological data over the region the (differenced) effects of (wet and dry) tropospheric and ionospheric delays for the radar signal are ignored. However, given that Antarctica is relatively dry, one can expect that the localized wet tropospheric delay differences would

(a) Power Model	(b) Exponential Model
$\gamma = \begin{cases} 0 & (h=0) \\ c_0 + b_p h^{\alpha} & (h \neq 0) \end{cases}$	$\gamma = \begin{cases} 0 & (h=0) \\ c_0 + c_e \left[1 - e^{-h/a_e}\right] & (h \neq 0) \end{cases}$
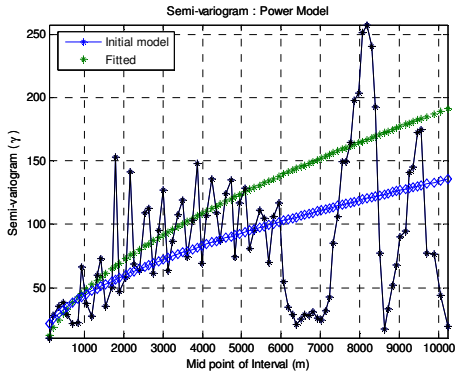	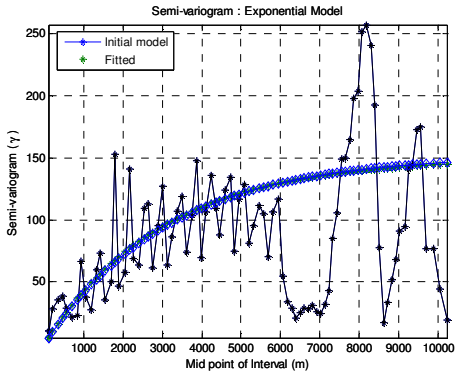

Figure 3.11. Theoretical and fitted models for ice tongue B.

be minimal. The averaging of four DEMs would further reduce such atmospheric delay errors in the radar signal. Azimuth streaks [Gray et al., 2000] have not been observed in our images, which suggests that there are no severe ionospheric disturbances on the SAR data acquisition times.

Profile ID	ICESat Profile	Length, km	Mean±Standard deviations, m
A	17 Feb 2004	62.3	2.93±3.57
B	18 Feb 2004	30.2	2.33±4.26
C	12 Mar 2004	56.6	-0.23±4.55
D	13 Mar 2004	54.4	-2.26±5.50

Table 3.11. Four ICESat profiles used to replace GCPs and their height differences to the InSAR DEM.

Error Source	Changes (8 years)	Reference
Ice melt/flow, Snow accumulation	-6 to -50 cm	[Wingham et al, 1998]
Radar penetration	> ~10 m	[Hoen and Zebker, 2000], [Rignot et al., 2001]

Table 3.12. Error sources.

3.5 Validation of the DEM

In addition to the four ICESat profiles used to replace GCPs in InSAR processing, here 15 independent profiles help to assess the accuracy of the resulting InSAR DEM. Table 3.11 shows the four ICESat GCP profiles and their comparisons with the InSAR DEM. The average difference between all 15 ICESat profiles and the InSAR DEM is -0.55 ± 5.46 m.

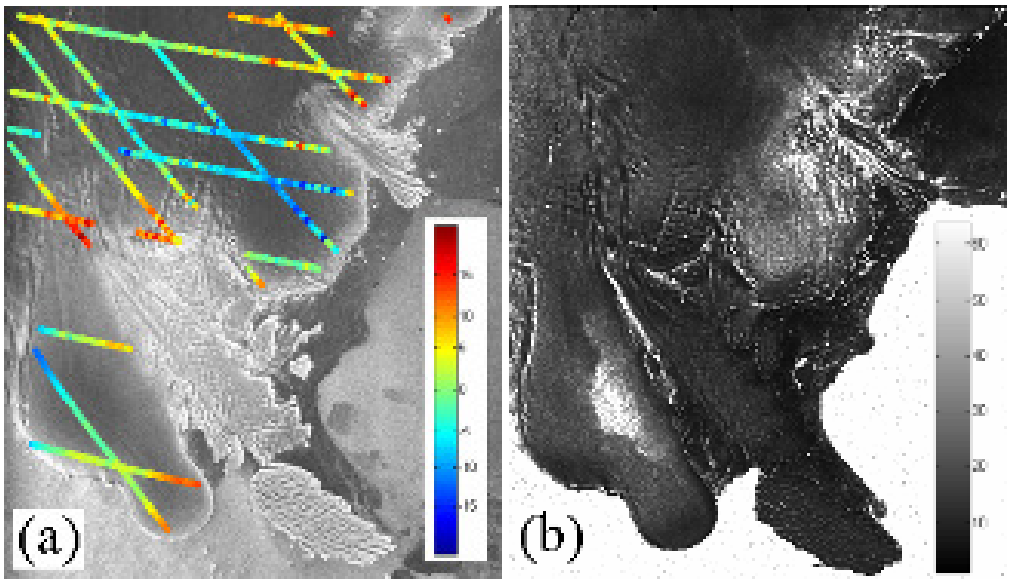

Figure 3.12. (a) The elevation difference, ICESat–InSAR in meters, draped on a SAR amplitude image before adjustment in image coordinates. (b) Phase error in degree in the interferogram between ERS-1 orbit 23916 and ERS-2 orbit 4243.

The differences can be attributed to a number of factors as listed in Table 3.12. In addition to the previously mentioned assumption that the atmospheric delay anomalies are negligible in differential InSAR processing, other physical processes and error sources exist when combining 1996 SAR data and 2004 ICESat laser altimetry data to derive a DEM. First, the processes include surface changes or ice dynamics such as ice melting, snow accumulation, and ice flow. In [Wingham et al., 1998] it was reported that the average elevation change in the Sulzberger Ice Shelf drainage basin had a rate of -3.3 ± 2.6 cm/year between 1992 and 1996. If this rate persists to the present day, the cumulative elevation change over eight years (1996–2004) could be in the range of -6 to -50 cm. Second, laser altimetry measures the surface of snow/ice, while radar (SAR) penetrates into the snow/ice cover. The depth of radar penetration depends on the wetness and compactness of the ice/snow cover, and it can reach a few tens of meters in C-band radar [Hoen et al., 2000; Rignot et al., 2001]. In addition to the above-mentioned error sources, other relatively smaller effects, which include deformations due to glacial isostatic adjustment, solid Earth tides, and atmosphere loading, have a combined magnitude of only several centimeters or less. In summary, despite all these potential error sources, in part resulting from eight years of measurement acquisition time differences, the overall difference of -0.55 ± 5.46 m between ICESat profiles and InSAR DEM indicates an excellent agreement.

However, Figure 3.12(a) shows relatively large localized errors in some areas of the DEM. The actual surface change between SAR and ICESat data acquisitions, radar penetration, and depth variation are the most likely sources of the phase error for this area. In Figure 3.12(b), the cape in the lower left corner of the image shows higher phase errors (brightly colored) than other areas; this implies that there may be significant variation in backscattering characteristics in the area, supporting the possibility of spatial variation in the depth of radar penetration. The baseline refinement through GCPs serves to eliminate the overall (systematic) error trend in the image. To eliminate the local errors that remain even after the baseline refinement, further adjustment is applied.

For the adjustment, the InSAR DEM is selectively compared with the same-season ICESat elevation profiles and is adjusted by constraining the differences. First, ICESat data from February–March and May–June 2004 (phases 2b and 2c, respectively,) are used as reference data to derive difference profiles with respect to the DEM. These differenced profiles are gridded to derive a difference surface model using a bicubic spline. This surface model is applied to the DEM in order to adjust it to the ICESat profiles of phases 2b and 2c. Then, the differences between ICESat data from September–November 2003 (phase 2a) and the adjusted DEM are computed. For this same-season adjustment, the differences between adjusted DEM and ICESat data of phase 2b/c and 2a are -0.01 ± 1.17 m and -0.09 ± 3.44 m, respectively (Table 3.13, fourth column). The opposite-season adjustment is then performed. ICESat phase 2a data are used as reference profiles to compute an opposite-season adjusted DEM. The differences between this DEM and ICESat profiles from phase 2b/c are computed. Here, the differences are -0.07 ± 1.15m and -0.05 ± 3.21m for 2a and 2b/c, respectively (Table 3.13, third column). As expected, in both cases, the surface adjustment leads to significantly smaller mean differences and standard deviations for both phases 2b/c and 2a with respect to the original DEM (Table 3.13, second column). These comparisons reveal localized residual elevation discrepancies between the InSAR DEM and the ICESat altimetry profiles. While the origin of these offsets is speculated to be partially due to varying radar penetration, all the ICESat data are used to create an InSAR/altimetry composite DEM by removing these localized elevation discrepancies using a bicubic spline. As a result, the

Validation Profiles	Before Adjustment, m	DEM differences after constraining validation ICESat profiles, m		
		2a	2b/c	All
2a	0.11±6.14	-0.07±1.15	-0.09±3.44	-0.14±1.25
2b/c	-1.13±5.48	-0.05±3.21	-0.01±1.17	0.02±1.26
All	-0.57±5.88	-	-	0.05±1.35

Table 3.13. Validation of ICESat profiles with the InSAR DEM, before and after adjustment of the DEM to selected ICESat profiles using bicubic spline.

difference between ICESat elevations and the adjusted (composite) DEM is 0.05 ± 1.35m (Table 3.13, fifth column).

Figure 3.13 shows the resulting DEM including the grounded ice and the two floating ice shelves, and the ICESat tracks of phases 2a, 2b, and 2c with the RAMP mosaic image [Jezek, 2002] in the background. The final DEM is compared to ICESat profiles and RAMP DEM in the Figure 3.14, and Figure 3.15 represents the height differences between the original and the composite DEMs and all 19 ICESat profiles available in the study region. For the display purpose a 50 m offset is subtracted intentionally from the InSAR height in Figure 3.14.

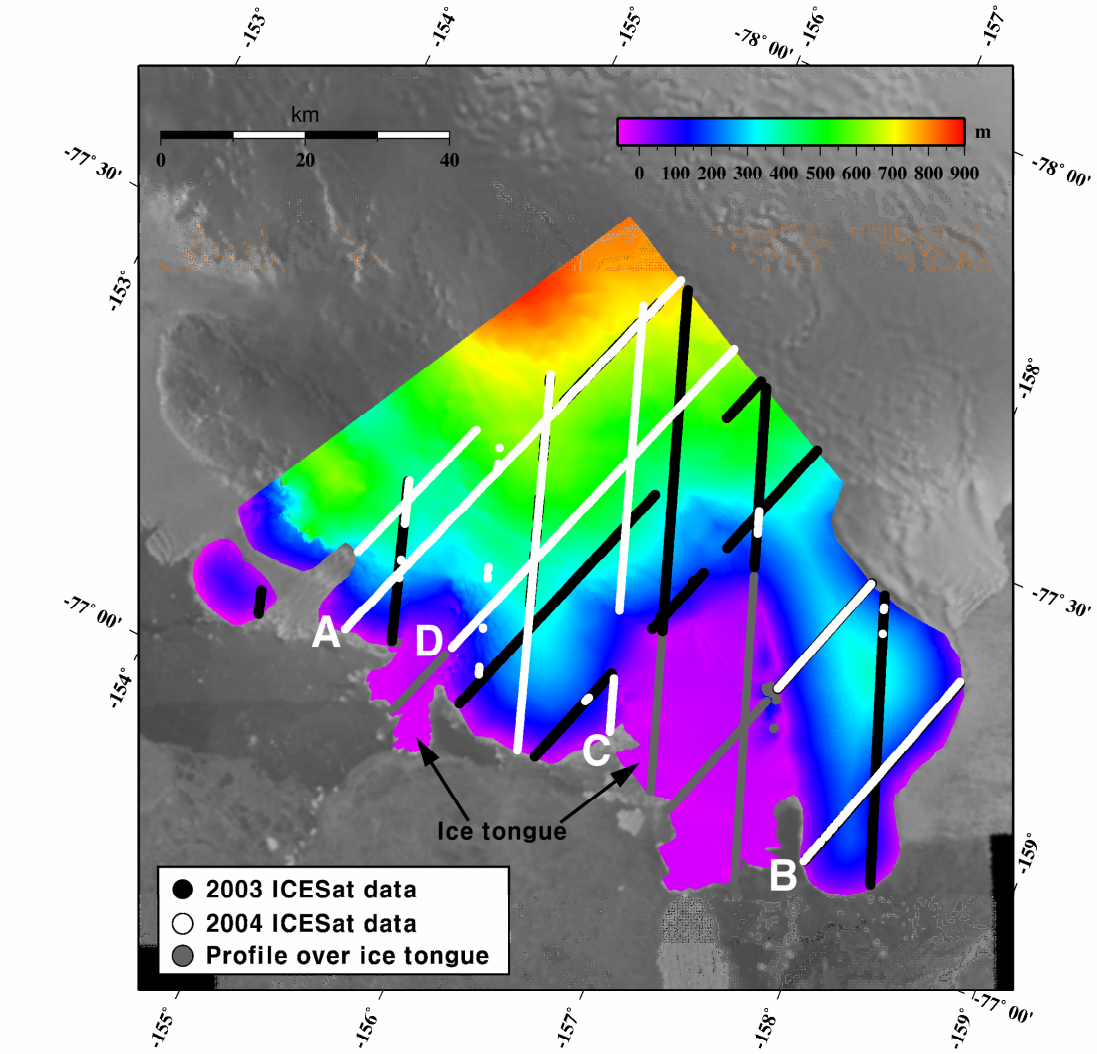

Figure 3.13. Adjusted InSAR DEM and ICESat tracks draped on the Radarsat mosaic image in gray. ICESat profiles from 2003 (phase 2a) are in black and profiles from 2004 (phase 2b/c) are in white. Profiles over the ice tongues are indicated in gray. The four ICESat GCP profiles in white are indicated by A-D.

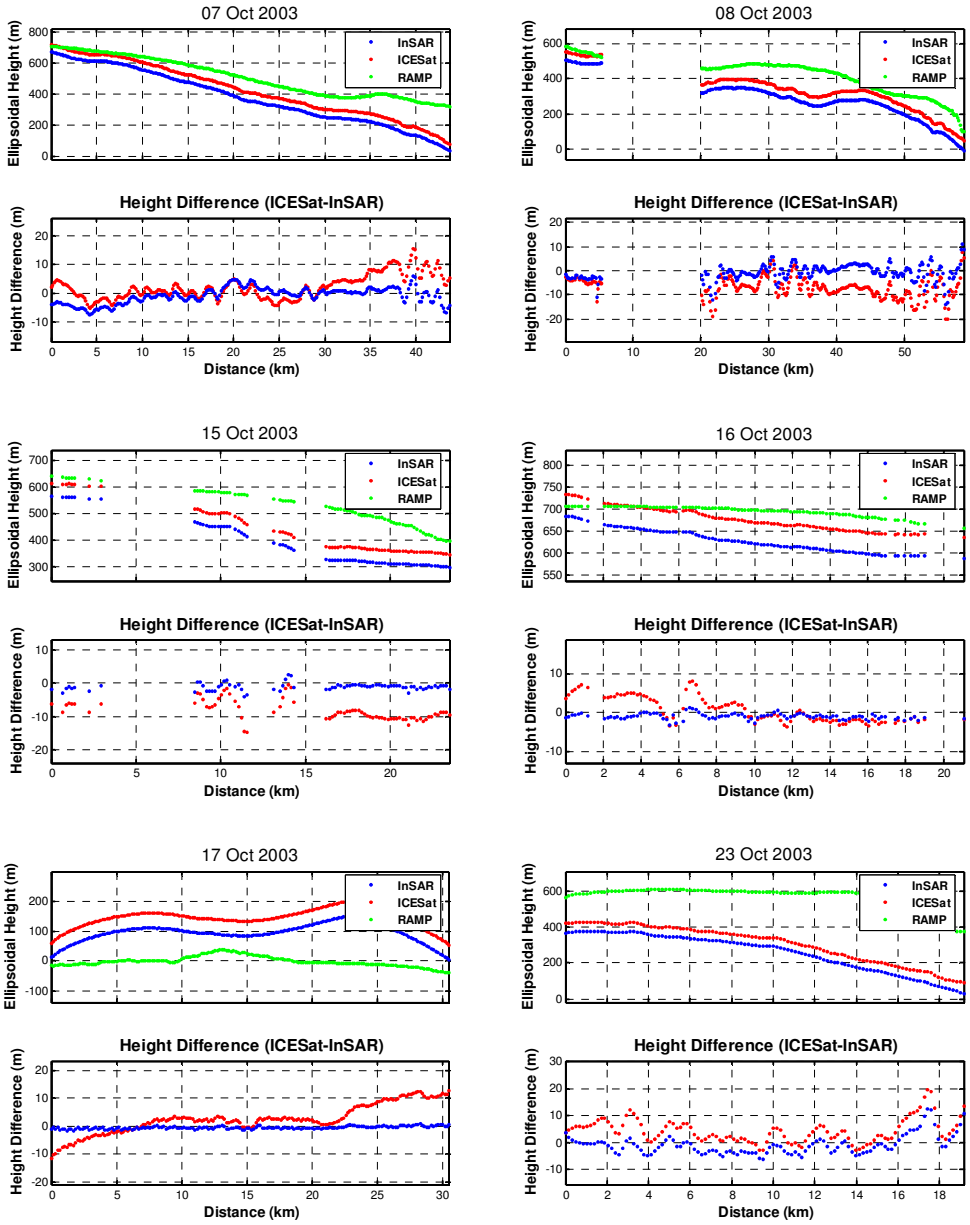

Continued

Figure 3.14. The elevation comparison among ICESat, adjusted InSAR DEM and RAMP DEM profiles.

Figure 3.14 continued

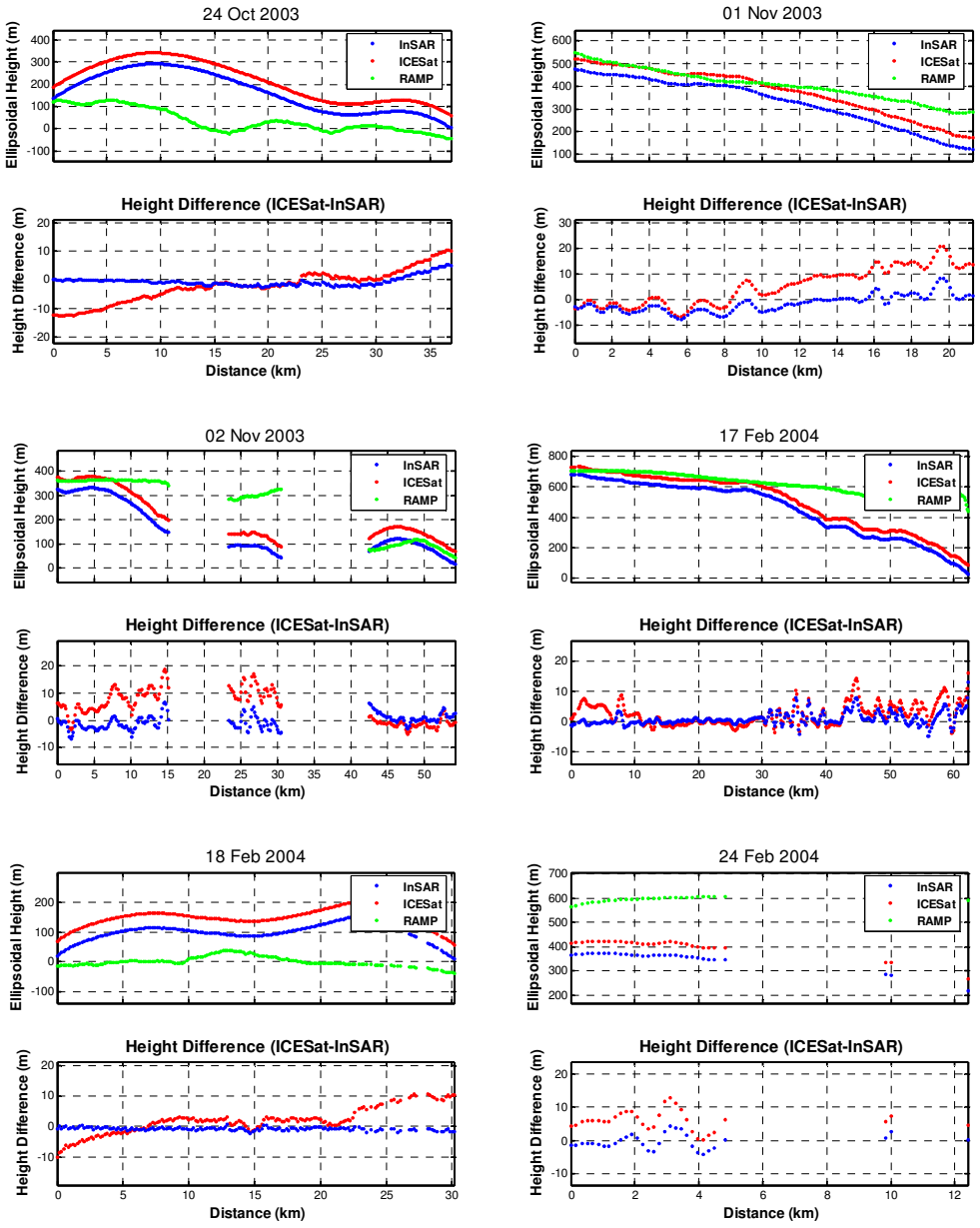

Continued

Figure 3.14 continued

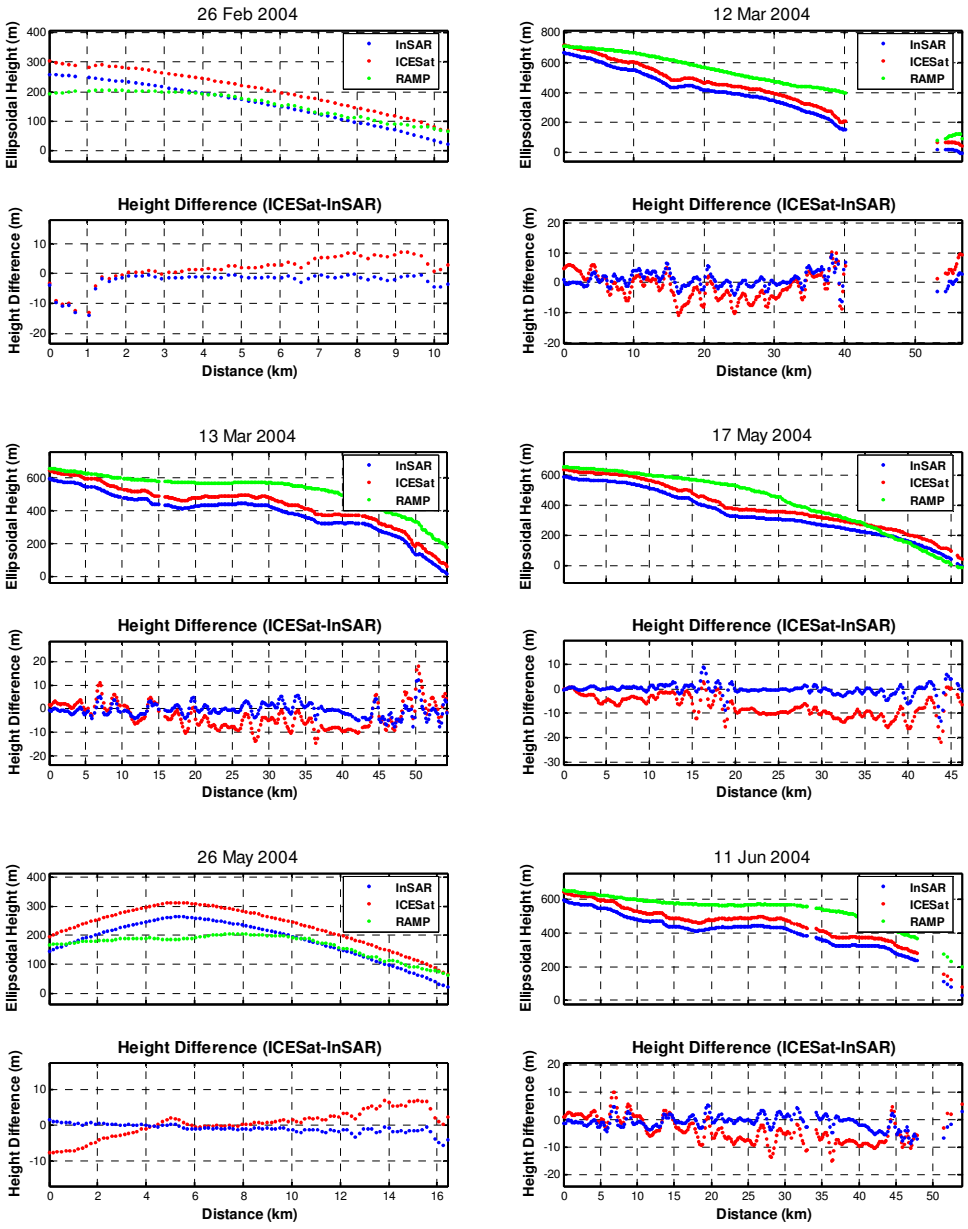

Continued

Figure 3.14 continued

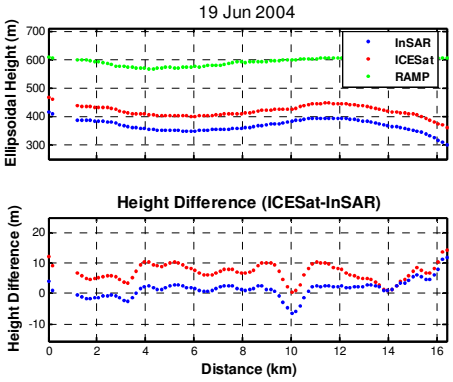

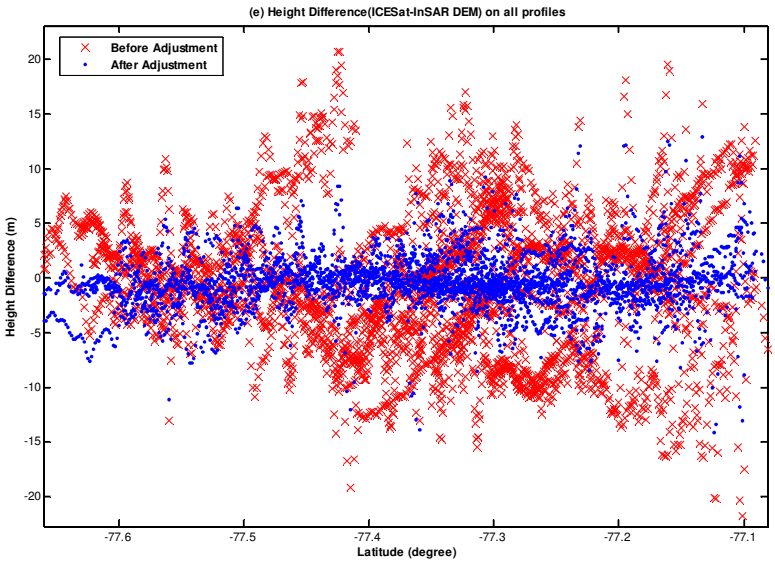

Figure 3.15. The height difference between ICESat profiles and InSAR DEM before and after adjustment over all 19 profiles.

3.6 Conclusions

In this chapter, a high-resolution (60-m) DEM by the Sulzberger Bay, West Antarctica, is generated using differential SAR interferometry over grounded ice and a Kriging method on floating ice shelves. Satellite laser altimeter data from ICESat are used to replace GCPs in generating the InSAR-based DEM. The height differences at the crossover points of ICESat could give some sense of vertical and also horizontal accuracy of the ICESat. There were 13 crossover points over the grounded ice area (see Table 3.14) with the mean difference and standard deviation being -0.85 m and ±1.70 m, respectively. The maximum difference was 2.61 m and the minimum difference was - 4.77 m. Unlike over the ocean surface, over the ground with slope the height difference at the crossover points implies both vertical and horizontal accuracy. Even though the statistics are not as good as predicted, the results is still show a good enough quality for use as ground control points in this study. So, it can be concluded that the orbit information used was reliable, and also the ICESat profiles can be used to replace GCPs for baseline refinment purposes.

It is also concluded that the differential InSAR technique incorporated with ICESat laser altimeter data is a cost-effective method for generating DEMs in remote areas like Antarctica and for cases where GCPs are unavailable. The derived DEM can be used for ice surface deformation studies, tidal dynamics, ice shelf grounding line detection, and the estimation of the grounding zone topography. It is shown that InSAR and ICESat data are complementary data that form the basis for the generation of relatively accurate (several meters) and high-resolution (60-m) DEMs in Antarctica.

Profile 1	Profile 2	Difference, m
7 Oct 03	2 Nov 03	-1.92
7 Oct 03	17 Feb 04	-0.2
7 Oct 03	13 Mar 04	0.03
17 Oct 03	24 Oct 03	0.18
24 Oct 03	31 Oct 03	-0.26
24 Oct 03	18 Feb 04	0.44
31 Oct 03	25 Feb 04	2.45
1 Nov 03	2 Nov 03	2.61
1 Nov 03	13 Mar 04	0.05
2 Nov 03	12 Mar 04	-4.77
17 Feb 04	12 Mar 04	-1.15
24 Feb 04	25 Feb 04	0.44
12 Mar 04	13 Mar 04	1.67

Table 3.14. ICESat height differences at crossover points

CHAPTER 4

TIDAL SIGNAL RECONSTRUCTION USING INSAR

4.1 Introduction

Ocean tides is one of the major effects causing deformations of the floating ice shelves in Antarctica [Fricker and Padman, 2002], and ocean tide modeling which would allow to the accurate removal of tides from space and in-situ measurements is critical for geophysical or glaciological studies including ice sheet mass balance. However, because of the lack of bathymetry data with sufficient accuracy and adequate resolution and of in-situ measurements underneath the ice shelves and in the Antarctic ocean, tide modeling (prediction and assimilations) under the Antarctic ice shelves has been difficult [Fricker and Padman, 2002; King et al., 2005]. InSAR has been used to demonstrate its potential to detect vertical deformation caused by ocean tides underneath the floating ice shelves [Goldstein et al., 1993; Hartl et al.; 1994, Rignot, 1996; Rignot et al. 2000; Padman et al., 2003b].

In this chapter, it will be shown for the first time, that it is possible to estimate selected ocean tidal constituents using InSAR measurements. In the study area, there is an ice tongue (about 30 km by 30 km) floating over the ocean whose vertical motion is significantly affected by ocean tides. Even though the study area is under the coverage of ERS altimeter measurements, these measurements are less accurate (i.e., the ice mode data have lower resolution and accuracy, e.g., over the Filchner-Ronne Ice Shelf [Fricker and Padman, 2002]). Thus sufficiently accurate heights for empirical ocean tide modeling could not be provided. In particular, the resolution of the ice mode data is defined by footprints larger than 5 km, and the precision of the retracked ice elevation heights is only at the meter level. While traditionally tide gauges measure ocean tides adequately, sampled temporally but with limited spatial locations, InSAR can provide observations towards constructing a tidal model with a very dense spatial resolution (tens of meters).

The phase information in an interferogram consists of topography and deformation signals (equation (2.23)). The deformation consists of horizontal and vertical components. To assess the vertical deformation from an interferogram, first, an InSAR DEM is generated, as described in the previous chapter, but by averaging two DEMs and with corrected topography signals. For the rapidly moving ice shelves, vertical deformation should be computed only after the horizontal deformation correction has been applied either through creep flow estimation [Joughin et al., 1996; Zhao, 2001; Gray et al., 2001] or a double differencing technique [Rignot et al., 2000]. However, the horizontal deformation in the study area is assumed to be zero. Our dataset looks almost

perpendicular to the flow direction which is not sensitive to the ice flow and, thus, the InSAR image is almost free of any horizontal signals. In addition, our study area shows only slowly moving ice [Rignot and Thomas, 2002; Shum et al., 2004], and our data from the ERS tandem missions are not significantly affected by the horizontal flow, due to the short time span between the ERS-1/2 data acquisition time (i.e., 1 day).

4.2 Ocean tide models

In addition to empirical models, the results of ocean tide modeling can be categorized into two groups: hydrodynamic models and hybrid assimilation models. A hydrodynamic model such as FES94.1 [Le Provost et al., 1994] is a purely hydrodynamic model that provides altimetry- or tide-gauge-independent predictions of the tides. In particular, FES94.1 provides eight major constituents, M_2, S_2, N_2, K_2, $2N_2$, K_1, O_1, and Q_1, whereas the five tidal constituents Mu_2, Nu_2, L_2, T_2, and P_1 are induced by admittance from the eight major constituents.

Since the advent of satellite altimeters such as those on Topex/Poseidon (T/P) and ERS-1/2, these altimeters have played a major role in providing data for assimilation. However, due to the limitation of the coverage by satellite altimeters, hydrodynamic modeling is still very much needed for the polar regions as well as the world's coastal and estuary regions. The accuracy of the hydrodynamic model depends greatly on the accuracy (and resolution) of the bathymetry data, water column thickness (the vertical distance between ice base and seafloor), and boundary conditions such as the location of the grounding line and the coastline [Padman et al., 2003b; King et al. 2005]. The assimilation models solve the hydrodynamic equations which adjusting altimetry and/or tide gauge data. GOT00.2 [Ray, 1999], NAO.99b [Matsumoto et al., 2000], TPXO.6.2 [Egbert and Erofeeva, 2002], FES2004 [Lefevre et al., 2002], and CATS02.01 [Padman et al., 2002] are all among the assimilated hydrodynamic ocean tide models. Among them, only CATS02.01 is a regional model for Antarctica. Table 4.1 summarizes selected ocean tide models in this study, including the model domains, model resolution/grid size, tidal constituents included, and types of data assimilated.

(1) FES2004

FES2004 assimilated 687 T/P crossover data over deep ocean, about 700 coastal tide gauges (T/G) [King et al, 2005]. It provides eight major, 16 minor, and four long period tidal constituents (M_{tm}, MS_{qm}, M_4, $2N_2$).

(2) NAO.99.b

NAO.99.b provides 16 estimates for major tidal constituents, such as M_2, S_2, K_1, O_1, N_2, P_1, K_2, Q_1, M_1, J_1, OO_1, $2N_2$, Mu_2, Nu_2, L_2, and T_2, assimilating about 5 years of 189 T/P cycles into Schwiderski's hydrodynamic model of 1980. For long period tides, Takanezawa's global model, which is a purely hydrodynamic model, was used to provide seven tidal constituents such as M_{tm}, M_f, MS_f, M_m, MS_m, S_{sa}, and S_a.

(3) TPXO.6.2

TPXO.6.2 is an improved model based on the original work done by Egbert et al. [1994]. The recent model uses 324 T/P cycles to provide estimates for eight major tidal constituents and two long period tidal constituents, M_m and M_f.

(4) GOT00.2

GOT00.2 adjusted the FES 94.1 [Le Provost et al., 1994] hydrodynamic model by using 286 10-days T/P cycles and 81 35-day cycles of ERS-1/2 altimetry outside the T/P coverage. In spite of the use of ERS altimetry over the higher latitudes in the model, the values from GOT00.2 still depend on FES94.1 over the areas outside the data coverage of ERS. It provides eight major and 16 minor tidal constituents.

(5) CATS02.01

CATS02.01 assimilated both T/P over the areas north of 66.2° S and 25 tidal gauges along the coastline based into the pure ocean tide model CATS of [Padman and Kottmeier, 2000]. It provides the eight major tidal constituents, M_2, S_2, N_2, K_2, K_1, O_1, P_1, and Q_1, and the two long period tidal constituents, M_m and M_f. It has no admittance, so the minor constituents are not inferred from major tidal constituents. For the use of differenced height measurements between two satellites or two orbits of one satellite, such as the height difference at altimetry crossover points and InSAR processing with long time span, it may cause large measurement errors depending on the period of the minor constituents and the differencing time interval. The model is a modified version of the TPXO series to express the tides in higher resolution around Antarctica with 10 km spacing, and covering the zone from 58°S to 86°S. As a regional model, it enhanced the

Model	Coverage	Resolution (lat × long)	Input	Constituent
GOT00.2	90 ° S – 90 ° N	0.5º × 0.5º	Hydrodynamic+T/P	8 major, 16 minor
NAO.99b	90 ° S – 90 ° N	0.5º × 0.5º	Hydrodynamic + T/P assimilation	16 short period, long period
TPXO.6.2	90 ° S – 90 ° N	0.25º × 0.25º	Hydrodynamic+T/P+ERS+T/G	8 major, M_m, M_f
CATS02.01	58 ° S – 86 ° S	0.08º ×0.25º	Hydrodynamic+T/P+T/G	8 major, M_m, M_f
FES2004	90 ° S – 90 ° N	0.25º × 0.25º	Hydrodynamic+T/P+T/G	8 major, 16 minor, Long period

Table 4.1. Ocean tide models; T/P stands for Topex/Poseidon, and T/G for tide gauges.

Constituents	M2	S2	N2	K2	K1	O1	P1	Q1
Period, days	95	∞	97	183	365	75	365	133

Table 4.2. ERS-2 aliasing period

prediction quality by smaller grid spacing and better accuracy of the grid geometry compared with the above mentioned global models [Padman et al., 2003b]. The CATS02.01 model is known to predict tidal heights quite well around Antarctica [Padman et al., 2003b; King et al., 2005].

Even with the availability of satellite altimeters, ocean tide modeling in the Southern Ocean around Antarctica remains challenging, due primarily to the limitation of the satellite orbit coverage, sea ice/ice shelf coverage of the ocean, and lack of in-situ data, caused by logistical problems involved in installing tide gauges in harsh conditions. In addition, when assimilating ERS altimetry data in high latitude areas, e.g., in case of GOT00.2, the tidal estimates from ERS have aliasing problem (see Table 4.2), due to its longer repeat-pass than the period of dominant tide signals which is less than 24 hours [Fricker and Padman, 2002]. The differences between GOT99.2b, NAO.99b, and CATS02.01 show that they possess about ±5 to ±6 cm RSS (Root Sum of Squares) error over the Southern Ocean (see Figure 4.1 and Table 4.3). Here the RSS is defined as [Wang, 2005]:

$$RSS = \sqrt{\sum_{i=1}^{8} RMS(i)^2} \tag{4.1}$$

where i is the index for eight tidal constituents from each tide model. The RMS deviation is defined between model 1 and model 2, e.g., as

$$RMS = \sqrt{\frac{1}{2N}\sum_{i=1}^{N}\left(\left[C_1(i)-C_2(i)\right]^2+\left[S_1(i)-S_2(i)\right]^2\right)} \tag{4.2}$$

	M_2	S_2	N_2	K_2	K_1	O_1	P_1	Q_1	RSS
CATS_FES	3.23	2.30	0.83	0.96	2.34	1.94	0.86	0.50	5.25
CATS_GOT	1.56	2.38	1.37	0.86	2.26	2.90	0.69	0.73	5.03
GOT_FES	3.78	2.08	1.53	0.60	2.63	3.01	0.91	0.58	6.20

Table 4.3. Comparison of tide models in the Southern Ocean in terms of rms deviations in the unit of ±centimeter [Wang, 2005].

where C_j and S_j are in-phase and quadrature of the tide model j, N is the total number of locations used for its computation.

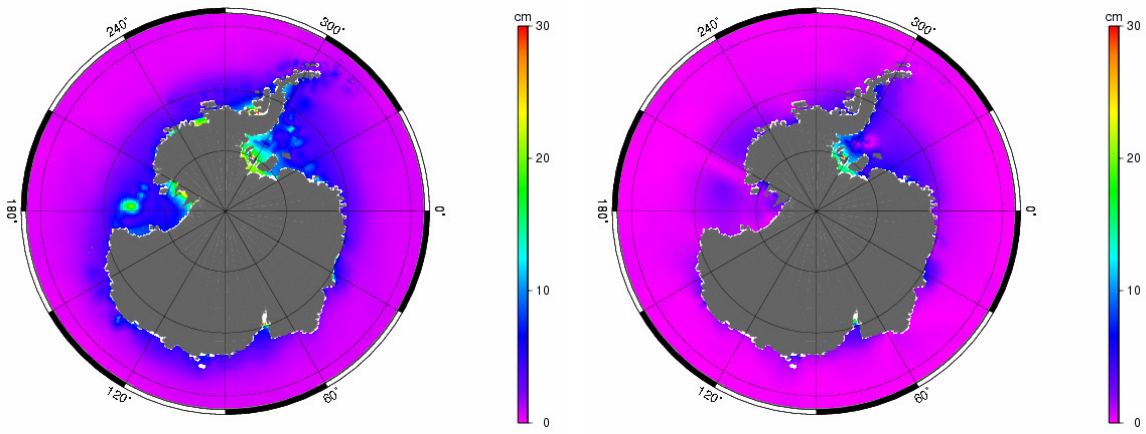

(a) Average RSS tidal difference

(b) Average RMS difference for M_2

(c) Average RMS difference for K_1

(d) Average RMS difference for O_1

Figure 4.1. Tidal height differences between tide models [Wang, 2005].

4.3 Tide model comparison with InSAR observations

The vertical deformation from InSAR observations reflects a certain change of the surface. The deformation of an ice shelf floating over the ocean is affected not only by ocean tide, but also by solid earth tide (SET), ocean loading (OL), atmospheric pressure (or the inverse barometric effect, IB), pole tides, ocean circulation, and snow accumulation or melting. While tide gauges measure pure ocean tidal heights relative to the ocean floor, satellite altimetry and InSAR observe the height of both pure ocean tide and ocean floor loading [Smith, 1999] relative to the earth center of mass. In this study, InSAR derived ocean tides (OT) were computed after correcting for the IB effect, solid earth tides, and ocean loading, i.e., $y_{OT} = (y_{obs} + IB) - SET - OL$ where y_{obs} is the vertical deformation observed by InSAR along the radar line of sight and converted into geocentric change. Pole tide is neglected as it is negligible, especially in the polar regions. The floating ice shelf is affected by atmospheric pressure which is called the IB effect [Padman et al., 2003a], and in this study IB is corrected by using an atmospheric model, provided by the European Centre for Medium-Range Weather Forecasts (ECMWF) [Gibson et al., 1997]. Using the pressure data from ECMWF, the IB effect Δh_{IB} is computed by [Pugh, 1996]:

$$\Delta h_{IB} = -\frac{\Delta P_A}{\rho_w g} \tag{4.3}$$

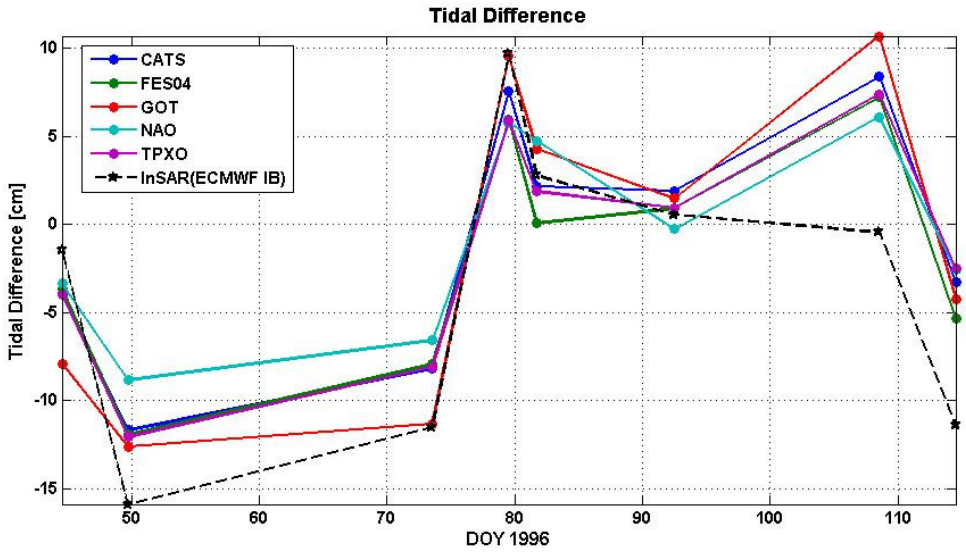

Figure 4.2. Tide model comparison with InSAR observations at the ice tongue edge of the study area.

where ΔP_A are the local pressure variations about the mean atmospheric pressure over the oceans, ρ_w is the sea water density, e.g., 1030 kg/m^3 [Schmeltz et al., 2002], and g is the magnitude of the gravitational acceleration, approximately 9.8 m/s^2. Even though the resolution of the atmospheric model is coarse, the differencing pressure over 1 day shows a good correction to the vertical deformation. This is presumably not due to of the model accuracy, but because of a smooth change of the pressure over this area, beside the elimination of model errors by subtraction of 1 day separation pressures.

While a tide model provides predicted tidal values without involving observations, InSAR provides independent observations and, hence, can be compared to different tide models. Figure 4.2 shows the tidal height differences synthesized from tide models at InSAR observation times over the ice tongue edge of the study area. The correlation coefficient between the InSAR observations and the models is larger than 0.70. Except for TPXO.6.2, the four other models, CATS02.01, FES2004, GOT00, and NAO.99b, have an even higher correlation coefficient (≥0.77) with the InSAR observations. The rms difference varies from ±4.89 to ±5.23 cm. Based on this comparison, it is found that there is no major difference between the models and the InSAR observations. However, [King et al., 2005] pointed out that the good agreement between tide model predictions does not imply tide model accuracy; rather it is because of the similar data input used in the models.

Tidal signals can be extracted by the four-pass differential interferometry techniques, which was introduced in chapter 2.5. Among the data pairs listed in Table 3.3, the first two InSAR pairs from track 381 were selected for tidal difference comparison with selected tide models. Even though track 381 was used for InSAR DEM generation, already, the combination between the two InSAR pairs in this chapter was not a combination used for DEM generation because of the very similar length of baselines, which are -152.1 and -147.4m. As shown in Figure 4.3, due to the ocean tidal difference between successive images, there are dense fringe lines (so-called ‘fringe belts’) along the transition area from land to sea in the differential interferogram, indicating the grounding line. The consistency of the tidal change was checked between tide model and SAR interferogram over the time span for the SAR data acquisition. Four tide models NAO99b, TPXO.6.2, CATS02.01, and GOT00 are used for comparison, and no major differences were found in magnitude and direction of tides corresponding to each SAR data acquisition time. Each predicted tidal difference from the models is shown in Table 4.5.

Models	CATS02.01	FES2004	GOT00.2	NAO.99b	TPXO.6.2
Correlation	0.78	0.80	0.77	0.77	0.72
rms Difference (±cm)	4.89	5.05	5.23	5.01	4.99

Table 4.4. Correlation coefficient and rms difference.

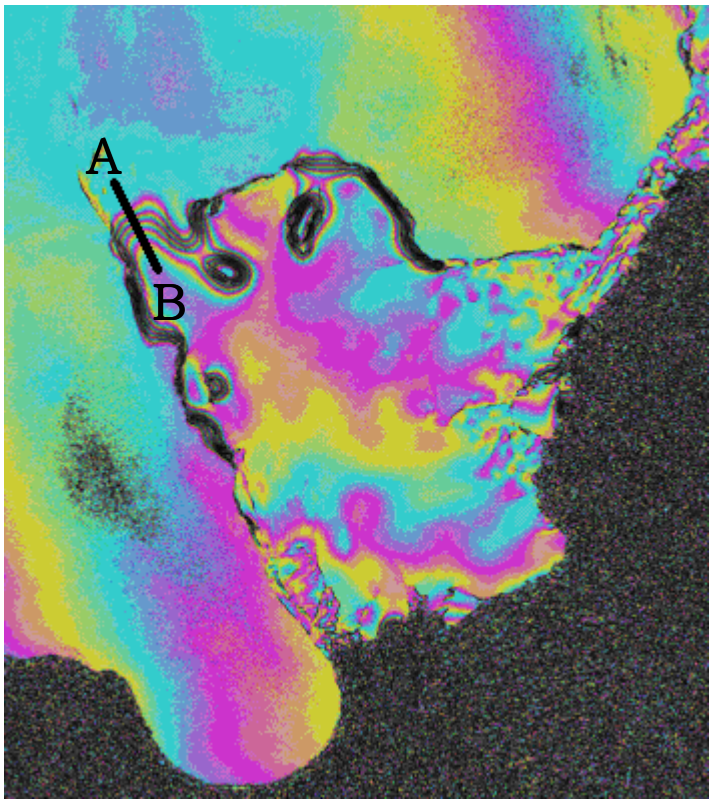

Figure 4.3. Four pass differential interferogram with fringe belt.

The values in the last row of Table 4.5 represent relative tidal changes between the first and last SAR acquisition days, i.e., $(t_1\text{-}t_2)\text{-}(t_3\text{-}t_4)$. According to the SAR image combination, it spans 37 days between the first and the last image. A negative value means that the sea level at day 37 is lower than at day 1. Tidal differences measured by SAR interferometry are obtained by the phase differences between two points A and B across the grounding line in Figure 4.3. Phase values in the unwrapped interferogram are 0.1 rad and 34.7 rad for a grounded point A and a floating point B, correspondingly. This range difference along the SAR line of sight is converted to a geocentric elevation change [Rignot. et al., 2000]. The range difference of 34.6 rad is converted into a vertical displacement of 37.5 rad. This value is for a round trip; so, after dividing by two and multiplying the wavelength by 2π, the geocentric vertical deformation was computed to be -16.7 cm. A positive value in range distance means subsidence of the surface at day 37 relative to day 1. So the magnitude and its direction essentially agree with those predicted from the tide models. Among the four tide models, the CATS02.01 model fits best, but other tide models are still in good agreement with InSAR, showing less than 3 cm differences.

Date	NAO.99b	TPXO.6.2	CATS02.01	GOT00.2
1996-2-10	-15.8	-13.1	-12.3	-7.4
1996-2-11	-21.5	-21.1	-20.1	-15.6
1996-3-16	-9.8	2.9	1.6	-8.6
1996-3-17	-0.8	12.5	10.8	-3.0
4-pass difference	-14.7	-17.5	-16.9	-13.9

Table 4.5. Tidal differences predicted by different models (in cm).

4.4 Tidal characteristics in Sulzberger Bay

Tides around Antarctica show opposite tidal species between the Weddell Sea and the Ross Sea. While semi-diurnal tides M_2 and S_2 are dominant with large tidal amplitudes (>1m) at the Weddell Sea, the diurnal tides O_1 and K_1 are dominant in the Ross sea area [Padman et al, 2002; Fricker and Padman, 2002; Han et al., 2005]. Figures 4.4 and 4.5 show different tidal patterns at two different locations plotted based on the CATS02.01 model values for each tidal constituent.

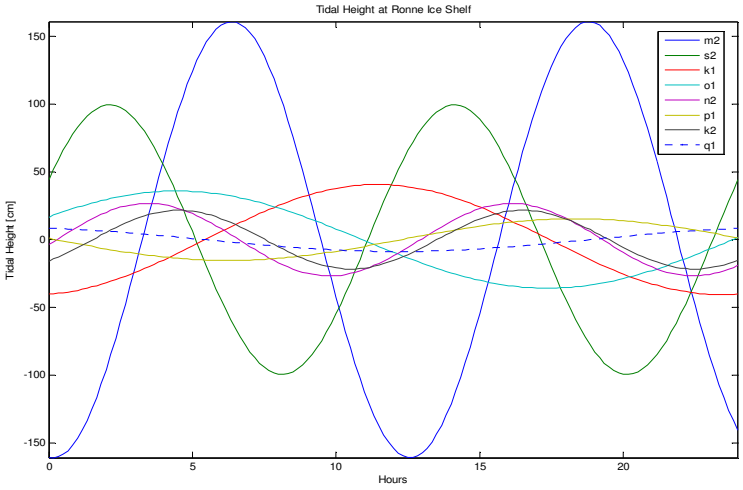

Figure 4.4. Tidal height from the CATS02.01 model over 24 hours at Ronne Ice Shelf (73.0° W, 80.0° S).

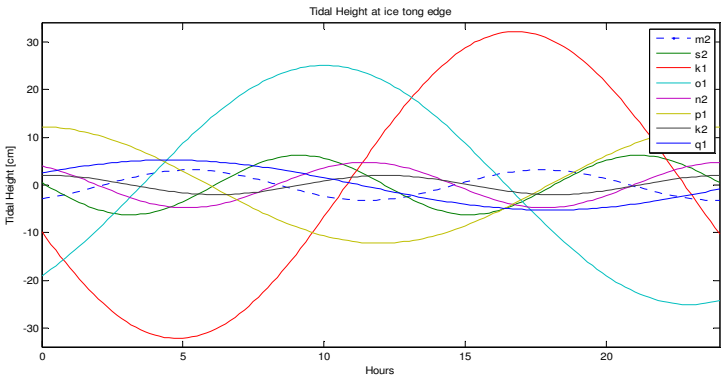

Figure 4.5. Tidal height from the CATS02.01 model over 24 hours at the ice tongue edge of the study area.

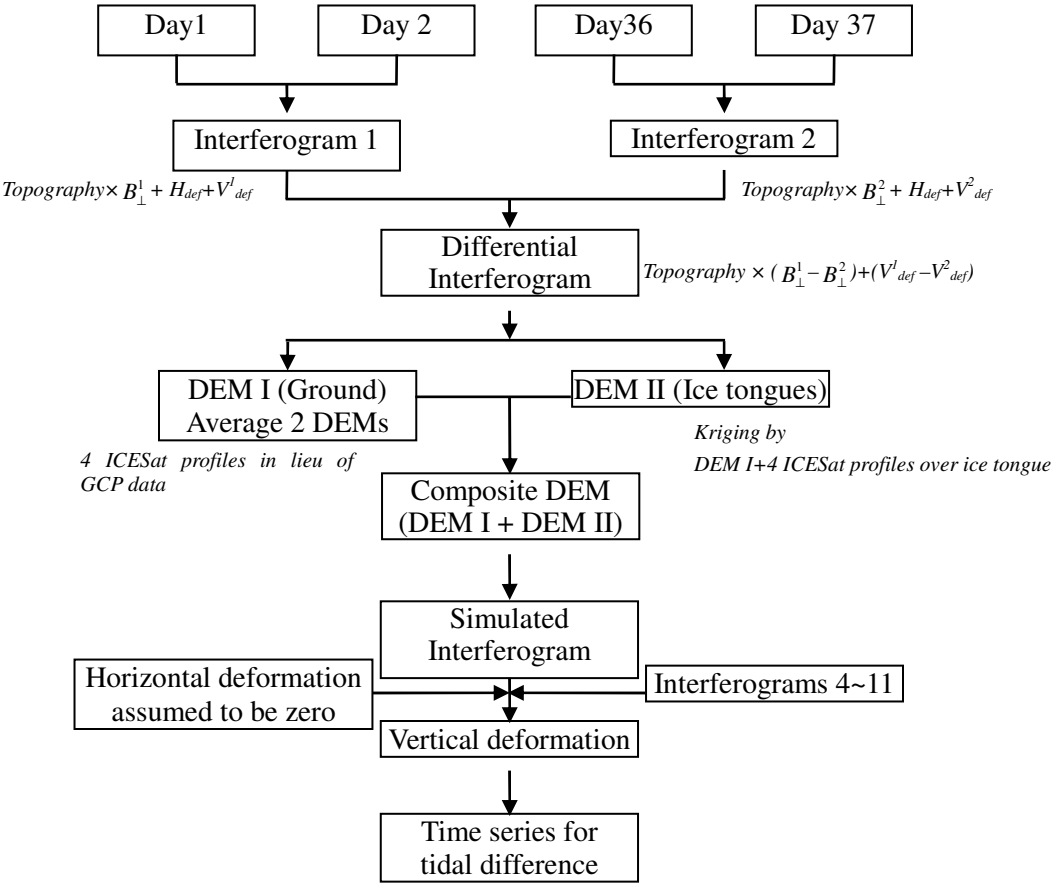

Figure 4.6. Diagram for DEM generation and deformation study ($B_{\perp}$: perpendicular baseline, H_{def}: Horizontal deformation, V_{def} : Vertical deformation).

4.5 InSAR tidal deformation observations

To extract tidal signals from the interferogram, two-pass differential interferometric processing for which it is necessary to have an external DEM is applied. For this requirement, we generate an InSAR DEM through the differential interferometric method while exploiting ICESat profiles in lieu of GCPs over ground ice. Over the floating ice, the elevation is computed by Kriging. Figure 4.6 shows a diagram for the procedure to get the time series for tidal differences using InSAR. Among 11 available InSAR pairs, three interferograms in Table 4.6 are used for InSAR DEM generation over grounded ice and ICESat profiles over floating ice with the method described in the previous chapter. The remaining eight interferograms (Table 4.7) are reserved to extract vertical deformation by subtracting the topography phase using a simulated interferogram by the DEM.

Table 4.6 shows the differential interferogram pairs for InSAR DEM generation along with their perpendicular baseline difference $B_{\perp}^{1} - B_{\perp}^{2}$ and temporal baseline B_T. Figure 4.7 shows a comparison between all 19 ICESat profiles and a new InSAR DEM and their difference. The mean and the standard deviation for this plot are (0.05 ± 8.06) m which is worse than expected, considering the quality of the DEM averaged among four InSAR DEMs in the previous chapter 3.4. Because of the subtraction of an interferogram from another interferogram simulated by a DEM, the vertical deformation from InSAR is affected by both the DEM accuracy and the interferogram accuracy. First, using equation (2.29), we found the phase standard deviation using mean coherence values over the ice tongue. Second, the phase error induced by the DEM standard deviation is computed by the modified version of equation (2.34) such as:

$$(\sigma_{\phi})_{DEM} = \frac{4\pi}{\lambda} \frac{B_{\perp}}{R \sin\theta} \sigma_z \tag{4.4}$$

Image	Master pair	Slave pair	$B_{\perp}^{1} - B_{\perp}^{2}$, m	B_T, days
1	23916/4243	24918/5245	-146.2	35
2	24417/4744	24918/5245	-141.6	70

Table 4.6. Differential interferogram pairs for InSAR DEM generation for tidal studies.

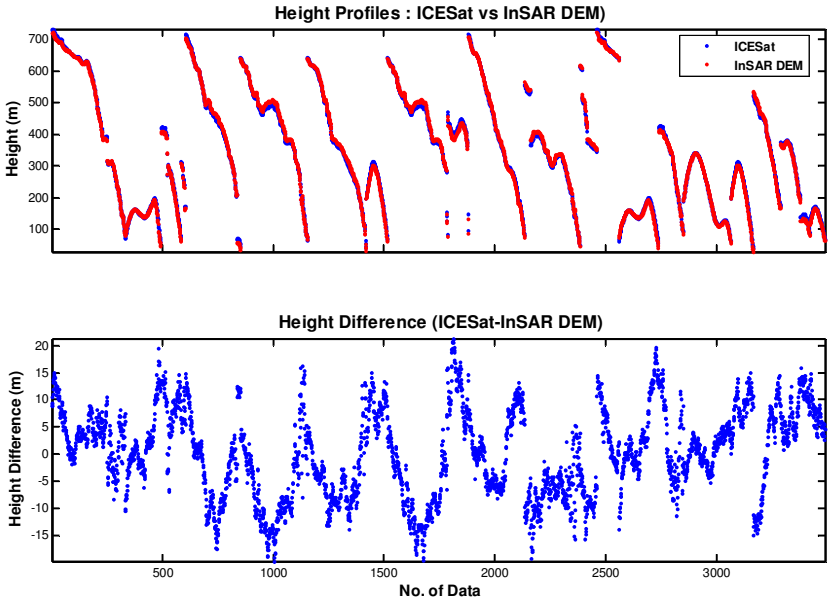

Figure 4.7. ICESat and InSAR DEM profiles.

With an assumption of no correlation between InSAR and DEM, which holds due to independence between interferograms used in the DEM generation and the rest of the interferograms, the combined phase between InSAR and the simulated interferogram using the combined DEM has the standard deviation:

$$(\sigma_\phi)_{def} = \sqrt{(\sigma_\phi)^2_{InSAR} + (\sigma_\phi)^2_{DEM}} \tag{4.5}$$

Again the standard deviation of the geocentric deformation, due to the phase standard deviation is computed by following (2.25) modified:

$$(\sigma_z)_{def} = \frac{\lambda}{4\pi} \frac{(\sigma_\phi)_{def}}{\cos\theta} \tag{4.6}$$

where θ denotes the local incidence angle as in Figure 2.6, which is the angle between look direction and local vertical direction. Here it is assumed that the ice tongue surface is flat enough to approximate the local incidence angle with the radar look angle.

ERS1/2	$B_{\perp}$, m	$\lvert\gamma\rvert$	Date
23959/4286	-121	0.5	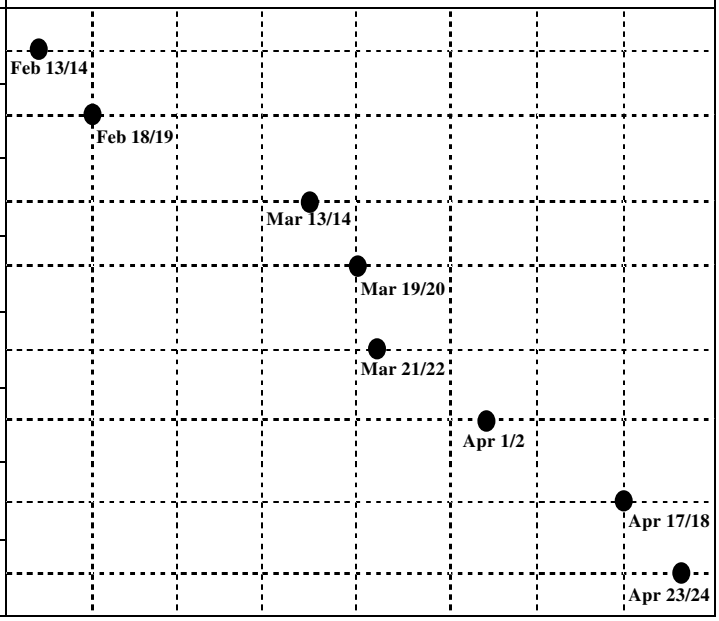
24033/4360	-217	0.4	
24374/4701	-114	0.3	
24460/4787	-195	0.4	
24491/4818	-23	0.5	
24646/4973	18	0.7	
24875/5202	-5	0.3	
24961/5288	-23	0.6	

Table 4.7. InSAR time series from 8 ERS-1/2 tandem pairs ($\lvert\gamma\rvert$ is mean coherence, and $B_{\perp}$ is perpendicular baseline).

Tidal Band	$H_s > 0$	$H_s < 0$
Long Period	π	0
Diurnal	$\pi/2$	$-\pi/2$
Semidiurnal	0	π

Table 4.8. Values of χ_i for the long-period, diurnal, and semi-diurnal period corresponding to the sign of the amplitude H_s at the tidal frequency s, defined by [Cartwright and Tayler, 1970]'s harmonic expansion of the tide-generating potential.

Constituents	Doodson Number	Period, hours
K_1	165.555	23.9345
K_2	275.555	11.9672
M_2	255.555	12.4206
N_2	245.655	12.6583
O_1	145.555	25.8193
P_1	163.555	24.0659
Q_1	135.655	26.8684
S_2	273.555	12.0000

Table 4.9. Doodson number and period for eight major tidal constituents.

4.6 InSAR observation equation

The ocean tidal signal can be expressed as a function of time, t, and location, (ϕ,λ), as follows [McCarthy, 1996; Cartwright and Tayler, 1970]:

$$\zeta(t,\phi,\lambda) = a + b\cdot t + \sum_{i=1}^{n} f_i H_i(\phi,\lambda)\cos(\omega_i t + \Theta_i(t_0) + \chi_i + u_i - G_i(\phi,\lambda)) \quad (4.7)$$

where ω_i is the angular frequency for the tidal constituent i; t is Universal Time measured in mean solar days from a reference epoch t_0 such as January 1, $0^h.000$, 1900; $\Theta_i(t_0)$ is the astronomical argument at t_0; $H_i(\phi,\lambda)$ and $G_i(\phi,\lambda)$ are the amplitude and phase for the tidal constituent i at location (ϕ,λ); χ_i is the additive phase correction as defined in Table 4.8; f_i and u_i are slowly varying functions to account for the longitude of the lunar node.

The astronomical argument $\Theta_i(t_0)$ is computed by multiplying the vector $\overline{n} = [A \quad B \quad \cdots \quad F]$ by the Doodson variables:

$$\Theta_i(t_0) = A\tau + Bs + Ch + Dp + EN' + Fp_1 \quad (4.8)$$

Doodson Argument	Description and relation to the nutation series	Frequency ($^\circ / hr$)	Period
τ	Local mean lunar time (angle)	14.4920521	1.0035050 days
s	Moon's mean longitude	0.5490165	27.321582 days
h	Sun's mean longitude	0.0410686	365.242199 days
p	Mean longitude of moon's perigee	0.0046418	8.847309 yrs
$N'(=-N)$	Negative longitude of moon's ascending node	0.0022064	18.612904 yrs
p_1	Longitude of sun's perigee	0.0000020	20,940.2766 yrs

Table 4.10. Doodson's fundamental angles. Values are from Brown [1919] and Newcomb [1895].

where A through F are integer numbers corresponding to the tidal constituent *i*, which is a result of subtraction [0 -5 -5 -5 -5 -5] from the Doodson number defined in Table 4.9, and the vector $[\tau\ s\ h\ p\ N'\ p_1]$ contains the Doodson variables defined in Table 4.10. A more complete definition of Doodson's arguments are found in Newcomb's theory of the solar elements h and p_1 along with Brown's lunar theory for the arguments s, p, and N as follows [Doodson, 1921; Casotto, 1989]:

	f_i : series of multiples of				u_i : series of multiples of		
	1	$\cos N$	$\cos 2N$	$\cos 3N$	$\sin N$	$\sin 2N$	$\sin 3N$
K_1	1.0060	0.1150	-0.0088	0.0006	-8.86	0.68	-0.07
K_2	1.0241	0.2863	0.0083	-0.0015	-17.74	0.68	-0.04
M_2	1.0004	-0.0373	0.0002	–	-2.14	–	–
O_1	1.0089	0.1871	-0.0147	0.0014	10.80	-1.34	0.19
S_2, P_1, N_2, Q_1	$f_{S_2} = f_{P_1} = 1$ $f_{N_2} = f_{M_2}$ $f_{Q_1} = f_{O_1}$				$u_{S_2} = u_{P_1} = 0$ $u_{N_2} = u_{M_2}$ $u_{Q_1} = u_{O_1}$		

Table 4.11. Values of f_i and u_i with the longitude of moon's ascending node N as defined in equation (4.9). For example, the f_i value for the tidal constituent K_1 is computed by $f_{K_1} = 1.0060 + 0.1150\cos N - 0.0088\cos 2N + 0.0006\cos 3N$.

$$
\begin{aligned}
\tau &= 15^\circ t - s + h \\
s &= 270^\circ.43659 + 481267^\circ.89057T + 0^\circ.00198T^2 + 0^\circ.000002T^3 \\
h &= 279^\circ.69660 + 36000^\circ.76892T + 0^\circ.00030T^2 \\
p &= 334^\circ.32956 + 4069^\circ.03403T - 0^\circ.01032T^2 - 0^\circ.000010T^3 \\
N &= 259^\circ.18328 - 1934^\circ.14201T + 0^\circ.00208T^2 + 0^\circ.000002T^3 \\
p_1 &= 281^\circ.22083 + 1^\circ.71902T + 0^\circ.00045T^2 + 0^\circ.000003T^3
\end{aligned}
\tag{4.9}
$$

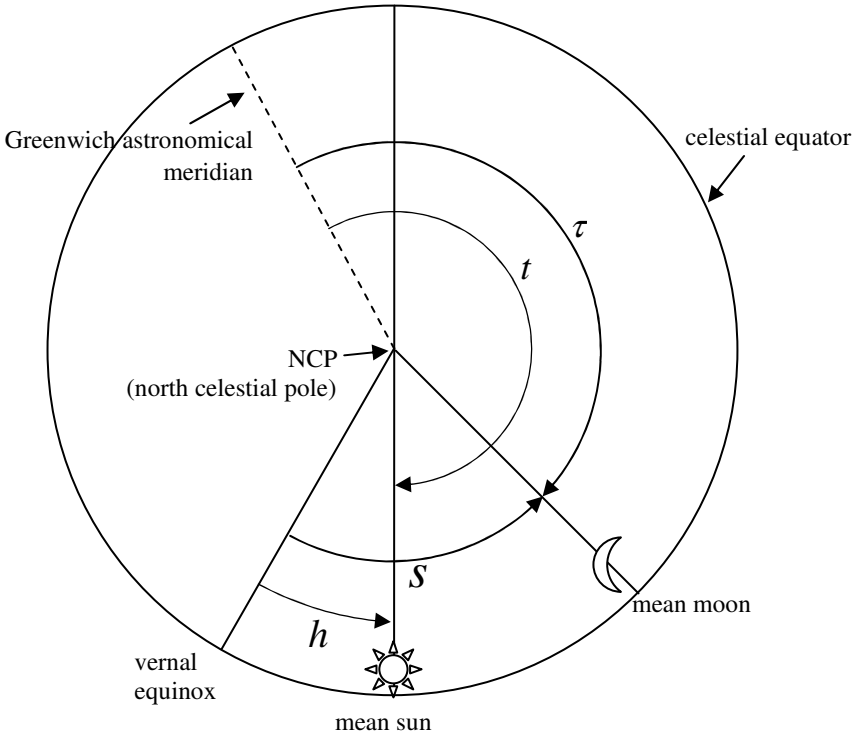

Figure 4.8. Relations between Greenwich mean solar time, t, Greenwich mean lunar time, τ, moon's mean longitude, s, and sun's mean longitude, h [Smith, 1999].

where t is the Greenwich mean solar time, and T is the time defined as the Julian centuries past Julian date of 2415020, corresponding to the Greenwich mean moon on December 31, 1899, 12:00 Universal Time (UT). These values are represented modulo 2π. The two variables f_i and u_i are computed through the relations in Table 4.11 for the eight major tidal constituents [Doodson, 1928].

By setting $\Omega_i = \omega_i t + \Theta_i(t_0) + \chi_i + u_i$ and introducing harmonic coefficients $C_i(\phi,\lambda)$ and $S_i(\phi,\lambda)$, equation (4.7) can be rewritten as follows:

$$\zeta(t,\phi,\lambda) = a + b \cdot t + \sum_{i=1}^{n} [C_i(\phi,\lambda)\cos\Omega_i + S_i(\phi,\lambda)\sin\Omega_i] \tag{4.10}$$

where the harmonic coefficients $C_i(\phi,\lambda)$ and $S_i(\phi,\lambda)$ are defined as:

$$C_i(\phi,\lambda) = f_i H_i(\phi,\lambda)\cos G_i(\phi,\lambda) \tag{4.11.1}$$

$$S_i(\phi,\lambda) = f_i H_i(\phi,\lambda)\sin G_i(\phi,\lambda) \tag{4.11.2}$$

Amplitude and phase are computed by the harmonic coefficients such as:

$$H_i(\phi,\lambda) = \frac{\sqrt{C_i^2(\phi,\lambda) + S_i^2(\phi,\lambda)}}{f_i} \tag{4.12.1}$$

$$G_i(\phi,\lambda) = \arctan\left(\frac{S_i(\phi,\lambda)}{C_i(\phi,\lambda)}\right) \tag{4.12.2}$$

The observation from InSAR, according to Figure 2.6, is the range difference ΔR along the line of sight between times t_1 and t_2 such as $\Delta R = R(t_1,\varphi,\lambda) - R(t_2,\varphi,\lambda)$ and is converted to the surface elevation change to form an observation equation:

$$\begin{aligned} \Delta\zeta(t_1, t_2,\phi,\lambda) &= \zeta(t_1,\phi,\lambda) - \zeta(t_2,\phi,\lambda) \\ &= b(t_1 - t_2) + \sum_{i=1}^{n} [C_i(\phi,\lambda)(\cos\Omega_{i,1} - \cos\Omega_{i,2}) + S_i(\phi,\lambda)(\sin\Omega_{i,1} - \sin\Omega_{i,2})] \end{aligned} \tag{4.13}$$

The time difference $(t_1 - t_2)$ is -24 hours as determined by the ERS orbit configuration; in the ERS tandem mission period, ERS-2 passes almost the same area as previously passed by ERS-1 with 24 hours separation. Because of this special case of the time difference, there is a limitation in the determination of the tidal constituents using

Constituents	K_1	K_2	M_2	N_2	O_1	P_1	Q_1	S_2
correlation	0.09	-0.10	0.16	-0.36	0.79	0.25	0.63	-0.23

Table 4.12. Eight major tidal constituents from the CATS02.01 model and their correlation coefficient with the InSAR observations.

the ERS tandem mission. For example, the period of the S_2 tide is exactly 12 hours (in a solar day) and, thus, the S_2 tidal signal is canceled out by subtracting between two SAR images acquired at a 24 hour difference. Rigorously speaking, however, due to the slight difference between solar and sidereal day, it is not canceled perfectly. With this orbit configuration, several constituents with periods close to 12 and 24 hours, e.g., S_2 as well as K_1 with a period of 23.9345 hours, will be primarily eliminated and are unlikely to be detected by the InSAR measurements.

Unlike satellite altimetry, the InSAR time series has no aliasing problem, due to irregular sampling; the nature of forming an interferogram, however, which is a subtraction between two images at a difference of 24 hours, prohibits InSAR from providing a solution for all tidal constituents. In the Sulzberger Bay, next to the Ross Sea, K_1 and O_1 are also dominant tides. However, due to the aforementioned satellite orbital characteristics, K_1 signal with a frequency very close to 1 day is diminished in the ERS tandem mission interferometry. In contrast to K_1, both O_1 and Q_1 are favorable

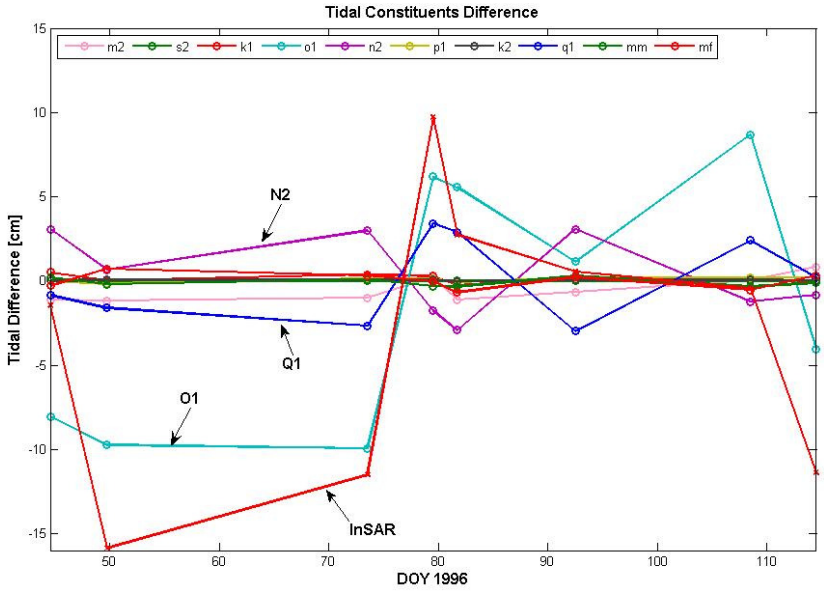

Figure 4.9. Differences of the tidal constituents and the InSAR measurements at the ice tongue edge.

constituents to be detected from the InSAR data of the ERS tandem mission, based on their correlation coefficients with InSAR observations; O_1 has the largest correlation at 0.79, and Q_1 is the next largest at 0.63 (Table 4.12). Because of this reason, among the K_1 and O_1 tides which are dominant in the study area, the K_1 signal is insensitive in the InSAR observations, whereas O_1 and Q_1 are potentially observable tidal constituents, using the data from the ERS tandem mission. Figure 4.9 shows the tidal difference of each constituent, along with the InSAR measurement in the study area.

4.7 Adjustment in a Gauss-Helmert Model

In equation (4.13), the times, (t_1, t_2), the location, (ϕ, λ), and the quantities Ω_i, are assumed to be known, the harmonic coefficients $C_i(\phi, \lambda)$ and $S_i(\phi, \lambda)$ are supposed to be estimable, along with b, within a Gauss-Markov Model:

$$y = A\xi + e, \quad e \sim (0, \sigma_0^2 P^{-1}), \tag{4.14}$$

where y is a n×1 observation equation vector, ξ is a m×1 vector of unknown parameters, A is the n×m design matrix, σ_0^2 is the unknown variance component, and P is a given weight matrix of size n×n. The random error vector e is assumed to have zero mean and the dispersion matrix of $\sigma_0^2 P^{-1}$. The Least-Squares Solution of ξ in model (4.14) is

$$\hat{\xi} = N^{-1}c, \quad [N \quad c] = A^T P[A \quad y] \tag{4.15}$$

provided that A has full column rank.

Any $q_1 < m$ nuisance parameters can be eliminated by finding a $(n - q_1) \times n$ matrix B that satisfies the condition $BA_1 = 0$ with $rank(B) + rank(A_1) = n$ where q_1 is the rank of matrix A_1 with $A = [A_1 \quad A_2]$, and n is the number of observations. Now the transformed model can be written in the form of a Gauss-Helmert Model, or "condition equations with parameters," as follows:

$$By = BA_2\xi_2 + Be, \quad e \sim (0, \sigma_0^2 P^{-1}). \tag{4.16}$$

Letting $w = By$, $\overline{A} = BA_2$, and $\bar{e} = Be$, above equation may be rewritten as

$$w = \overline{A}\,\xi_2 + \bar{e}, \quad \bar{e} \sim (0, \sigma_0^2 BP^{-1}B^T). \tag{4.17}$$

To get the least-squares solution which satisfies $e^T Pe = \min_{e,\xi}\{w - \overline{A}\,\xi - Be = 0\}$, the Lagrange target function is formed as:

$$\Phi(e,\xi,\lambda) := e^T Pe + 2\lambda^T (w - \overline{A}\,\xi - Be) = \underset{e,\ \xi,\ \lambda}{stationary} \tag{4.18}$$

Then the Euler-Lagrange necessary conditions are:

$$\frac{1}{2}\frac{\partial \Phi}{\partial e} = P\tilde{e} - B^T\hat{\lambda} \doteq 0 \tag{4.19.1}$$

$$\frac{1}{2}\frac{\partial \Phi}{\partial \xi} = \overline{A}^T\hat{\lambda} \doteq 0 \tag{4.19.2}$$

$$\frac{1}{2}\frac{\partial \Phi}{\partial \lambda} = w - \overline{A}\,\hat{\xi} - B\tilde{e} \doteq 0 \tag{4.19.3}$$

In the above equations the notation of "$\doteq$" is read as "set to be" and "$:=$" means "equal by definition."

From (4.19.1) and (4.19.3), we have

$$\hat{\lambda} = (BP^{-1}B^T)^{-1}(w - \overline{A}\,\hat{\xi}) \tag{4.20}$$

Substituting (4.20) into (4.19.2), we get the normal equations in the form

$$[\overline{A}^T(BP^{-1}B^T)^{-1}\overline{A}]\hat{\xi} = [\overline{A}^T(BP^{-1}B^T)^{-1}w] \tag{4.21}$$

An equivalent normal equation system in matrix form can be written as

$$\begin{bmatrix} BP^{-1}P & \overline{A} \\ \overline{A}^T & 0 \end{bmatrix}\begin{bmatrix} \hat{\lambda} \\ \hat{\xi} \end{bmatrix} = \begin{bmatrix} w \\ 0 \end{bmatrix} \tag{4.22}$$

by combining (4.20) with (4.19.2).

Obviously by solving equation (4.22), we return to the solutions as above:

$$\hat{\xi} = [\overline{A}^T(BP^{-1}B^T)^{-1}\overline{A}]^{-1}[\overline{A}^T(BP^{-1}B^T)^{-1}w] \tag{4.23.1}$$

$$\hat{\lambda} = (BP^{-1}B^T)^{-1}(w - \overline{A}\,\hat{\xi}) \tag{4.23.2}$$

The dispersion matrix for $\hat{\xi}$ is obtained as:

$$D\{\hat{\xi}\} = \sigma_0^2[\overline{A}^T(BP^{-1}B^T)^{-1}\overline{A}]^{-1}, \tag{4.24}$$

And the residual vector $\tilde{e}$ is found by (4.19.1) and (4.23.2), together with its dispersion matrix, as:

$$\tilde{e} = P^{-1}B^T(BP^{-1}B^T)^{-1}(w - \overline{A}\hat{\xi}) \tag{4.25.1}$$

$$\begin{aligned} D\{\tilde{e}\} = {} & \sigma_0^2 P^{-1}B^T(BP^{-1}B^T)^{-1}BP^{-1} \\ & - \sigma_0^2 P^{-1}B^T(BP^{-1}B^T)^{-1}\overline{A}[\overline{A}^T(BP^{-1}B^T)^{-1}\overline{A}]^{-1}\overline{A}^T(BP^{-1}B^T)^{-1}BP^{-1} \end{aligned} \tag{4.25.2}$$

The covariance between $\hat{\lambda}$ and $\hat{\xi}$ happen to be zero, i.e., $C\{\hat{\lambda},\hat{\xi}\} = 0$, and hence $C\{\tilde{\tilde{e}},\hat{\xi}\} = 0$. The variance component estimate $\hat{\sigma}_0^2$ is computed by properly scaling $\tilde{e}^T P\tilde{e} = \tilde{e}^T B^T(BP^{-1}B^T)^{-1}B\tilde{e} = \hat{\lambda}^T(BP^{-1}B^T)^{-1}\hat{\lambda}$ in order to find:

$$\begin{aligned} \hat{\sigma}_0^2 &= \frac{\tilde{e}^T P\tilde{e}}{r} = \frac{(w - A\hat{\xi})^T\hat{\lambda}}{r} = \frac{w^T\hat{\lambda}}{r} \\ &= \frac{w^T(BP^{-1}B^T)^{-1}w - w^T(BP^{-1}B^T)^{-1}\overline{A}\hat{\xi}}{r} \end{aligned} \tag{4.26}$$

after exploiting (4.20) and (4.19.2) again, where the redundancy r is defined by $r = n - m = (n - q_1) - (m - q_1)$.

In this dissertation, measurements are provided in the form of differenced tidal heights from InSAR to estimate harmonic coefficients of tidal constituents. Equation (4.13) can be expanded in matrix form as follows:

$$E\left\{\begin{bmatrix} \zeta_1 - \zeta_2 \\ \zeta_3 - \zeta_4 \\ \vdots \\ \zeta_{n-1} - \zeta_n \end{bmatrix}\right\} =$$

$$\begin{bmatrix} (t_1 - t_2) & \cos\Omega_{1,1} - \cos\Omega_{1,2} & \sin\Omega_{1,1} - \sin\Omega_{1,2} & \cdots & \cos\Omega_{m,1} - \cos\Omega_{m,2} & \sin\Omega_{m,1} - \sin\Omega_{m,2} \\ (t_3 - t_4) & \cos\Omega_{1,3} - \cos\Omega_{1,4} & \sin\Omega_{1,3} - \sin\Omega_{1,4} & \cdots & \cos\Omega_{m,3} - \cos\Omega_{m,4} & \sin\Omega_{m,3} - \sin\Omega_{m,4} \\ \vdots & \vdots & \vdots & \vdots & \vdots & \vdots \\ (t_{n-1} - t_n) & \cos\Omega_{1,n-1} - \cos\Omega_{1,n} & \sin\Omega_{1,n-1} - \sin\Omega_{1,n} & \cdots & \cos\Omega_{m,n-1} - \cos\Omega_{m,n} & \sin\Omega_{m,n-1} - \sin\Omega_{m,n} \end{bmatrix} \begin{bmatrix} b \\ C_1 \\ S_1 \\ \vdots \\ C_m \\ S_m \end{bmatrix} \tag{4.27}$$

It should be noted that, even though the above equation is different for any two time epochs, the estimates are still for the coefficients for the original harmonic signal. From those estimates of the harmonic coefficient, amplitude and phase estimates can also be obatined such as:

$$\hat{H}_i(\phi,\lambda) = \frac{\sqrt{\hat{C}_i^2(\phi,\lambda) + \hat{S}_i^2(\phi,\lambda)}}{f_i} \tag{4.28.1}$$

$$\hat{G}_i(\phi,\lambda) = \arctan\left(\frac{\hat{S}_i(\phi,\lambda)}{\hat{C}_i(\phi,\lambda)}\right) \tag{4.28.2}$$

The dispersions of amplitude and phase estimates are; by error propagation:

$$D\{\hat{H}_i(\phi,\lambda)\} = \frac{1}{f_i^2}\left[\frac{\hat{C}_i(\phi,\lambda)}{\sqrt{\hat{C}_i^2(\phi,\lambda)+\hat{S}_i^2(\phi,\lambda)}} \quad \frac{\hat{S}_i(\phi,\lambda)}{\sqrt{\hat{C}_i^2(\phi,\lambda)+\hat{S}_i^2(\phi,\lambda)}}\right] D\begin{Bmatrix}\hat{C}_i(\phi,\lambda)\\ \hat{S}_i(\phi,\lambda)\end{Bmatrix}\begin{bmatrix}\frac{\hat{C}_i(\phi,\lambda)}{\sqrt{\hat{C}_i^2(\phi,\lambda)+\hat{S}_i^2(\phi,\lambda)}}\\ \frac{\hat{S}_i(\phi,\lambda)}{\sqrt{\hat{C}_i^2(\phi,\lambda)+\hat{S}_i^2(\phi,\lambda)}}\end{bmatrix} \tag{4.29.1}$$

$$D\{\hat{G}_i(\phi,\lambda)\} = \left[-\frac{\hat{S}_i(\phi,\lambda)}{\hat{C}_i^2(\phi,\lambda)+\hat{S}_i^2(\phi,\lambda)} \quad \frac{\hat{C}_i(\phi,\lambda)}{\hat{C}_i^2(\phi,\lambda)+\hat{S}_i^2(\phi,\lambda)}\right] D\begin{Bmatrix}\hat{C}_i(\phi,\lambda)\\ \hat{S}_i(\phi,\lambda)\end{Bmatrix}\begin{bmatrix}-\frac{\hat{S}_i(\phi,\lambda)}{\hat{C}_i^2(\phi,\lambda)+\hat{S}_i^2(\phi,\lambda)}\\ \frac{\hat{C}_i(\phi,\lambda)}{\hat{C}_i^2(\phi,\lambda)+\hat{S}_i^2(\phi,\lambda)}\end{bmatrix} \tag{4.29.2}$$

with the covariance:

$$C\{\hat{H}_i(\phi,\lambda),\hat{G}_i(\phi,\lambda)\} = \frac{1}{f_i}\left[\frac{\hat{C}_i(\phi,\lambda)}{\sqrt{\hat{C}_i^2(\phi,\lambda)+\hat{S}_i^2(\phi,\lambda)}} \quad \frac{\hat{S}_i(\phi,\lambda)}{\sqrt{\hat{C}_i^2(\phi,\lambda)+\hat{S}_i^2(\phi,\lambda)}}\right] D\begin{Bmatrix}\hat{C}_i(\phi,\lambda)\\ \hat{S}_i(\phi,\lambda)\end{Bmatrix}\begin{bmatrix}-\frac{\hat{S}_i(\phi,\lambda)}{\hat{C}_i^2(\phi,\lambda)+\hat{S}_i^2(\phi,\lambda)}\\ \frac{\hat{C}_i(\phi,\lambda)}{\hat{C}_i^2(\phi,\lambda)+\hat{S}_i^2(\phi,\lambda)}\end{bmatrix} \tag{4.29.3}$$

Here, the slope of the ocean tidal signal b is considered a nuisance parameter and, thus, eliminated by using the transformed or Gauss-Helmert Model described beforehand, with the matrices A_1, A_2, and B fulfilling the condition of $rank(B) + rank(A_1) = 7 + 1 = 8$ as follows:

$$\underset{8\times 1}{A_1} = [t_1 - t_2, \quad t_3 - t_4, \quad \cdots \quad t_{2n-1} - t_{2n},]^T \tag{4.30.1}$$

$$\underset{8\times 4}{A_2} = \begin{bmatrix} \cos\Omega_{O1,1} - \cos\Omega_{O1,2} & \sin\Omega_{O1,1} - \sin\Omega_{O1,2} & \cos\Omega_{Q1,1} - \cos\Omega_{Q1,2} & \sin\Omega_{O1,1} - \sin\Omega_{Q1,2} \\ \cos\Omega o_{1,3} - \cos\Omega_{O1,4} & \sin\Omega_{O1,3} - \sin\Omega_{O1,4} & \cos\Omega_{Q1,3} - \cos\Omega_{Q1,4} & \sin\Omega_{O1,3} - \sin\Omega_{Q1,4} \\ \vdots & \vdots & \vdots & \vdots \\ \cos\Omega_{O1,15} - \cos\Omega_{O1,16} & \sin\Omega_{O1,15} - \sin\Omega_{O1,16} & \cos\Omega_{Q1,1} - \cos\Omega_{Q1,2} & \sin\Omega_{O1,15} - \sin\Omega_{Q1,16} \end{bmatrix} \tag{4.30.2}$$

$$B_{7\times 8} = \begin{bmatrix} -1 & 1 & 0 & 0 & \cdots & 0 \\ -1 & 0 & 1 & 0 & \cdots & 0 \\ -1 & 0 & 0 & 1 & \cdots & 0 \\ \vdots & \vdots & \vdots & \vdots & \ddots & \vdots \\ -1 & 0 & 0 & 0 & \cdots & 1 \end{bmatrix} \tag{4.30.3}$$

Once the tidal constituents are estimated, the tidal height $\hat{h}_i(t,\phi,\lambda)$ for a tidal constituent i is estimated by the following equation:

$$\hat{h}_i(t,\phi,\lambda) = f_i \hat{H}_i(\phi,\lambda) \cdot \cos(\Omega_{i,t} - \hat{G}_i(\phi,\lambda)) \tag{4.31}$$

where $\hat{H}_i(\phi,\lambda)$ and $\hat{G}_i(\phi,\lambda)$ are the estimated amplitude and phase of the tidal constituent i as defined in equation (4.28.1) and (4.28.2), respectively.

4.8 Results

When comparing estimates from InSAR data with model values, it is reasonable to do this over freely floating points with several kilometers from the ground line [Rignot et al., 2000]. Two points have been selected for tidal signal analysis: one at the center and the other at the edge of the ice tongue. Then, harmonic coefficients have been estimated for the tidal constituents O_1 and Q_1. However, due to the redundancy problem in the system, there are unacceptable errors in the amplitudes and phase estimates for the two constituents at both locations. Estimates are given in the Figures 4.10 through 4.13, and

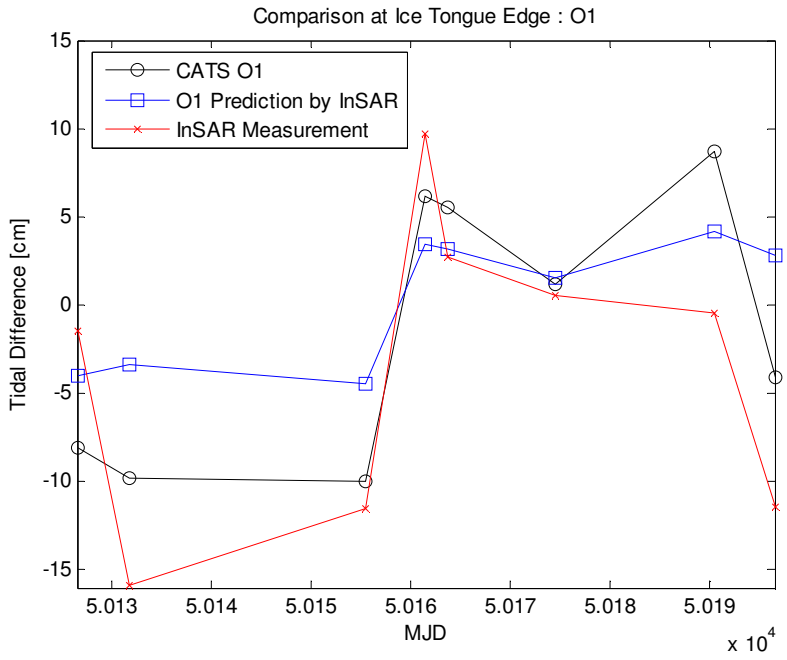

Figure 4.10. Tidal height comparison between the CATS02.01 model and InSAR based prediction at ice tongue edge for O_1.

the tidal height from different models is listed in Tables 4.13 and 4.14 with statistics from the estimation.

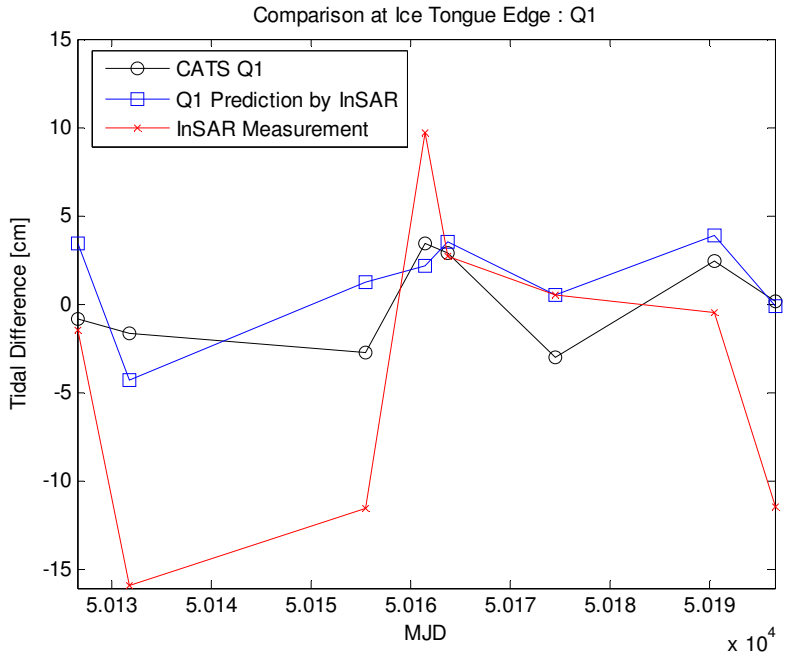

Figure 4.11. Tidal height comparison between the CATS02.01 model and InSAR based prediction at ice tongue edge for Q_1.

cm/degrees	CATS02.01	FES2004	GOT00.2	NAO.99b	TPXO.6.2	from InSAR
Amp O_1	30.6	29.3	26.3	30.7	33.2	16.3±16.8
Phase O_1	127.8	130.2	121.7	128.2	128.2	147.1±63.1
Amp Q_1	6.3	5.9	5.0	6.4	6.3	3.5±6.0
Phase Q_1	119.4	121.5	126.0	113.3	120.5	31.8±136.0

Table 4.13. Amplitude and phase from different tide models at the ice tongue edge.

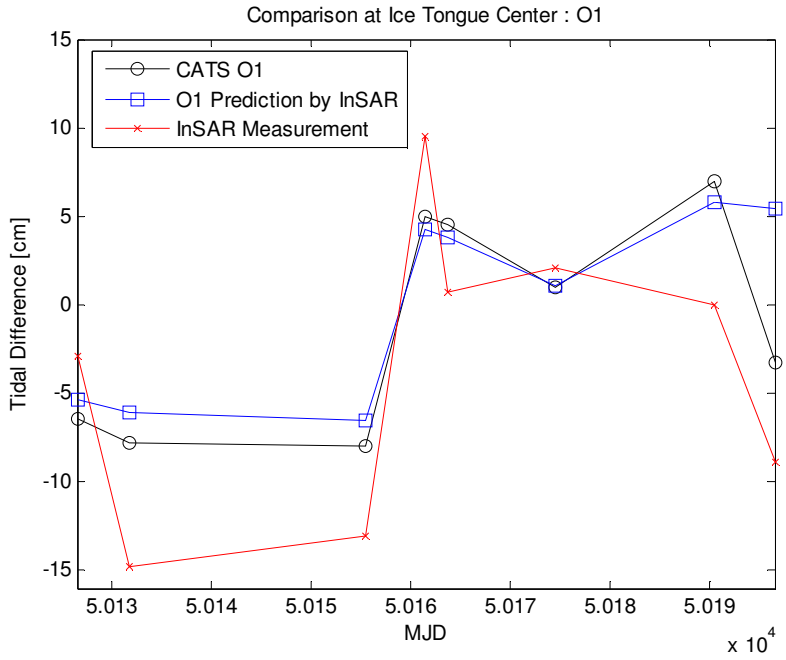

Figure 4.12. Tidal height comparison between the CATS02.01 model and InSAR based prediction at ice tongue center for O_1.

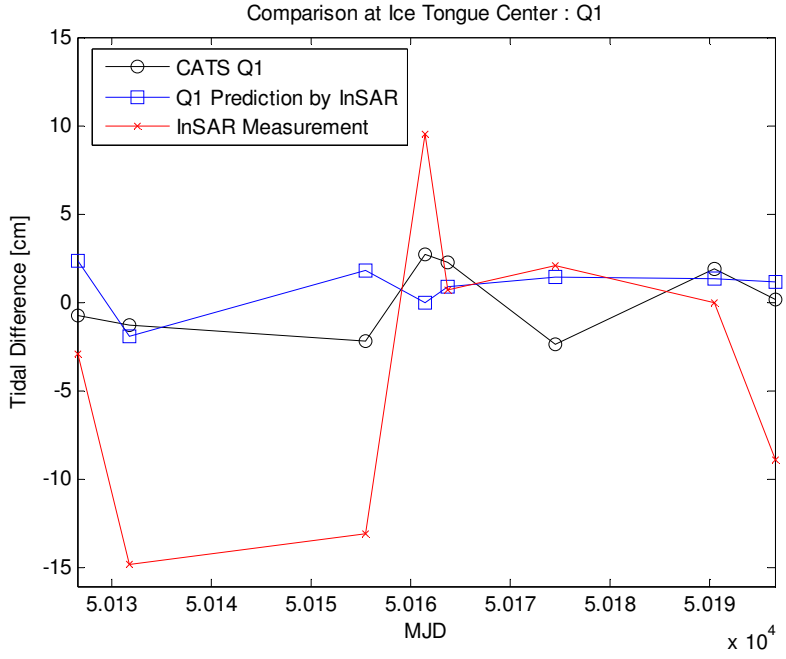

Figure 4.13. Tidal height comparison between the CATS02.01 model and InSAR based prediction at ice tongue center for Q_1.

cm/degrees	CATS02.01	FES2004	GOT00.2	NAO.99b	TPXO.6.2	from InSAR
Amp O_1	24.4	29.0	26.5	30.6	33.1	16.3±15.3
Phase O_1	128.2	130.5	121.5	128.4	128.2	149.5±61.7
Amp Q_1	5.1	5.9	5.0	6.3	6.3	2.5±5.7
Phase Q_1	119.7	121.1	126.0	113.1	120.5	31.1±175.8

Table 4.14. Amplitude and phase from different tide models at the ice tongue center.

As shown in Tables 4.13 and 4.14, the error is not within an acceptable range, and it is concluded that the parameters ought to be limited only to the most dominant tide signal O_1.

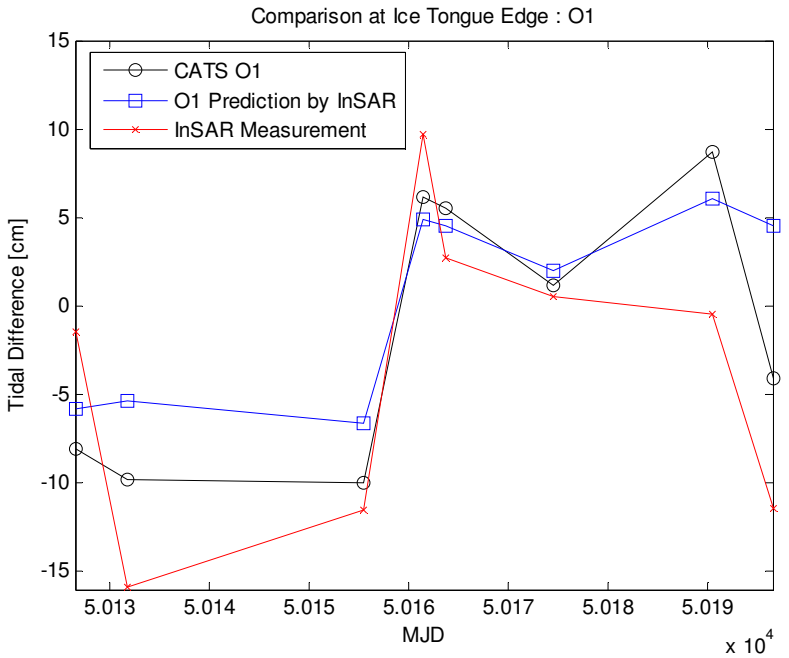

Figure 4.14. Tidal height comparison between the CATS02.01 model and InSAR based prediction at ice tongue edge only for O_1.

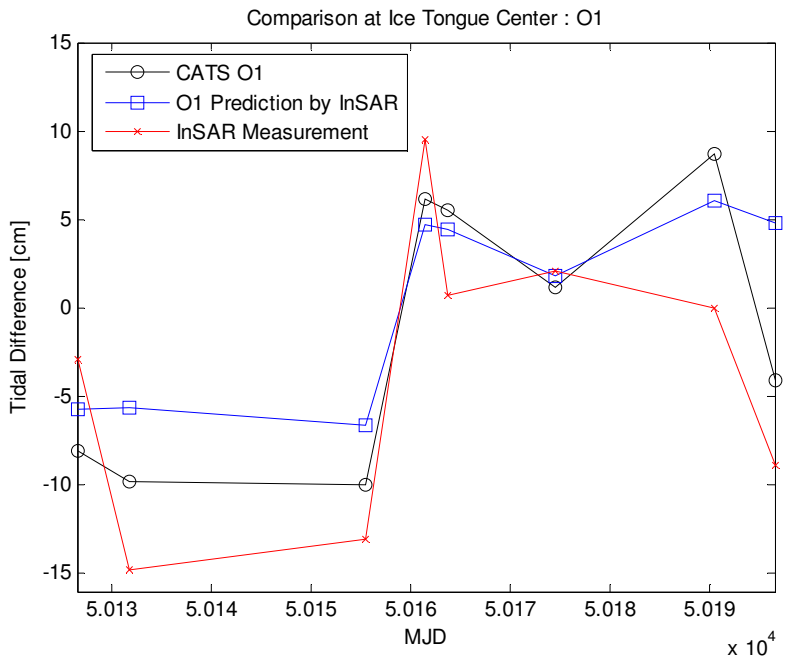

Figure 4.15. Tidal height comparison between the CATS02.01 model and InSAR based prediction at ice tongue center only for O_1.

	Amplitude, cm	rms error, ±cm	Phase, deg	rms error, ±deg
Ice tongue Edge	17.4	7.8	155.7	34.8
Ice tongue Center	17.1	7.2	155.6	32.7

Table 4.15. Estimates for the O_1 tidal constituent from InSAR measurements.

Table 4.15 shows the results for the O_1 only estimate of the tidal signal for both locations, with amplitude and phase about 17 cm and 155°. Their rms errors are about ±7 cm and ±34°.

4.9 Hypothesis Tests

First, with the estimate for the O_1 tide only, a null hypothesis H_0 and the alternative hypothesis H_a are set up as:

$$H_0 : \begin{bmatrix} C_{Q_1} & S_{Q_1} \end{bmatrix} = \begin{bmatrix} 0 & 0 \end{bmatrix} \tag{4.32.1}$$

$$H_a : \begin{bmatrix} C_{Q_1} & S_{Q_1} \end{bmatrix} \neq \begin{bmatrix} 0 & 0 \end{bmatrix} \tag{4.32.2}$$

For the hypothesis test, the Gauss-Helmert Model with fixed constraints is defined as:

$$\begin{aligned} w &= \overline{A}\,\xi_2 + Be, \quad e \sim (0, \sigma_0^2 P^{-1}) \\ \kappa_0 &= K\xi_2 \end{aligned} \tag{4.33}$$

where κ_0 is a $l \times 1$ zero vector, i.e., l=2 in this case, for harmonic coefficients of the Q_1 tidal constituent, K is a $l \times m$ design matrix, i.e., 2×4 here, for the constraints. The test statistic T is written as:

$$T = \frac{R/l}{\Omega/(n - rank(\overline{A}))} \sim F(l, n - rank(\overline{A})) \tag{4.34}$$

where $R = (\kappa_0 - KN^{-1}c)^T (KN^{-1}K^T)^{-1} (\kappa_0 - KN^{-1}c)$, $\Omega = (w - \overline{A}N^{-1}c)^T P (w - \overline{A}N^{-1}c)$, F stands for the argument of the F distributions.

For the first test, $\xi_2 = [C_{O_1} \quad S_{O_1} \quad C_{Q_1} \quad S_{Q_1}]$, $\kappa_0 = [0 \quad 0]^T$, and $K = \begin{bmatrix} 0 & 0 & 1 & 0 \\ 0 & 0 & 0 & 1 \end{bmatrix}$. With the F-test checking if the tidal harmonic coefficients of Q_1 are 0, the hypothesis test was accepted with an error probability of 5% since the values of 1.16 (ice edge) and 0.39 (ice center) as critical value of the F-test for the degrees of freedom (2, 3) which is 9.55.

Second, it is speculated whether the O_1 tide only estimate is 0 or not by setting up hypothesis as:

$$H_0 : \begin{bmatrix} C_{O_1} & S_{O_1} \end{bmatrix} = \begin{bmatrix} 0 & 0 \end{bmatrix} \tag{4.33.1}$$

$$H_a : \begin{bmatrix} C_{O_1} & S_{O_1} \end{bmatrix} \neq \begin{bmatrix} 0 & 0 \end{bmatrix} \tag{4.33.2}$$

The value for the test statistics was 3.78 with critical value of the F-test for the degrees of freedom (2, 5) which is 5.81 and 3.78 for error probability of 5% and 10%, respectively.

Third, it is tested whether the O_1 tide only estimate from InSAR measurements is statistically the same as model values from CATS02.01 by setting up hypothesis as:

$$H_0 : \lfloor C_{O_1} \quad S_{O_1} \rfloor = \lfloor C_{O_1} \quad S_{O_1} \rfloor_{CATS02.01} \tag{4.34.1}$$

$$H_a : \lfloor C_{O_1} \quad S_{O_1} \rfloor \neq \lfloor C_{O_1} \quad S_{O_1} \rfloor_{CATS02.01} \tag{4.34.2}$$

In this test, the test statistic value was 3.09 which is corresponding to the critical value for an error probability of about 15% for the *F*-test degree of freedom (2, 5). Based on the second and third hypothesis tests, at an error probability of 10%, the InSAR estimate is significant but is likely to be the same as the values from CATS02.01 model.

Figures 4.16 and 4.17 show the tidal amplitude and phase estimates for the O_1 tide, along with their rms errors over the study area with 200 m resolution. The advantage of using SAR interferometry in tidal studies lies in the very high horizontal resolution even up to tens of meters covered by each SAR image. Tides detected around small objects that are not resolvable by the typical grid spacing of ocean tidal models (>10 km) may contribute to iceberg calving and ocean cavity study under the ice shelf [Rignot et al., 2000]. According to the figures over the ice tongue, there is a smooth change from the grounding line to the edge both in amplitude and phase. Around the grounding line it shows a smaller amplitude (<15 cm) than in the main body of the ice tongue (see Figure 4.16), whereas the left side of the image depicted in yellow and green shows a big tidal amplitude up to 30 cm. This is a separated part from the main ice tongue and moves more freely than the main body. The difference between the freely floating part and the main ice tongue body is about 10 cm in the image and this is close to the difference between the values from the tide models and the InSAR based estimates. Therefore, in InSAR applications, the assumption of free floating for an ice shelf or ice tongue that is connected at one side with the ground needs to be corrected when more accurate estimation is desired. Due to the ice/ocean interface, there is a dissipation of tidal energy at the bottom of the floating ice [MacAyeal, 1984] which could reduce the tidal height change as observed on the ice surface.

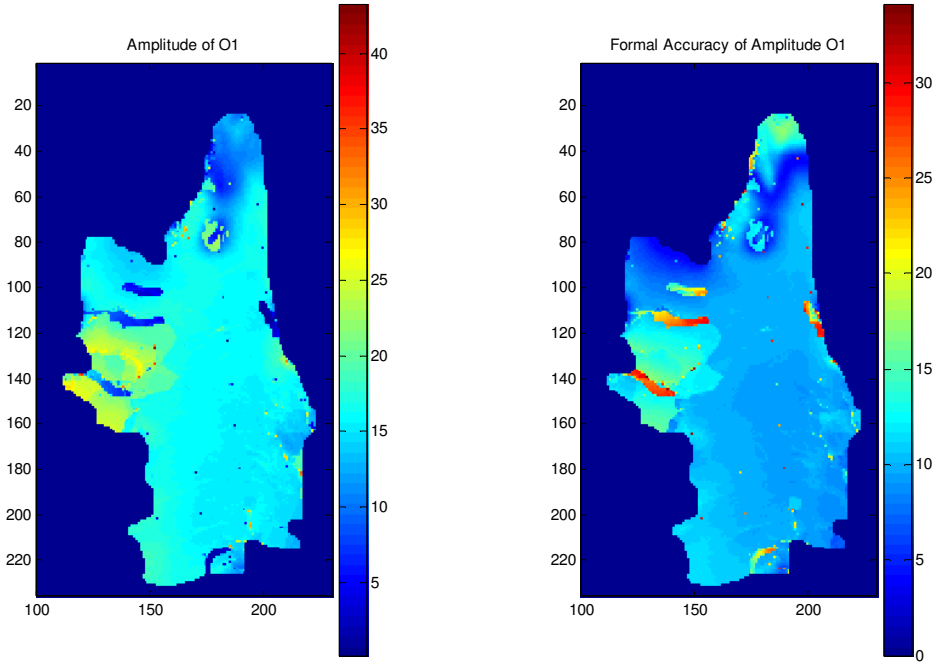

Figure 4.16. Amplitude estimate of O_1 and its rms error with 200m resolution.

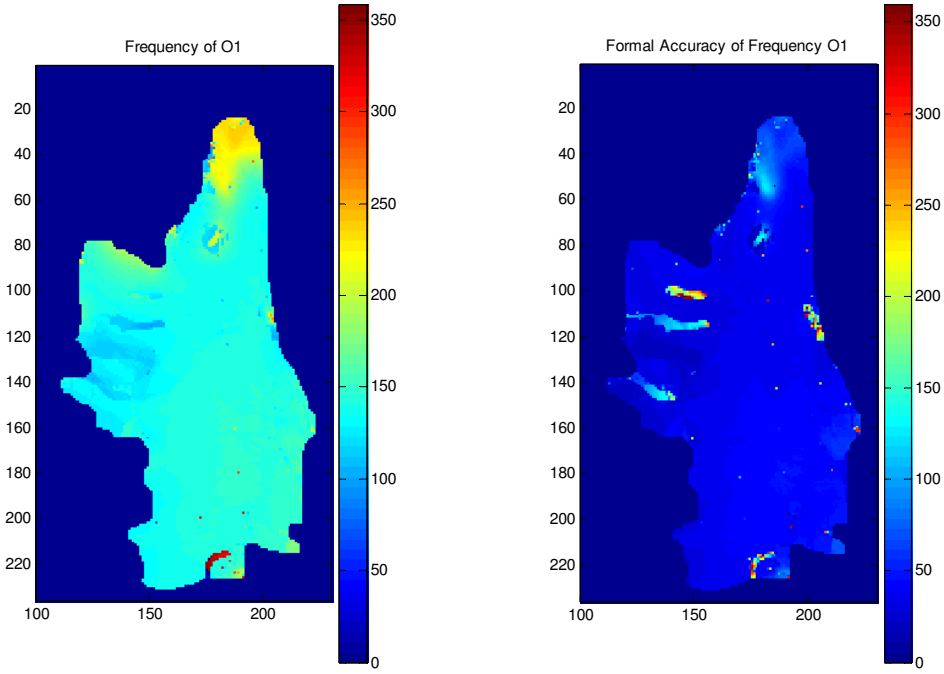

Figure 4.17. Phase estimate of O_1 and its rms error with 200m resolution.

4. 10 Discussion and conclusions

The estimated tide signal from InSAR measurements in this study was compared with global or regional Antarctic tide models including NAO.99b, TPXO.6.2, GOT00.2, CATS02.01, and FES2004. Even though the lack of data hinders the effort to readily develop a full tide model using a longer data span (time series may span over years), the estimated tidal constituents represent the first attempt to derive such a high-resolution tide model over an Antarctic ice shelf using InSAR. It is assumed that most other tidal signals except O_1 are below the noise level and therefore set to zero. However, those relatively small tides within the estimation error may still affect the observations. Because of this dissipation, the amplitude of the estimate could be too small. To see the effect of the small tides, the model values for those small tides were introduced from CATS02.01 and removed from InSAR observations for an alternative processing of the O_1 tide estimate. It is shown that the amplitude increased up to about 25 cm with an rms error of ±8.3 cm and ±10.2 cm at ice tongue center and edge, respectively (Table 4.16).

CHAPTER 5

THE USE OF InSAR IN MASS BALANCE STUDIES

5.1 Mass balance studies over ice sheets

The Antarctic and Greenland ice sheets contain enough water to raise the global sea level by 70 m [Rignot and Thomas, 2002; Velicogna and Wahr, 2006; Church et al., 2001]. Recently using GRACE observations, [Chen et al., 2006] reported the rate of mass loss in West Antarctica with (-77±14) km^3/yr while East Antarctica a gain of shows +80±16 km^3/yr. Sudden collapse or fast melting of the ice sheets can cause a significant sea level rise [Bindschadler, 1991]. In spite of its importance in sea level rise, any accurate quantification of ice sheet mass balances remains difficult primarily because of the remoteness of the polar regions and their unfavorable weather conditions. The ERS/ENVISAT altimeters and ICESat [Zwally et al., 2002], as well as airborne laser measurements covering higher latitudes than the previous altimeter missions, helped to estimate the mass balance over the polar regions. The GRACE, a spaceborne gravimetry mission [Tapley et al., 2004], provides additional measurements beginning to allow one towards quantifying the role of ice sheet mass balance on global sea level change.

Estimating the ice mass balance of the ice sheets has three major categories: measuring the mass budget, measuring any elevation change, and weighing the ice sheets [Rignot and Thomas, 2002]. First, the mass budget method compares any mass

	Glaciers	Ice Caps	Glaciers and ice caps	Greenland ice sheet	Antarctic ice sheet
Number	>160000	70	-	-	-
Area (10^6 km^2)	0.43	0.24	0.68	1.71	12.37
Volume (10^6 km^3)	0.08	0.10	0.18±0.04	2.85	25.71
Equivalent Sea-level rise (mm/yr)	0.24	0.27	0.50±0.10	7.2	61.1
Accumulation (sea level equivalent, mm/yr)	-	-	1.9±0.3	1.4±0.1	5.1±0.2

Table 5.1. Physical characteristics of ice on earth [Church et al., 2001].

accumulation in the interior with the mass discharge. Accumulation can be estimated by ice coring, and the discharge over a small ice shelf is estimated from GPS and InSAR derived ice surface velocity. The second task is to measure any elevation change. Given the time series of elevation over a certain location, it can be converted to volume change over that location. Satellite altimeters such as ERS-1/2 and ICESat covering the ice shelves within high latitudes provide such elevation changes. [Fricker et al., 2001] used an ERS-derived digital elevation model over the Amery ice shelf to convert the elevation into an ice thickness. NASA's new laser satellite altimeter ICESat was used to estimate the elevation change over a glacier in Alaska [Sauber et al., 2005] and the Antarctica ice shelf [Fricker et al., 2005]. Lastly, mass balance can be inferred by weighing the ice sheets. The NASA GRACE satellite provides the ice mass balance estimates through inference from spaceborne gravity change measurements [Velicogna & Wahr, 2006; Chen et al., 2006].

5. 2 InSAR Contribution to Mass Balance Studies

Among the three categories of ice mass balance studies, InSAR can be used for the mass budget task. It can provide a grounding line location, ice velocity, and ice sheet surface topography.

5.2.1 Grounding Line Detection

The grounding line is a transition line from grounded ice into ice floating over the ocean. Its location is used to define the boundary condition for ocean tide modeling [King et al., 2005]. In addition, it plays an important role as an indicator of the ice thickness change; if the ice melts and is getting thinner, the grounding line will retreat and vice versa. [Goldstein et al., 1993] showed the use of a single interferogram pair to locate the grounding line of the Rutford ice stream flowing into the Ronne Ice Shelf. A differential interferometry method was developed by Rignot [1998] to improve the accuracy of the grounding line. As can be seen in Figure 4.3, the differential interferogram combining two interferograms shows the dense fringe belt around the ice tongue at Sulzberger Ice Shelf, West Antarctica. The grounding line is located somewhere in the belt along the fringe line. Usually in InSAR studies, the inmost fringe line is selected as an InSAR grounding line at the expense of accuracy [Rignot and MacAyeal, 1998].

5.2.2 Ice Velocity Estimation

The surface ice velocity provides the rate of transportation from the accumulation region to ablation [Rosen et al., 2000]. The information for the velocity and its gradient are important for the mass balance estimation. Ground-based measurements of ice surface velocity are rare, due to the harsh weather condition over polar regions. InSAR can observe both the surface topography and the ice surface velocity over the polar regions. First ice velocity measurements using repeat-pass interferometry were reported by Goldstein et al. [1993]. The ocean tidal motion of the Hemmen Ice Rise on the Filchner–Ronne Ice Shelf was studied by Hartl et al. [1994].

Figure 5.1 shows the ice surface velocity over the Sulzberger Ice Shelf. It was estimated by combining range and azimuth direction velocity. The range velocity was detected by the tandem pair of ERS-1 23959 and ERS-2 4286. On the other hand, the azimuth velocity was estimated by the speckle matching technique. The flow directions observed by the flow stripes in the imagery are used as control data. This study shows that the maximum and mean speed in this area is ~509 and ~131m/year, respectively.

5.2.3 Ice Sheet Surface Topography

Topography data are useful to map the boundary of ice sheets for a single drainage outlet, and high-resolution DEM's are important for glacier dynamics modeling. In spite of radar altimetry flying over high latitudes, their poor horizontal resolution (~a couple of km) could not provide sufficient topography over ice shelves.

Using the above mentioned contributions, InSAR has been used for mass balance studies over Greenland and Antarctica. [Rignot, 2002] estimated the mass balance of nine East Antarctic glaciers and ice shelves using InSAR. [Rignot and Thomas, 2002] reported that the Greenland ice sheet is losing mass by near-coastal thinning, and that the West Antarctic Ice Sheet, with thickening in the west and thinning in the north, is probably thinning overall. Discharge on the Humboldt and Petermann Glaciers in Greenland was studied by Joughin et al. [1999] by combining InSAR measured surface velocity data with ice thickness data from airborne radar depth sound.

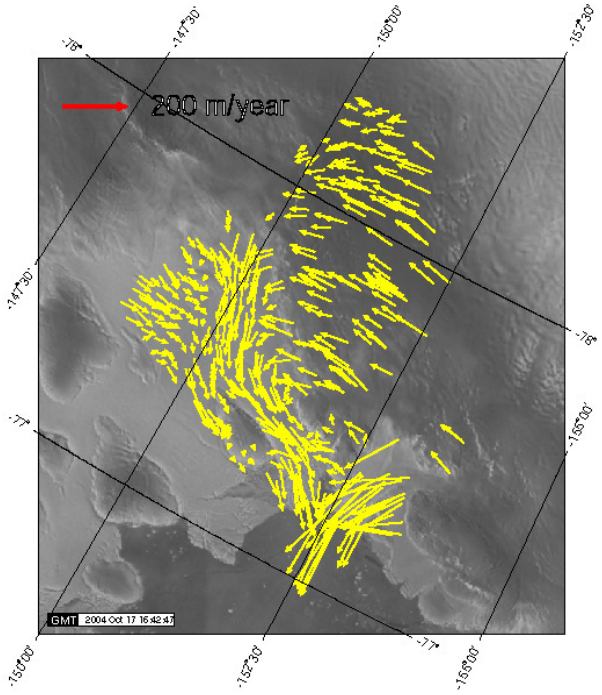

Figure 5.1. Ice surface velocity estimated by InSAR over the Sulzberger Ice Shelf.

CHAPTER 6

CONCLUSIONS AND FUTURE STUDIES

In glaciological studies, topography information is pretty basic and very important for many tasks such as ice surface deformation studies, tidal dynamics, ice shelf grounding line detection, and estimation of grounding zone topography. The results in Chapter 3 demonstrate the benefits of a novel technique to generate a high-resolution (60-m) DEM by differential SAR interferometry, using satellite laser altimeter data from GLAS/ICESat to replace ground control points. Using ICESat profiles in this remote place where it is difficult to have in-situ GCPs, successfully yields DEM with an accuracy at the meter level. It is concluded that the differential InSAR technique, incorporated with ICESat laser altimeter data, is a cost-effective method for generating DEMs in remote areas like Antarctica. It is shown that the InSAR and ICESat provide complementary data that form the basis for the generation of accurate (several meters) and high-resolution (60-m) DEM in Antarctica. The results presented in Chapter 3 indicate that there is a great improvement in topography possible, compared to the RAMP DEM which was generated based on radar altimetry over the study area. The results given in section 3.5 indicate that there may still be considerable localized errors in InSAR DEM even after baseline refinement. These errors can be removed by the bicubic spline method which, however, constitutes a sequential adjustment. Moreover, this is not the ideal solution due to the wide space between ICESat profiles over the study area. Thus, more research work is needed to find and properly remove the localized errors. The NASA/Goddard Space Flight Center is preparing an ICESat DEM over Antarctica, planned to be released in early 2007. It will provide the most complete and accurate topographical survey of the continent ever undertaken, with more than 65 million points surveyed from space by the GLAS onboard ICESat. The improved mapping of the height of the ice sheet will provide information about the topography effect for ice flow of this remote region of the planet. Even in light of the anticipated ICESat Antarctic topography map, which will have ~170 m along-track resolution and much coarser horizontal resolution, the here developed technique using InSAR for a high-resolution (60-m) DEM is beneficial to densify the ICESat DEM.

The results presented in Chapter 4 are to demonstrate, for the first time, that tidal constituents can be estimated underneath an ice shelf (ice tongue) using InSAR time series. First, it is shown that the time series of tidal differences from InSAR is comparable to those of global/regional ocean tide models such as NAO.99b, TPXO.6.2, GOT99.2, CATS02.01, and FES2004. It shows that InSAR observations are sensitive to the tidal signal over the chosen and that, among the ocean tide models, CATS02.01 is the

best-fitting model when compared with InSAR observations over this area; this is in qualitative agreement with previous research work [King et al., 2005]. However, there is no significant difference between the ocean tide models since most of the developed tide models used primarily the same information (bathymetry and boundary). In our study, the development of a full tide model using InSAR is not feasible, due primarily to the limited number of observations and the data span (71 days) from the ERS tandem mission as well as the peculiar ERS orbit characteristics; the most dominant tide O_1 has been estimated with formal error ~±8 cm for amplitude and ±34° for phase, respectively. In this solution, the amplitude is smaller than those predicted by other ocean tide models. Since no more ERS tandem data are available, the use of the combined information from different sensors can help InSAR to overcome both the limited number of observations and the short time span. In the procedure of combining two different types of observations, the same weighting factors are applied to both observations at this time. The weighting factors and induced correlation should be studied as a topic in the future, as well as the use of other data types, including ENVISAT and Geosat Follow-On (GFO) radar altimetry, as well as GRACE [Han et al., 2005]. The integration of various datasets such as InSAR, ICESat laser altimetry, ERS/ENVISAT/GFO radar altimetry, and GRACE gravimetry is anticipated to improve our understanding of ocean tidal dynamics underneath the ice shelves, and their roles in the determination of ice sheet mass balances in Antarctica. The methods and results given in Chapter 4 can also be applied to other areas with poor accuracy and low resolution. Especially the Filchner Ronne Ice Shelve in

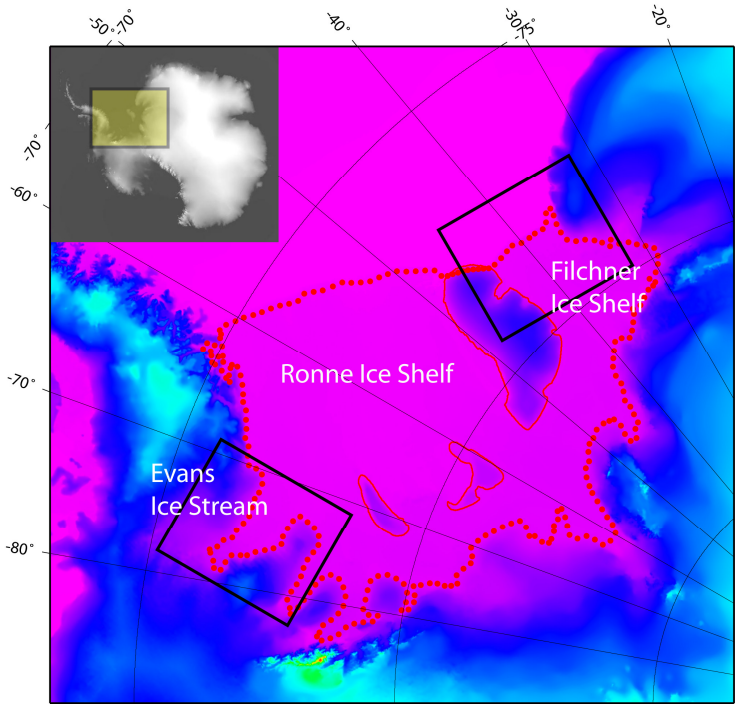

Figure 6.1. Filchner Ronne Ice Shelf (FRIS). The grounding line from the Antarctic Digital Database (ADD) is depicted in red dots on top of the RAMP DEM. Available ERS tandem missions over these two areas are listed in Table 6.1.

the Weddell Sea, Antarctica, shows a big amplitude which reaches up to more than 1 meter for some constituents and there is a relatively big difference between existing tide models over this area. The two boxes in Figure 6.1 show available ERS tandem mission datasets near the grounding line, and the Tables 6.1 and 6.2 list tandem pairs for the Filchner Ice Shelf and the Evans Ice Stream, respectively. It covers January through March, spanning about 70 days over the Filchner Ice Shelf and 61 days over the Evans Ice Stream. In Chapter 4, the combination of InSAR and ICESat has been shown to be capable of providing much longer time spans in tidal studies. The integration of various datasets such as InSAR, ICESat, ERS altimetry, and GRACE can improve our understanding of tides underneath ice shelves over this area.

Track	ERS-1	ERS-2
5	23540	3867
	24041	4368
20	23555	3882
	24056	4383
62	24098	4425
	23597	3924
77	24113	4440
105	24141	4468
191	23726	4053
	24227	4554
206	24242	4569
248	23783	4110
320	23855	4182
355	24371	4698
363	23898	4225
	24399	4726
377	23912	4239
392	23927	4254
	24428	4755
449	24485	4812
	23984	4311
277	23812	4139
249	24285	4612
263	23798	4125
378	23913	4240

Table 6.1. ERS tandem pairs over the Filchner Ice Shelf

Track	ERS-1	ERS-2
20	23555	3882
	24056	4383
37	24073	4400
51	24087	4414
94	24130	4457
180	24216	4543
392	23927	4254
	24428	4755

Table 6. 2. ERS tandem pairs over the Evans Ice Stream

REFERENCES

Abshire, J., X.L. Sun, H. Riris, J. M. Sirota, J. F. McGarry, S. Palm, D. H. Yi, and P. Liiva, Geoscience Laser Altimeter System (GLAS) on the ICESat Mission: On-orbit measurement performance, Geophys. Res. Lett., vol. 32, L21S02, doi:10.1029/2005GL024028, 2005.

Bamber, J. L., and R. A. Bindschadler, An improved elevation dataset for climate and ice-sheet modelling: validation with satellite imagery, Annals of Glaciology, vol. 25, pp.439-444, 1997.

Bamler, R. and P. Hartl, Synthetic aperture radar interferometry, Inverse Problems, vol. 14, pp. R1-R54, 1998.

Bamler, R. and D. Just, Phase statistics and decorrelation in SAR interferograms, in Proc. Int. Geosci. Remote Sensing Symp., Tokyo, Japan, August 18-21, pp. 980-984, 1993.

Bindschadler, R. A., (Ed.), West Antarctic ice sheet initiative, vol. 1: Science and impact plan, NASA Conf. Pub., no. 3115, 1991.

Braun, A., K. Cheng, B. Csatho, and C. K. Shum, ICESat laser altimetry in the great lakes, presented at the Inst. of Navigation (ION) 60th Ann. Meeting, Dayton, OH, 2004.

Brown, E.W and H. B. Hedrick, Tables of the Motion of the Moon. Yale Univ. Press, New Haven CT, 1919.

Cartwright D. E. and R. J. Tayler, New computations of the tide-generating potential, Geophys. J. R. Astr. Soc. vol. 23, pp. 45-74, 1970.

Casotto, S., Ocean tide models for TOPEX precise orbit determination, Ph. D. thesis, Center for Space Research, The University of Texas, Austin, TX, 1989.

Cenzo, A. D., Synthetic Aperture Radar and Digital Processing: An Introduction, JPL Publication 80-90, 1981.

Chen, J. L., C. R. Wilson, D. D. Blankenship, B. D. Tapley, Antarctic mass rates from GRACE, Geophys. Res. Letts, vol. 33, L11502, doi:10.1029/2006GL026369, 2006.

Cheney, M., Introduction to Synthetic Aperture Radar (SAR) and SAR Interferometry, in Approximation Theory X: Wavelets, splines, and Applications, ed. C.K. Chui, L.L. Schumaker, and J. Stoeckler, Vanderbilt Univ. Press, Nashville, TN, pp. 167-177, 2001.

Church, J.A., J.M. Gregory, P. Huybrechts, M. Kuhn, C. Lambeck, M.T. Nhuan, D. Qin, P.L. Woodworth, Changes in sea level. in: J.T Houghton, Y. Ding, D.J. Griggs, M. Noguer, P.J. van der Linden, X. Dai, K. Maskell, and C.A. Johnson (eds.): Climate Change 2001: The Scientific Basis, Contribution of Working Group I to the Third Assessment Report of the Intergovernmental Panel on Climate Change, Cambridge University Press, Cambridge, MA, pp. 639-694, 2001.

Cressie, N., Statistics for Spatial Data, 2nd edition, John Wiley and Sons, New York, NY, 1993

Curlander, J. C. and R. N. McDonough, Synthetic Aperture Radar Systems and Signal Processing. New York: Wiley-Interscience, 1991.

Doodson, A. T., The harmonic development of the tide-generating potential, Proc. Roy. Soc. Lond., pp. 305-329, 1921.

Doodson, A. T., The analysis of tidal observations. Phil. Trans. Roy. Soc. Lond., vol. 227, pp. 223-279, 1928.

Egbert, G. D. and L. Erofeeva, Efficient inverse modeling of barotropic ocean tides, J. Atmos. Oceanic Technol., vol. 19, no. 2, pp. 183-204, 2002.

Egbert, G. D., A. F. Bennett, M. G. G. Foreman, Topex/Poseidon tides estimated using a global inverse model, J. Geophys. Res., vol. 99, pp. 24821-24852, 1994.

Elachi, C., Introduction to the Physics and Techniques of Remote Sensing, John Wiley and Sons, New York, NY, 1987.

Eldhuset, K., P. H. Andersen , S. Hauge, E. Isaksson, D. J. Weydahl, ERS tandem InSAR processing for DEM generation, glacier motion estimation and coherence analysis on Svalbard, International Journal of Remote Sensing, vol. 24, no. 7, pp. 1415-1437, 2003.

Fatland, D. R. and C. S. Lingle, Analysis of the 1993-95 Bering Glacier (Alaska) surge using differential SAR interferometry, J. Glaciol., vol. 44, no. 148, pp. 532-546, 1998.

Ferretti, A., C Prati, F Rocca, Permanent scatterers in SAR interferometry, IEEE Trans. Geos. Rem. Sens., vol. 39, no. 1, pp. 8-20, 2001.

Fitch, J. P., Synthetic Aperture Radar, Springer-Verlag, New York, 1988.

Fricker, H.A., S. Popov, I. Allison, and N. Young, Distribution of marine ice beneath the Amery Ice Shelf, Geophys. Res. Letts., vol. 28, no. 11, pp. 2241-2244, 2001.

Fricker, H. A. and L. Padman, Tides on Filchner-Ronne Ice Shelf from ERS radar altimetry, Geophys. Res. Letts, vol. 29, no. 12, 1622, 10.1029/2001GL014175, 2002.

Fricker, H. A., J. N. Bassis, B. Minster, and D. R. MacAyeal, ICESat's new perspective on ice shelf rifts: The vertical dimension, Geophys. Res. Letts. vol. 32, L23S08, doi:10.1029/2005GL025070, 2005

Franceschetti, G. and R. Lanari, Synthetic Aperture Radar Processing, CRC Press, New York, 1999.

Gabriel, A. K., R. M. Goldstein, and H. A. Zebker, Mapping small elevation changes over large areas: Differential radar interferometry, J. Geophys. Res., vol. 94, pp. 9183-9191, 1989.

Gibson, J.K., P. K?lberg, S. Uppala, A. Hernandez, A. Nomura, and E. Serrano. ERA Description. Re-Analysis (ERA) Project Report Series 1, ECMWF, Shinfield Park, Reading, U.K., 1997.

Goldstein, R. M., H. A. Zebker, and C. L. Werner, Satellite radar interferometry: Two-dimensional phase unwrapping, Radio Sci., vol. 23, no. 4, pp. 713-720, 1988.

Goldstein, R. M., H. Engelhardt, B. Kamb, and R. M. Frolich, Satellite radar interferometry for monitoring ice sheet motion: Application to an antarctic ice stream, Science, vol. 262, pp. 1525-1530, 1993.

Graham, L C , Synthetic interferometer radar for topographic mapping, IEEE. Proc., vol. 62, pp. 763-768, 1974.

Gray, A. L., K. Mattar, and G. Sofko, Influence of ionospheric electron density fluctuations on satellite radar interferometry, Geophys. Res.Lett., vol. 27, no. 10, pp. 1451-1454, 2000.

Gray, A. L., Short, N., Mattar, K.E., Jezek. K. C., Velocities and flux of the Filchner Ice Shelf and its tributaries determined from speckle tracking interferometry, Canadian J. Remote Sens., vol. 27, no. 3, pp. 193-206, 2001.

Hagberg, J. O., L. M. H. Ulander, and J. Askne, Repeat-pass SAR interferometry over forested terrain, IEEE Trans. Geosci. Remote Sensing, vol. 33, pp. 331-340, 1995.

Han, S. -C, C. K. Shum, and K. Matsumoto, GRACE observations of M2 and S2 ocean tides underneath the Filchner-Ronne and Larsen ice shelves, Antartica, Geophys. Res. Lett., vol. 32, L20311, doi:10.1029/2005GL024296, 2005.

Hanssen, R. F., Radar Interferometry: Data Interpretation and Error Analysis, Kluwer Academic Press, Dordrecht, The Netherlands, 2001.

Hartl, P., K. H. Thiel, X. Wu, C. Doake, and J. Sievers, Application of SAR interferometry with ERS-1 in the Antarctic, Earth Observation Quarterly, no. 43, pp. 1-4, 1994.

Henderson, F. M. and A. J. Lewis (eds.), Principles and Applications of Imaging Radar, vol. 2 of Manual of Remote Sensing, John Wiley and Sons, New York, NY, 3rd ed., 1998.

Hensley, S., R. Munjy, and P. Rosen, Interferometric synthetic aperture radar (IFSAR), in Digital Elevation Model Technologies and Applications: The DEM Users Manual, D. F. Maune, (Ed.) Bethesda, MD: Amer. Soc. Photogramm. Remote Sens., pp. 143-206, 2001.

Hoen, E. and H. Zebker, Penetration depths inferred from interferometric volume decorrelation observed over the Greenland ice sheet, IEEE Trans. Geosci. Remote Sens., vol. 38, no. 6, pp. 2571-2583, 2000.

Holdsworth, G. Flexure of a floating ice tongue, J. Glaciol., vol. 8, no. 54, pp. 385-397, 1969.

Holdsworth, G. Tidal interaction with ice shelves, Ann. Geophys., vol. 33, no. 1, pp. 133-146, 1977.

Jezek, K. C., RAMP AMM-1 SAR image mosaic of Antarctica, Alaska SAR Facility, Fairbanks, Alaska, 2002.

Jordan, R., The SEASAT-A Synthetic Aperture Radar System. IEEE J. Ocean Eng., vol. OE-5, No. 2, pp. 154-164, 1980.

Joughin, I., Estimation of Ice-Sheet Topography and Motion Using Interferometric Synthetic Aperture Radar, Ph.D. Thesis, Dept. of Electric Engineering, Univ. Washington, Seattle,1995.

Joughin, I., D. Winebrenner, M. Fahnestock, R. Kwok, and W. Krabill, Measurement of ice-sheet topography using satellite radar interferometry, J. Glaciol., vol. 42, pp. 10-22, 1996.

Joughin, I., M. Fahnestock, R. Kwok, P. Gogineni, and C. Allen, Ice flowof Humboldt, Petermann, and Ryder Gletscher, northern Greenland, J. Glaciology, vol. 45, no. 150, pp. 231-241, 1999.

King, M., N. T. Penna, P. J. Clarke, and E. C. King, Validation of tide models around Antarctica using onshore GPS and gravity data, J. Geophys. Res., vol. 110, B08401, doi:10.1029/2004JB003390, 2005.

King, M., R. Coleman, and P. Morgan, Treatment of horizontal and vertical tidal signals in GPS data: A case study on a floating ice shelf, Earth, Planets and Space, vol. 52, no. 11, pp. 1043-1047, 2000.

Kwok, R. and M. A. Fahnestock, Ice sheet motion and topography from radar interferometry, IEEE Trans. Geosci. Remote Sens., vol. 34, pp. 189-200, 1996.

Le Provost, C., M.L. Genco, F. Lyard, P. Vincent and P. Canceil, Tidal spectroscopy of the world ocean tides from a finite element hydrodynamic model, J. Geophys. Res., 99, C12, pp. 24777-24798, 1994.

Lefevre, F., F. H. Lyard, C. Le Provost, and E. J. O. Schrama, FES99: A global tide finite element solution assimilating tide gauge and altimetric information, J. Atmos. Oceanic Technol., vol. 19, no. 9, pp. 1345-1356, 2002.

Li, F. K. and R. M. Goldstein, Studies of multibaseline spaceborne interferometric synthetic aperture radars, IEEE Trans. Geosci. Remote Sens., vol. 28, no. 1, pp. 88-97, 1990.

Liu, H., K. C. Jezek, B. Li, and Z. Zhao, Radarsat Antarctic Mapping Project digital elevation model, version 2, Nat. Snow and Ice Data Center, Boulder, CO, 2001.

Liu, H., K. C. Jezek, and B. Li, Development of an Antarctic digital elevation model by integrating cartographic and remotely sensed data: A geographic information system based approach, J. Geophys. Res., vol. 104(B10), pp. 23,199-23 213, 1999.

MacAyeal, D. R., E. Rignot and C. L. Hulbe, Ice-shelf dynamics near the front of Filchner-Ronne Ice Shelf, Antarctica, revealed by SAR interferometry: Model/interferogram comparison, J. Glaciol., vol. 44, pp. 419-428, 1998.

MacAyeal, D. R., Numerical simulations of the Ross Sea tides. J. Geophys. Res., vol. 89, pp. 607-615, 1984.

Madsen, S. N. and H. A. Zebker, Synthetic aperture radar interferometry: Principles and applications, in: Manual of Remote Sensing. Boston, MA: Artech House, vol. 3, ch. 6, 1999.

Magruder, L. A., B. E. Schutz, and E. C. Silverberg, Laser pointing angle and time of measurement verification of the ICESat laser altimeter using a ground-based electro-optical detection system, J. Geodesy, vol. 77, no. 3-4, pp. 148-154, 2003.

Massonnet, D., M. Rossi, C. Carmona, F. Adragna, G. Peltzer, K. Fiegl, and T. Rabaute, The displacement field of the Landers earthquake mapped by radar interferometry, Nature, vol. 364, pp. 138-142, 1993.

Massonnet, D., K. Feigl, M. Rossi, and F. Adragna, Radar interferometric mapping of deformation in the year after the Landers earthquake, Nature, vol. 369, no. 6477, pp. 227-230, 1994.

Massonnet, D., P. Briole, and A. Arnaud, Deflation of Mount Etna monitored by spaceborne radar interferometry, Nature, vol. 375, pp. 567-570, 1995a.

Massonnet, D. and K. Feigl, Satellite radar interferometric map of the coseismic deformation field of the M=6.1 Eureka Valley, CA earthquake of May 17, 1993, Geophys. Res. Lett., vol. 22, pp. 1541-1544, 1995b.

Massonnet, D. and K. L. Feigl, Radar interferometry and its application to changes in the earth's surface, Rev. Geophys., vol. 36, no. 4, pp. 441-500, 1998.

Matsumoto, K., T. Takanezawa, and M. Ooe, Ocean tide models developed by assimilating TOPEX/POSEIDON altimeter data into hydrodynamical model: A global model and a regional model around Japan, J. Oceanogr., vol. 56, pp. 567-581, 2000.

McCarthy, D., ERS Conventions, IERS Technical note 21, 1996.

Meade, C. and D. T. Sandwell, Synthetic aperture radar for geodesy, Science, vol. 273. no. 5279, pp. 1181 - 1182, 1996.

Newcomb, S., Tables of the motion of the Earth on its axis around the Sun, Astronomical Papers prepared for the use of the American Ephemeris and Nautical Almanac, vol. 6, Part I, 1895.

Padman, L., H. A. Fricker, R. Coleman, S. Howard, and S. Erofeeva, A new tidal model for the Antarctic ice shelves and seas, Ann. Glaciol., vol. 34, pp. 247-254, 2002.

Padman, L., M. King, D. Goring, H. Corr, R. Coleman, Ice shelf elevation changes due to atmospheric pressure variations, J. Glaciol., vol 49, no. 167, pp. 521-526, 2003a.

Padman, L., S. Erofeeva, and I. Joughin, Tides of the Ross Sea and Ross Ice Shelf cavity, Antarctic Science, vol 15, no. 1, pp. 31-40, 2003b.

Padman, L., and Ch. Kottmeier, High-frequency ice motion and divergence in the Weddell Sea, J. Geophys. Res., 105(C2), 3379-3400, 2000.

Peltzer, G. and P. Rosen, Surface displacement of the 17 May 1993 Eureka Valley, California, earthquake observed by SAR interferometry, Science, vol. 268, pp. 1333-1336, 1995.

Pugh, D. T., Tides, Surges, and Mean Sea Level, John Willey & Sons Ltd, New York, NY, 1996.

Ray, R. D., A global ocean tide model from Topex/Poseidon altimetry: GOT99.2, NASA Tech. Memo. 209478, Goddard Space Flight Center, 1999.

Reeh, N., C. Mayer, O. B. Olesen, E. L. Christensen and H. H. Thomsen, Tidal movement of Nioghalvfjerdsfjorden glacier, northeast Greenland: Observations and modeling, Ann. Glaciol., vol. 31, pp. 111-117, 2000.

Ridley, J.K. W. Cudlip, N.F. McIntyre and C.G. Rapley, The topography andsurface characteristics of the Larsen Ice Shelf, Antarctica, using satellite altimetry. J.Glaciol., vol. 35, no. 121, 229-310, 1989.

Rignot, E., Tidal motion, ice velocity, and melt rate of Petermann Gletscher, Greenland, measured from radar interferometry, J. Glaciology, vol. 42, no. 142, 1996.
Rignot, E. and D. R. MacAyeal, Ice-shelf dynamics near the front of Filchner-Ronne Ice Shelf, Antarctica, revealed by SAR interferometry, J. Glaciol., vol. 44, pp. 405-418, 1998.

Rignot, E., L. Padman, D. R. MacAyeal, and M. Schmeltz, Observation of ocean tides below the Filchner and Ronne Ice Shelves, Antarctica, using synthetic aperture radar interferometry: Comparison with tide model predictions, J. Geophys. Res., vol. 105(C8), pp. 19615-19630, 2000.

Rignot, E., K. Echelmeyer, and W. Krabill, Penetration depth of interferometric synthetic-aperture radar signals in snow and ice, Geophys.Res. Lett., vol. 28, no. 18, pp. 3501-3504, 2001.

Rignot, E., Mass balance of East Antarctic glaciers and ice shelves from satellite data, Ann. Glaciol. vol. 34, pp. 217-228, 2002.

Rignot E. and R. Thomas, Mass balance of the polar ice sheets, Science, vol. 297, pp. 1502-1506, 2002.

Rocca, F., C. Prati, A. Montiguarnieri, and A. Ferretti, SAR interferometry and its applications, Surveys Geophys., vol 21, pp. 159-176, 2000.

Rodriguez, E. and J. M. Martin, Theory and design of interferometric synthetic aperture radars, Proc. Inst. Elect. Eng. F, vol. 139, no. 2, pp. 147-159, 1992.

van Roessel, J. W. and R. D. de Godoy, SLAR Mosaic for Project RADAM, Photogram. Eng., vol. 40, pp. 583-595, 1974.

Rosen, P. A., S. Henseley, I. R. Joughin, F. K. Li, S. N. Madsen, E. Rodriguez, and R. M. Goldstein, Synthetic aperture radar interferometry, Proc. IEEE, vol. 88, no. 3, pp. 333-382, 2000.

Rufino, G., A. Moccia and S. Esposito, DEM generation by means of ERS tandem data, IEEE Trans. Geosci. Remote Sens., vol. 36, no. 6, pp. 1905-1912, 1998.

Sansosti, E., R. Lanari, G. Fornaro, G. Franceschetti, M. Tesauro, G. Puglisi, and M. Coltelli, Digital elevation model generation using ascending and descending ERS-1/ERS-2 tandem data, Int. J. Remot. Sens., vol. 20., no. 8, pp. 1527-1547, 1999.

Sauber, J., B. Molnia, C. Carabajal, S. Luthcke, and R. Muskett, Ice elevations and surface change on the Malaspina Glacier, Alaska, Geophys. Res. Letts. vol. 32. L23S01, doi:10.1029/2005GL023943, 2005.

Schmeltz, M., E. Rignot, D. MacAyeal, Tidal flexure along ice-sheet margins: Comparison of InSAR with an elastic-plate model, Ann. Glaciol., vol. 34, pp. 202-208, 2002.

Schutz, B. E., H. J. Zwally, C. A. Shuman, D. Hancock, and J. P. DiMarzio, Overview of the ICESat Mission, Geophys. Res. Lett., vol. 32, L21S01, doi:10.1029/2005GL024009, 2005.

Schutz, B.E., Spaceborne laser altimetry: 2001 and beyond, published in Plag, H.P. (ed.), Book of Extended Abstracts, WEGENER-98, Norwegian Mapping Authority, Honefoss, Norway, 1998

Schwiderski, E.W, Ocean tides, Part I: Global ocean tidal equations, Marine Geodesy, vol. 3,Nos. 1-4, pp. 161-217, 1980.

Seymour, M. S. and I. G. Cumming, Maximum likelihood estimation for SAR interferometry, in: Proc. IGARSS'94, pp. 2272-2275, 1994.
Shepherd, A. and N. R. Peacock, Ice shelf tidal motion derived from ERS altimetry, Geophys. Res. Lett., vol. 108(C6), doi:10.1029/2001JC001152, 2003.

Shum, C. K., Y. Yi, Y. Wang, S. Baek, O. Andersen, and Z. Lu, Ross sea tide modeling using InSAR and radar altimetry, AGU Fall Meet., San Francisco, December, 2002.

Shum, C. K., S. Baek, H. K. Lee, Z. Lu, O. -I. Kwoun, and A. Braun, Tidal dynamics, ice stream velocity and DEM in the Sulzberger Ice Shelf, West Antarctica, using SAR interferometry, NASA-JPL InSAR Workshop, Oxnard, CA, 2004.

Smith, A. J. E., Application of Satellite Altimetry for Global Ocean Tide Modeling, TU Delft, The Netherlands, 1999.
Smith, A. M., The use of tiltmeters to study the dynamics of Antarctic ice-shelf grounding lines, J. Glaciol., vol. 47, no. 156, pp. 71-77, 1991.

Tapley, B. D., S. Bettadpur, M. Watkins, and C. Reigber, The gravity recovery and climate experiment: Mission overview and early results, Geophys. Res. Letts. vol. 31, L09607, doi:10.1029/2004GL019920, 2004

Thomas, R. E. Rignot, G. Casassa, P. Kanagaratnam, C. Acuña, T. Akins, H. Brecher, E. Frederick, P. Gogineni,4 W. Krabill, S. Manizade, H. Ramamoorthy, A. Rivera, R. Russell, J. Sonntag, R. Swift, J. Yungel, J. Zwally, Accelerated sea-Level rise from West Antarctica, Science, vol. 306. no. 5694, pp. 255-258, 2004.

Ulaby, F. T., R. K. Moore, and A. K. Fung, Microwave Remote Sensing: Active and Passive, Norwood, MA: Artech House, 1981.

Vaughan, D., Investigating tidal flexure on an ice shelf using kinematic GPS, Ann. Glaciol., vol. 20, pp. 372-376, 1994.

Vaughan, D., Tidal flexure at ice shelf margins, J. Geophys. Res., vol. 100, no. B4, pp. 6213-6224, 1995.

Velicogna, I and J. Wahr, Measurements of Time-Variable Gravity Show Mass Loss in Antarctica, vol. 311, no. 5768, pp. 1754 - 1756, Science, 2006.

Viksne, A., T. C. Liston, and C. D. Sapp, SLR reconnaissance of Panama, Geophys., vol. 34, no. 1, pp. 54-64, 1969.

Wang, Y., Ocean tide modeling in the Southern ocean, OSU Report no. 471, Dept. of CEEGS, The Ohio State University, Columbus, OH, 2005.

Werner, C. L., U. Wegmueler, T. Strozzi, and A. Wiesmann, GAMMA SAR and interferometry processing software, presented at the ERSENVISAT Symp., Gothenburg, Sweden, Oct. 16-20, 2000.

Wingham, D., A. Ridout, R. Scharroo, A. Arthern, and C. K. Shum, Antarctic elevation change from 1992 to 1996, Science, vol. 282, pp. 456-458, 1998.
Zebker, H. A. and R. M. Goldstein, Topographic mapping from interferometric SAR observations, J. Geophys. Res., vol. 91, pp. 4993-4999, 1986.

Zebker, H. A. and J. Villasenor, Decorrelation in interferometric radar echoes, IEEE Trans. Geosci. Remote Sensing, vol. 30, pp. 950-959, 1992.

Zebker, H. A., S. N. Madsen, J. Martin, K. B. Wheeler, T. Miller, Y. Lou, G. Alberti, S. Vetrella, and A. Cucci, The TOPSAR interferometric radar topographic mapping instrument, IEEE Trans. Geosci. Remote Sensing, vol. 30, pp. 933-940, 1992.

Zebker, H. A., C. L.Werner, P. A. Rose, and S. Hensley, Accuracy of topographic maps derived from ERS-1 interferometric radar, IEEE Trans. Geosci. Remote Sens., vol. 32, no. 4, pp. 823-836, 1994a.

Zebker, H. A., P. A. Rosen, R. M. Goldstein, A. Gabriel, and C. H. Werner, On the derivation of coseismic displacement fields using differential radar interferometry: The Landers earthquake, J. Geophy. Res., vol. 99, pp. 19617-19634, 1994b.

Zhao, Z., Surface velocities of the East Antarctic ice streams from Radarsat-1 interferometric synthetic aperture radar data, Ph. D. Thesis, Dept. of CEEGS, The Ohio State University, Columbus, OH, 2001.

Zwally, H. J., and R. A. Bindschadler, Surface elevation contours of Greenland and Antarctic ice sheets, J. Geophys. Res., vol. 88(C3), pp. 1589-1596, 1983.

Zwally, H. J., J. A. Major, A. C. Brenner, and R. A. Bindschadler, Ice measurements by GEOSAT radar altimetry, Johns Hopkins APL Technical Digest, vol. 8, no. 2, pp. 251-254, 1987.

Zwally, H. J., A. C. Brenner, J. A. Major, R. A. Bindschadler, and J. G. Marsh, Growth of the Greenland Ice Sheet: Measurement, Science, vol. 246, pp. 288-289, 1989.

Zwally, H. J., A. C. Brenner, J. A. Major, T. V. Martin, and R. A. Bindschadler, Satellite radar altimetry over ice, Vol. 1, 2, and 4, NASA Ref. Pub. 1233, 1990.

Zwally, H.J., and M.B. Giovientto, Annual sea level variability induced by changes in sea ice extent and accumulation on ice sheets: an assessment based on remotely sensed data, Surveys in Geophys., vol. 18, pp. 327-340, 1997.

Zwally, H.J., B. Schutz, W. Abdalati, J. Abshire, C. Bentley, A. Brenner, J. Bufton, J. Dezio, D. Hancock, D. Harding, T. Herring, B. Minster, K. Quinn, S. Palm, J. Spinhirne, R. Thomas, ICESat's laser measurements of polar ice, atmosphere, ocean and land, J. Geodyn., vol. 34, pp. 405-445, 2002.

Zwally, H. J. and C. Shuman, ICESat: Ice, Cloud, and land Elevation Satellite, NASA GSFC, Greenbelt, MD, Brochure FS-2002-9-047-GSFC, 2002.
Zwally, H.J., R. Schutz, C. Bentley, J. Bufton, T. Herring, J. Minster, J. Spinhirne, and R. Thomas, GLAS/ICESat L2 Antarctic and Greenland Ice Sheet Altimetry Data V018, Boulder, CO: National Snow and Ice Data Center. Digital media, 2003.